High Energy High Repetition-Rate Thin-Disk Amplifier for OPCPA Pumping

Dissertation
zur Erlangung des Doktorgrades
des Department Physik
der Universität Hamburg

vorgelegt von
Dipl. Phys. Michael Schulz
aus Dresden

Hamburg
2013

Gutachter/in der Dissertation: Prof. Dr. Markus Drescher
Prof. Dr. Günter Huber

Gutachter/in der Disputation: Prof. Dr. Markus Drescher
Dr. Jens Osterhoff

Datum der Disputation: 22.08.2013

Vorsitzender des Prüfungsausschusses: Dr. Michael Martins

Vorsitzender des Promotionsausschusses: Prof. Dr. Peter Hauschildt

Dekan des Fachbereichs Physik: Prof. Dr. Heinrich Graener

Selbstständigkeitserklärung

Hiermit bestätige ich, die vorliegende Dissertation selbst verfasst und keine anderen als die angegebenen Quellen und Hilfsmittel verwendet zu haben.

Michael Schulz, Hamburg, 2013

Abstract

The development of a pump laser system for a high power and high repetition rate optical parametric chirped-pulse amplification (OPCPA) is presented in this thesis. The OPCPA system requires pump pulse energies in the range of tens of millijoules at high repetition rates with sub-picosecond pulse durations. This can be achieved to some extend with Innoslab amplifier technology. However, scaling to higher pulse energies at high repetition rates may be problematic. With the thin-disk amplifier presented in this thesis, output energies of 140 mJ at 100 kHz repetition rate could be achieved in burst-mode operation, which is a world record for this type of laser amplifier. Due to its material and spectral properties, ytterbium doped YAG (Yb:YAG) is used as a gain medium for the high power amplifier stages. The low quantum defect and the comparatively large emission bandwidth makes this material the choice for high power operation and sub-picosecond compressed pulse durations. The output beam profile as well as the shape of the output bursts is ideal to pump an OPCPA system. An OPCPA output energy in the millijoule range with repetition rates of 100 kHz to 1 MHz is needed to generate seed pulses for the FEL and for the application as pump-probe laser at the FEL facility.

Since the development of this laser system needs to meet requirements set by the Free-Electron Laser in Hamburg (FLASH), the amplifier is conceived for burst-mode operation. The main requirement is a high intra-burst pulse repetition rate of more than 100 kHz and a uniform pulse train (burst) with equal properties for every pulse. The burst-mode is an operation mode where the laser never reaches a lasing equilibrium, which means that the behavior of the amplifier is similar to a switch-on of the laser system for every burst. This makes the development of the amplifier system difficult. Therefore, an analytical model has been developed to study the amplification process during the burst. This includes the effect of amplified spontaneous emission (ASE) in the gain material as well as the operation of the pump laser in a burst-mode. Burst-mode operation requires a relatively long pre-pumping phase, which increases ASE related problems.

A very important parameter for a large-scale OPCPA system is the timing between pump and OPCPA seed pulses. A drift would cause a loss in the temporal overlap within the crystal. Therefore, a method for the synchronization of pump and seed laser pulses in the OPCPA system by means of a two-crystal balanced optical cross-correlator has been developed and tested.

Zusammenfassung

In dieser Arbeit wird die Entwicklung eines Pumplasersystems für einen hochrepetitiven optisch parametrischen Verstärker für gechirpte Pulse mit hohen Ausgangspulsenergien vorgestellt. Für das System sind Pumppulsenergien im Bereich von mehreren 10 Millijoule bei hohen Repetitionsraten und sub-Pikosekunden Pulsdauern erforderlich. Dies wird in gewissem Maße durch den Einsatz eines Innoslab Verstärkers erreicht. Jedoch ist die Skalierung dieses Konzepts zu hohen Pulsenergien bei hohen Wiederholraten problematisch. Mit dem in dieser Arbeit entwickelten Scheibenlaser wurde eine Pulsenergie von 140 mJ bei Repetitionsraten von 100 kHz erreicht, was einen Weltrekord für diese Art von Laser darstellt. Durch seine materiellen und spektroskopischen Eigenschaften wird mit Ytterbium dotiertes YAG (Yb:YAG) als Verstärkermaterial verwendet. Die vorteilhaften Eigenschaften sind ein geringer Quantendefekt und eine vergleichsweise hohe verstärkte Bandbreite, wodurch sich dieses Material besonders für die Verstärkung von Pulsen im Pikosekundenbereich eignet. Sowohl das Ausgangsstrahlprofil als auch die Form des Bursts zeigen eine sehr hohe Qualität, was einen Nutzen des Verstärkersystems als Pumplasersystem für das OPCPA System ermöglicht. Dies wird benötigt, um hohe Pulsenergien bei hohen Repetitionsraten für das Seeden und auch als Pump-Probe Laser für FLASH2 zu erreichen.

Da die Entwicklung des Lasersystems stark mit dem Freie-Elektronen Laser in Hamburg (FLASH) verknüpft ist, ist der Verstärker für den so genannten "Burst-Mode" Betrieb ausgelegt. Dies bedeutet, dass eine festgelegte Anzahl von Pulsen innerhalb eines "Bursts" vom Lasersystem erzeugt wird. Die Anforderungen an diesen Betriebsmodus ist die Erzeugung der Pulse mit gleichbleibenden Eigenschaften über den gesamten Burst. In diesem Betriebsmodus befindet sich der Laser niemals in einem Gleichgewichtszustand bezüglich der Lasereigenschaften. Um die Eigenschaften des Lasers in diesem Modus zu untersuchen, wurde ein analytisches Modell entwickelt. Dieses beinhaltet sowohl die Verstärkung von spontaner Emission (ASE) im Verstärkermedium als auch die Vorpumpzeit, welche benötigt wird, um einen flachen Burst zu erzeugen. Diese Vorpumpzeit resultiert in einem verstärkten Einfluss der ASE im Verstärker.

Ein sehr wichtiger Parameter für das OPCPA System ist die zeitliche Synchronisierung der Pump- und OPCPA-Seed-Pulse. Ein zeitlicher Drift würde den Verlust des zeitlichen Überlapps im OPCPA Kristall zur Folge haben. Dafür wurde ein auf zwei Kristallen basierender balancierter optischer Kreuzkorrelator entwickelt und getestet.

List of publications

M. Schulz, R. Riedel, A. Willner, T. Mans, C. Schnitzler, P. Russbueldt, J. Dolkemeyer, E. Seise, T. Gottschall, S. Hädrich, S. Düsterer, H. Schlarb, J. Feldhaus, J. Limpert, B. Faatz, A. Tünnermann, J. Rossbach, M. Drescher, and F. Tavella, "*Yb:YAG Innoslab amplifier: efficient high repetition rate subpicosecond pumping system for optical parametric chirped pulse amplification*", Opt. Lett. 36, 2456, (2011).

M. Schulz, R. Riedel, A. Willner, S. Düsterer, M.J. Prandolini, J. Feldhaus, B. Faatz, J. Rossbach, M. Drescher, and F. Tavella, "*Pulsed operation of a high average power Yb:YAG thin-disk multipass amplifier*", Opt. Express 20, 5038, (2012).

A. Willner, F. Tavella, M. Yeung, T. Dzelzainis, C. Kamperidis, M. Bakarezos, D. Adams, **M. Schulz**, R. Riedel, M.C. Hoffmann, W. Hu, J. Rossbach, M. Drescher, N.A. Papadogiannis, M. Tatarakis, B. Dromey, M. Zepf, "*Coherent Control of High Harmonic Generation via Dual-Gas Multijet Arrays*", PRL 107, 175002, (2011).

A. Willner, F. Tavella, M. Yeung, T. Dzelzainis, C. Kamperidis, M. Bakarezos, D. Adams, **M. Schulz**, R. Riedel, M.C. Hoffmann, W. Hu, J. Rossbach, M. Drescher, V.S. Yakovlev, N.A. Papadogiannis, M. Tatarakis, B. Dromey, M. Zepf, "*Efficient control of quantum paths via dual-gas high harmonic generation*", New Journal of Physics 13, 113001, (2011).

A. Willner, A. Hage, R. Riedel, I. Grguras, A. Simoncig, **M. Schulz**, T. Dzelzainis, H. Höppner, S. Huber, M.J. Prandolini, B. Dromey, M. Zepf, A.L. Cavalieri, F. Tavella, "*Coherent spectral enhancement of carrier-envelope-phase stable continua with dual-gas high harmonic generation*", Opt. Lett. 37, 3672, (2012).

U. Zastrau, V. Hilbert, C. Brown, T. Döppner, S. Dziarzhytski, E. Förster, S.H. Glenzer, S. Göde, G. Gregori, M. Harmand, D. Hochhaus, T. Laarmannm H.J. Lee, K.-H. Meiwes-Broer, P. Neumayer, A. Przystawik, P. Radcliffe, **M. Schulz**, S. Skruszewicz, F. Tavella, J. Tiggesbäumker, S. Toleikis, T. White, "*In-situ determination of dispersion and resolving power in simultaneous multiple-angle XUV spectroscopy*", Journal of Instrumentation 6, P10001, (2011).

M. Harmand, C.D. Murphy, C.R.D. Brown, M. Cammarata, T. Döppner, S. Düsterer, D. Fritz, E. Förster, E. Galtier, J. Gaudin, S.H. Glenzer, S. Göde, G. Gregory, V. Hilbert, D. Hochhaus, T. Laarmann, H.J. Lee, H. Lemke, K.-H. Meiwes-Broer, A. Moinard, P. Neumayer, A. Przystawik, H. Redlin, **M. Schulz**, S. Skruszewicz, F. Tavella, T. Tschentscher, T. White, U. Zastrau, S. Toleikis, "*Plasma switch as* *a temporal overlap tool for pump-probe experiments at FEL facilities*", Journal of Instrumentation 7, P08007, (2012).

A. Przystawik, A. Kickermann, A. Al-Shemmary, S. Düsterer, A.M. Ellis, K. von Haeften, M. Harmand, S. Ramakrishna, H. Redlin, L. Schroedter, **M. Schulz**, T. Seideman, N. Stojanovic, J. Szekely, F. Tavella, S. Toleikis, T. Laarmann, "*Generation of the simplest rotational wave packet in a diatomic molecule: Tracing a two-level superposition in the time domain*", Phys. Rev. A 85, 052503 (2012).

Conference contributions

M. Schulz, A. Willner, R. Riedel, M.J. Prandolini, S. Duesterer, J. Feldhaus, B. Faatz, J. Rossbach, M. Drescher, and F. Tavella, "*Kilowatt level Yb:YAG thin-disk pump laser amplifier system for seeding FLASH2*", Conference on Lasers and Electro-Optics (CLEO) 2012, CM1D, (2012).

M. Schulz [**invited talk**], A. Willner, R. Riedel, M.J. Prandolini, S. Düsterer, J. Feldhaus, B. Faatz, M. Drescher, and F. Tavella, "*Kilowatt level burst-mode OPCPA pump amplifier concepts*", Frontiers in Optics (FiO) conference 2012, FM4G.1, (2012).

F. Tavella, D. Adams, V. Ayvazyan, N. Baboi, J. Bahrdt, E. Bakarezos, V. Balandin, W. Decking, B. Dromey, T. Dzeltainis, S. Düsterer, M. Drescher, H. Eckoldt, B. Faatz, J. Feldhaus, R. Follath, M. Gensch, N. Golubeva, K. Holldack, C. Kamperidis, M. Körfer, T. Laarmann, A. Leuschner, L. Lilje, T. Limberg, A. Meseck, V. Miltchev, R. Mitzner, D. Nölle, N. Papadogiannis, A. Petrov, K. Rehlich, R. Riedel, J. Rossbach, H. Schlarb, B. Schmidt, M. Schmitz, S. Schreiber, J. Rönsch-Schulenburg, H. Schulte-Schrepping, **M. Schulz**, J. Spengler, M. Staack, M. Tatarakis, K. Tiedtke, M. Tischer, R. Treusch, A. Willner, M. Yeung, and M. Zepf, "*High Repetition Rate mJ-level Few-Cycle Pulse Laser Amplifier for XUV-FEL seeding*", High Intensity Lasers and High Field Phenomena (HILAS) conference 2011, HThD1, (2011).

A. Willner, **M. Schulz**, R. Riedel, M. Yeung, T. Dzelzainis, C. Kamperidis, M. Bakarezos, D. Adams, V. Yakovlev, J. Rönsch-Schulenburg, B. Dromey, N. Papadogiannis, M. Tatarakis, S. Düsterer, S. Schreiber, B. Faatz, M. Drescher, J. Rossbach, M. Zepf, and F. Tavella, "*A new XUV-source for seeding a FEL at high repetition rates* ", SPIE Proceedings Vol. 8075, (2011).

F. Tavella, R. Riedel, A. Willner, **M. Schulz**, M.J. Prandolini, S. Düsterer, J. Feldhaus, M. Drescher, and B. Faatz, "*Optical Parametric Chirped Pulse Amplification at High Repetition Rate Free Electron Laser Facility*", Frontiers in Optics (FiO) conference 2012, FTu5B.2 [invited talk], (2012).

Contents

Chapter 1

Introduction

Since the invention of the first optical laser in 1960 [1], lasers have become very important for a number of scientific fields. Four main output parameters can be defined, which are important for the application of the laser systems: First, the laser wavelength is important. For example, spectroscopy of semiconductors and dielectrics requires light pulses in the visible to UV spectral range. Shorter wavelengths can be achieved by frequency doubling [2], tripling [3] and quadrupling [4] common laser systems. The second parameter in the case of pulsed lasers is the pulse duration. Ultrashort pulses from common solid-state lasers can be generated by mode-locking of a laser oscillator [5–7]. With more sophisticated techniques such as high-harmonic generation [8, 9], pulse durations in the sub-femtosecond regime are within reach [10–12].

The remaining two parameters of laser systems are the repetition rate of the laser pulses and the pulse energy. An increase in one of the parameters usually goes hand in hand with the decrease of the other one, especially in the case of amplifiers for short pulse durations. For example, a high energy laser with pulse energies in the joule range normally has a repetition rate of only a few Hertz [13]. To increase both parameters at the same time in solid-state laser amplifiers, three main prerequisites have to be met. The first one is the availability of high power laser diodes for pumping the laser active medium. Secondly, the laser active medium has to have a high damage threshold and a low quantum defect in order to efficiently convert the pump light into the amplified laser pulses. The third prerequisite is the thermal management of the laser active medium. This can be optimized by design or by cryogenical cooling of the laser amplifier.

To achieve the thermal management by design, three main amplifier techniques have been developed in the past decades. The first is the amplification of pulses in a fiber [14]. Due to the large surface to volume ratio, a good heat removal can be achieved in the laser active medium. Nevertheless, this amplifier technique is limited in pulse energy due to the small mode field diameter in a fiber amplifier. This can be circumvented by coherent combination of several fibers, which is a sophisticated and complicated technique in terms of phase control of every single fiber source [15]. The second technique is Innoslab amplifiers [16]. Here, a large surface to volume ratio is achieved by the slab shaped geometry of the laser medium. In addition, the thermal properties in terms of thermal lensing of the amplifier during operation are used for the guiding of the laser pulses through the amplifier medium. This technique is also limited in pulse energy, because small mode field diameters are also used in the amplifier crystal. However, in burst-mode operation, the onset of the thermal lensing due to the pulsed pumping of the amplifier, achieving a flat burst shape is difficult. The third technique uses a thin disk as an active mirror in the amplifier [17]. Due to the small thickness of the gain medium, efficient heat removal can be achieved at the back plane of the medium. In addition, the heat flow is one-dimensional and in the direction of the amplified pulses, leading to a nearly vanishing thermal lensing. This technique allows for high pulse energies due to the large mode field diameter, which is used in the active medium. On the other hand, due to the small thickness of the medium, a large number of passes is needed for an efficient laser operation.

Nevertheless, with the thin-disk amplifier developed in the work presented, pulse energies of up to 140 mJ could be achieved at reasonable high repetition rates of 100 kHz. This concept can still be scaled to higher pulse energies by implementing additional thin-disk amplifier stages. A potential application for the developed thin-disk laser is for the pump-probe and seeding laser at the free-electron laser (FEL) FLASH in Hamburg, Germany. These lasers require a pump amplifier for a high power and high repetition rate optical parametric chirped-pulse amplification (OPCPA) system in the burst-mode.

1.1 Free-Electron Lasers

Free-electron lasers (FEL) are fourth generation sources of coherent XUV light [18, 19]. In a FEL, electrons are accelerated to relativistic energies in a linear particle accelerator and then steered through an undulator section. An undulator is a configuration of magnets with an alternating magnetic field. The electrons are forced to follow a sinusoidal trajectory where they emit incoherent spontaneous radiation. Depending on the undulator and electron beam properties, the wavelength of the emitted photons can range from the infrared down to the hard X-ray region. Due to the lack of adequate optics for wavelengths in the VUV and soft X-ray region, high gain FELs are necessary, where the radiation has to be created by a single pass of the electrons through the undulator structure. These FEL sources are operating in the so called self-amplified spontaneous emission (SASE) mode. The emitted light of the electron bunch interacts with the bunch itself, leading to a microbunching with a separation of the order of one wavelength of the emitted radiation. This leads to a coherent emission of radiation of the individual microbunches.

In the past decades, several FEL facilities have been developed at different research institutes. Facilities operating in the SASE operation mode include the Linac Coherent Light Source (LCLS, operating in the nm to Å range [18, 19]), the SPring-8 Angstrom Compact free electron LAser (SACLA, operating at wavelengths below 1 Å) and FLASH (see below). Facilities under development include the SwissFEL, the European X-FEL and FLASH2 (see below). These facilities offer special experimental conditions for studying the structure of matter and biological samples with outstanding resolution. In addition, pump-probe experiments can be performed in the XUV and X-ray range.

A major problem of FELs operating in SASE mode is the lack of temporal coherence of the generated radiation. This originates from the start of the amplification of light from shot noise. To overcome these problems, several methods of seeding can be implemented. Seeding dramatically improves the properties of the radiation since the start of the amplification process occurs with pulses with well defined properties. The most straightforward approach for seeding a FEL is direct seeding with a high-harmonic generated seed laser pulse. This has been performed at the SPring-8 compact SASE Source (SCSS) [20]. Another method for seeding has been implemented at the FERMI@Elettra Free-Electron Laser. Cascaded seeding via High Gain Harmonic Generation (HGHG) has been implemented to generate output wavelengths in the range of 20 down to 4 nm with well defined output pulse characteristics [21]. Compared to direct seeding, this method has the advantage that the constraints on the seed source are less stringent in terms of the generated wavelength. Another advantage of seeding with an external laser is that the seed laser can be synchronized with a pump-probe laser, making high temporal resolution pump-probe experiments feasible. At LCLS, self-seeded operation of the FEL could be achieved by mode-filtering of the generated radiation in a diamond monochromator [22]. This filtered radiation is then amplified further in the subsequent undulator sections, leading to high quality temporal coherence. Thus, no seed laser is needed at all in this scheme.

The Free-Electron Laser in Hamburg (FLASH) is a soft X-ray light source [23]. It delivers pulse energies in the microjoule range at wavelengths from 60 down to 4.45 nm. The goal of the current research on the machine is to improve the spatial and temporal coherence of this radiation. Due to the self-amplified spontaneous emission (SASE) process, these properties are poor compared to light generated in a classical laser. The approach to overcome this limitation is the direct or cascaded seeding of the FEL. Therefore, an extension of the existing FLASH facility is currently under construction, which is the FLASH2 project [24]. Seeding is foreseen with the HGHG concept. The planned parameters of the FEL with this seeding method are a wavelength range from 40 down to less than 10 nm and output pulse energies in the range of 30 to 200 μJ. The output pulse duration will be in the range of 15 to 80 fs. Laser pulses in the UV range are needed. The generation is performed with frequency tripling of an 800 nm pulse with tunable center wavelength of 700 to 950 nm.

1.2 The special challenge: Burst-mode amplifiers

The FLASH FEL operates in a burst-mode, which is a challenge for the laser system in terms of the adaption of the high laser repetition rate in this special operation mode. The burst-mode laser is never operated in equilibrium, concerning the laser operation given by the rate equations. For 10 Hz burst repetition rate, the laser is not amplifying pulses for most of the time. This leads to a switch-on like behavior of the laser for every amplified burst of pulses. For the application at the Free-Electron Laser FLASH, existing burst-mode lasers are operated as photo-injector laser [25] and also as pump-probe laser for experiments [26].

Thermal issues are less problematic in the case of burst-mode operation in contrast to a continuously operating laser system. A fixed repetition rate would be beneficial regarding the dynamics of the laser itself. However, the burst-mode requires low cooling for the entire laser system. In addition, the overall operation time of the pump diodes for the individual amplifier stages is much smaller than in continuous operation. It needs to be stated that the influence of the burst-mode operation on the lifetime of the laser diodes still needs to be investigated. The challenge of the burst-mode operation is the generation of a flat pulse train. The pulse train in our case consists of 80 pulses with an intra-burst repetition rate of 100 kHz. The burst repetition rate is 10 Hz with a temporal separation of the bursts of ca. 99 ms, which is well above the upper state lifetimes of common laser media. In the case of ytterbium-YAG as a laser active medium, which is used for the amplifiers presented in this thesis, the upper state lifetime is smaller than one millisecond. For every pulse train, the laser gain medium of each individual amplifier stage has to be pumped prior to the amplification of the pulses. This triggers problems with amplified spontaneous emission (ASE).

The burst operation mode of the amplifier system can also be used for materials processing applications. A high repetition rate laser system is interesting for a high processing speed. For high pulse energies, on the other hand, this comes hand in hand with a high average power of the laser output, leading to a strong thermal influence on the sample. Using a burst-mode amplifier, the beneficial properties of both types of system can be combined: The high intra-burst repetition rate for high processing speed and the low total average power due to the burst operation mode of the laser system [27].

1.3 OPCPA system development for applications at FLASH

For the application at the free-electron laser FLASH, an OPCPA system with output parameters matching the operation characteristics of the FEL is developed ([28, 29]). These parameters are, as already stated previously, a burst operation mode with a burst repetition rate of 10 Hz and an intra-burst repetition rate of 100 kHz. The output pulse energy of the OPCPA system is planned to be in the millijoule range with a spectral bandwidth supporting compression of the pulses to sub-7 to 20 femtosecond pulse durations for pump-probe experiments. For seeding applications at FLASH, a tunable OPCPA is foreseen with a wavelength range of 700 to 950 nm and pulse durations of 30 or 100 fs. A schematic of the planned setup is displayed in figure 1.1.

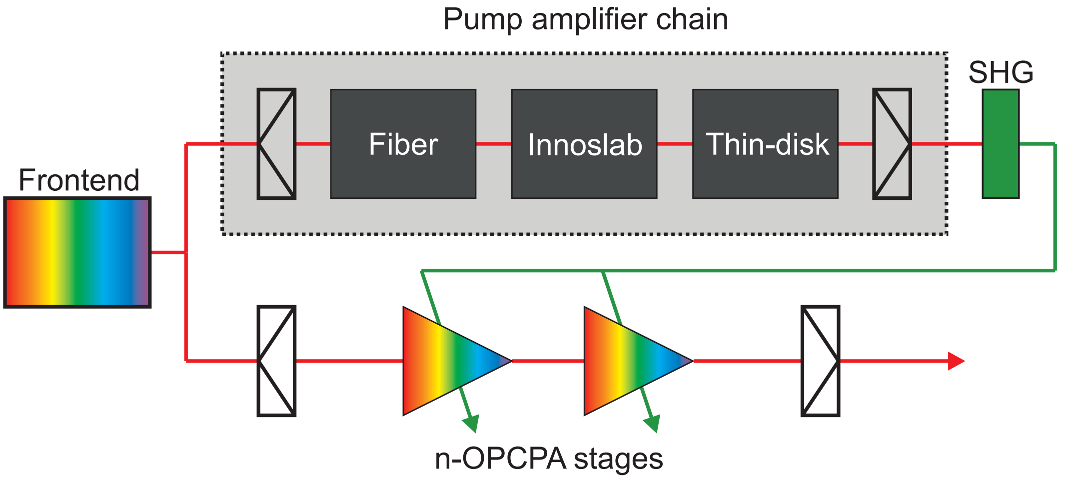

Figure 1.1: Planned setup of the OPCPA system. The seed light from the frontend is split for OPCPA and pump amplifier seeding. The latter is used as pump pulses for the OPCPA system after frequency doubling.

The frontend of the laser system is a titanium sapphire (Ti:Sa) oscillator. The output of this oscillator is used to seed both pump amplifier chain and OPCPA system. Thus, an intrinsic optical synchronization of both systems is provided. The pump amplifier is chirped-pulse amplification (CPA) system with a fiber amplifier system and further booster amplifiers. The booster system can be either an Innoslab amplifier, a thin-disk amplifier or a combination of both. The performance study of both systems and the development of the thin-disk amplifier is the main focus of this thesis. The compressed pulses are frequency doubled in a nonlinear crystal and used as pump pulses for the OPCPA system. The burst operation mode is implemented in the pump amplifier chain and is transferred in the OPCPA amplifier stages, where only pulses are amplified which are temporally overlapped with a pump pulse.

The output of the OPCPA stage is interesting for the applications at the free-electron laser FLASH and can be used for the generation of high harmonics (HHG) for direct seeding of the FEL with a short wavelength, for third-harmonic generation (THG) for high gain harmonic-generation seeding of the FEL or directly as a pump-probe laser for experiments at the facility.

1.4 Thesis outline

The thesis is structured as follows:

- A survey of theory and methods used in this thesis is given in chapter 2. This includes the linear and nonlinear interactions of light with matter. In addition, a survey of different solid-state amplifier techniques is presented in this chapter.

- In chapter 3, an analytical model for the investigation of the thin-disk amplifier is presented. The model is one-dimensional and includes the burst-mode operation of the amplifier as well as the influence of amplified spontaneous emission (ASE). This has to be considered for the burst-mode since an unseeded pre-pumping time of the amplifier is necessary to achieve a flat burst.

- The experimental setup of the amplifier system is described in chapter 4. The pump amplifier setup is described. A synchronization method for pump and seed pulses in the OPCPA system by means of a balanced cross-correlator is presented.

- Chapter 5 summarizes the experimental results achieved with Innoslab amplifier technique as well as with the thin-disk amplifier. In addition, a comparison of the experimental results with the analytical model is given. At the end of the chapter, measurements performed with the balanced cross-correlator for the pump-seed synchronization are presented.

- A summary of the entire work presented in this thesis is given in chapter 6.

Chapter 2

Theoretical background

In this chapter, the theoretical background on which this work is based is presented. Starting with the basic properties of laser light, the foundations for modeling the laser system will be presented in section 2.1. This includes the spatial and also the temporal properties of Gaussian beams and pulses as well as linear interactions with matter. In section 2.2, the nonlinear interactions of light with matter are described, which is the basis for second-harmonic generation and for optical parametric amplification. Section 2.3 deals with the techniques for the amplification of laser pulses. This includes the basic properties of chirped-pulse amplification, optical parametric chirped-pulse amplification as well as diode pumped solid-state laser technologies. In particular, amplifiers based on Ytterbium doped gain media are investigated. A theoretical description of the properties of this gain medium is given in section 2.4. The main topic of this thesis is the development of an Yb:YAG thin-disk laser amplifier.

2.1 Properties of light

This section gives an overview on the fundamental properties of laser light. In section 2.1.1 the spatial properties of Gaussian beams are given. This is the basis for the numerical method for modeling beam propagation, based on the beam propagation matrices. These are described in detail in section 2.1.2. The temporal properties of Gaussian pulses will be presented in section 2.1.3 with the properties of pulses in the time and frequency domain. In section 2.1.4, linear interactions of light with matter will be discussed. This includes the influence of matter on the light pulses by means of dispersion and also linear absorption of light in materials.

2.1.1 Spatial properties of Gaussian beams

In the spatial domain, the intensity distribution $I(r,z)$ of a Gaussian beam with power P can be described by the following equation [30]:

$$I(r,z) = \frac{2P}{\pi w(z)^2} \exp\left(-2\frac{r^2}{w(z)^2}\right), \tag{2.1}$$

where r is the distance from the beam axis, z is the position along the beam axis and $w(z)$ is the radius where the intensity of the beam drops to $1/\mathrm{e}^2$ of the peak value. The development of the beam radius along the beam axis is described by (definitions derived from [31]):

$$w(z) = w_0\sqrt{1+\left(\frac{z\lambda_0}{w_0^2 n\pi}\right)^2}, \tag{2.2}$$

with w_0 as beam waist, λ_0 as center wavelength of the laser beam and n as refractive index of the medium in which the light propagates. An important parameter regarding the description of Gaussian beams is the Rayleigh length z_R:

$$z_R = \frac{n\pi}{\lambda_0} w_0^2. \tag{2.3}$$

At the distance of one Rayleigh length from the beam waist, the Gaussian beam is expanded by a factor of $\sqrt{2}$. By using the Rayleigh length, equation 2.2 can be simplified to:

$$w(z) = \sqrt{\frac{\lambda_0 z_R}{n\pi}\left(1+\frac{z^2}{z_R^2}\right)}. \tag{2.4}$$

For the full description of a Gaussian beam with central wavelength λ_0, the position, size of the beam waist and refractive index are fully sufficient. Figure 2.1 shows a schematic of the beam parameters given above.

For the propagation of Gaussian beams, it is also useful to define the radius of curvature of the wavefront $R(z)$ and the divergence angle Θ of the beam:

$$R(z) = z\left(1+\frac{z_R^2}{z^2}\right), \tag{2.5}$$

$$\Theta = \frac{w_0}{z_R} = \frac{\lambda_0}{n\pi w_0}. \tag{2.6}$$

With these parameters, one can define the complex beam parameter $q(z)$, which leads to a very elegant way to describe the propagation of Gaussian beams with the ray transfer matrix algorithm described in section 2.1.2. It is defined as:

$$\frac{1}{q(z)} = \frac{1}{R(z)} - \frac{i\lambda_0}{\pi n w(z)^2}. \tag{2.7}$$

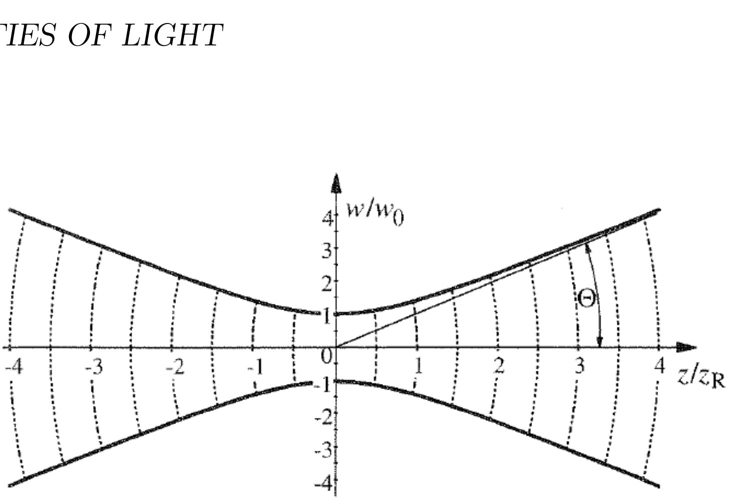

Figure 2.1: Schematic of the Gaussian beam properties [31]. The beam size w of the Gaussian beam normalized to the waist diameter w_0 is plotted over the propagation distance z normalized to the Rayleigh length z_R.

2.1.2 Beam propagation matrices

For modeling long beam paths with several focusing elements, the ray-transfer matrix formalism has proved to be a very powerful tool [32]. Every element of the beam path is given as an ABCD-matrix containing the manipulation of spatial and angular properties of a laser beam, which is given as a vector with 2 elements. The resulting equation is then written as (formulas and matrices taken from [31]):

$$\begin{pmatrix} w_{out} \\ w_{out'} \end{pmatrix} = \begin{pmatrix} A & B \\ C & D \end{pmatrix} \cdot \begin{pmatrix} w_{in} \\ w_{in'} \end{pmatrix}, \tag{2.8}$$

where w_{in} and w_{out} are the widths of the in- and outgoing beam, and $w_{in'}$ and $w_{out'}$ are the divergence angles of the in- and outgoing beam, respectively. In geometrical optics, these parameters can be understood as offset and angle with respect to the beam axis as well. This equation can be used for calculating the beam propagation in the x-z-plane or the y-z-plane. For calculating the propagation through n optical elements with the corresponding ABCD-matrices M_i, the calculation is performed as follows:

$$\begin{pmatrix} w_{out} \\ w_{out'} \end{pmatrix} = M_n \cdot M_{n-1} \cdot ... \cdot M_1 \cdot \begin{pmatrix} w_{in} \\ w_{in'} \end{pmatrix}, \tag{2.9}$$

The following matrices (2.10) are the most commonly used: Drift in free space, thin lenses and spherical mirrors.

$$\begin{pmatrix} 1 & L \\ 0 & 1 \end{pmatrix}, \begin{pmatrix} 1 & 0 \\ -\frac{1}{f} & 1 \end{pmatrix}, \begin{pmatrix} 1 & 0 \\ -\frac{2}{R} & 1 \end{pmatrix}, \tag{2.10}$$

where L is the path length of the propagating light without optical elements, f is the focal length of the lens and R is the radius of curvature of the spherical mirror.

For the propagation of Gaussian beams with the ABCD-matrices, it is useful to use the q-parameter defined in equation 2.7. After combining the matrices of all optical elements in the beam path, the q-parameter of the outgoing beam depending on the q-parameter of the incoming beam is given as:

$$q_{out} = \frac{q_{in} \cdot A + B}{q_{in} \cdot C + D}. \tag{2.11}$$

2.1.3 Temporal properties of Gaussian pulses

In the temporal domain, the power distribution $P(t)$ of Gaussian laser pulses is described by the following formula:

$$P(t) = P_p \exp\left(-4\ln 2 \left(\frac{t}{\Delta\tau}\right)^2\right), \tag{2.12}$$

where P_p is the peak power of the pulse and $\Delta\tau$ is the pulse duration measured at the full width at half-maximum (FWHM). In the frequency domain, the electric field of a Gaussian pulse is defined as [33]:

$$E(\omega) \propto E_0 \exp\left(-\frac{(\omega - \omega_0)^2}{\Delta\omega^2}\right), \tag{2.13}$$

where E_0 is the peak electric field, ω_0 is the center frequency of the pulse and $\Delta\omega$ is the spectral width. The relationship between pulse duration and spectral bandwidth is given by the time-bandwidth product (*tbp*):

$$tbp = \Delta\omega \cdot \Delta\tau, \tag{2.14}$$

where $\Delta\omega$ is the spectral width of the pulse in the frequency domain and $\Delta\tau$ is the pulse duration. For Gaussian pulses, the *tbp* is 0.441. This is directly derived from the Fourier transformation of the Gaussian pulse. The time-bandwidth product can be used to define a lower limit of the pulse duration for a given spectral width of the laser pulses.

The chirp of the pulse is a linear change of the optical frequency of the laser field within the Gaussian envelope of the pulse. This means that the different frequency components of a pulse are shifted in time with respect to each other within the envelope of the pulse. Up-chirp is then defined as an increase of the instantaneous frequency with time, while down-chirp is defined as a decrease of the instantaneous frequency with time. Figure 2.2 shows a schematic of an up-chirped laser pulse, where the low frequency parts are at the rising edge of the Gaussian pulse envelope.

The characteristics of linear pulse chirp is explained in more detail in section 2.1.3. For quantifying the chirp of a pulse, the rate of change of the instantaneous frequency is given in Hertz per second. If this number is constant within the temporal pulse envelope, the chirp is defined as linear.

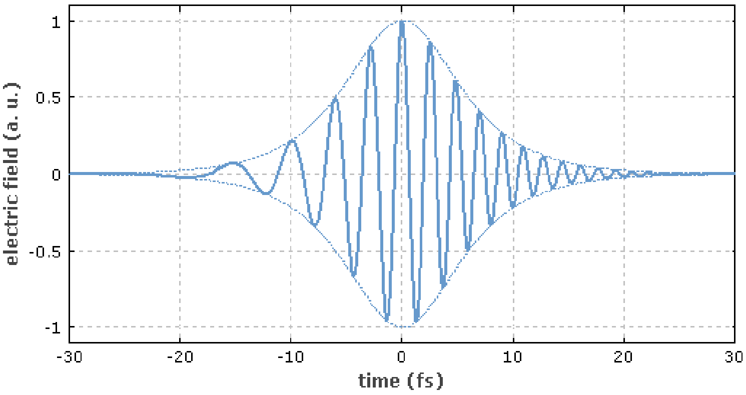

Figure 2.2: Schematic of an up-chirp of a Gaussian laser pulse [30]. The low frequency parts of the laser light are at the rising edge of the pulse in the temporal domain.

2.1.4 Linear optics: Dispersion and Absorption

Laser pulses consist of a set of frequency components. The dispersion of these components through propagation in matter have to be taken into account. Dispersion describes the materials wavelength dependent refractive index $n(\lambda)$. Without absorption in the medium, only the real part of the complex refractive index is non-zero. Normal dispersion is then defined as:

$$\frac{dn}{d\lambda} < 0. \tag{2.15}$$

In the range of absorption of light in matter, the real part of the refractive index increases with the wavelength, which is called anomalous dispersion:

$$\frac{dn}{d\lambda} > 0. \tag{2.16}$$

In the case of anomalous dispersion, the imaginary part of the refractive index starts to play a role. For the quantification of the linear dispersion in a medium, it is useful to define the phase velocity of the light wave:

$$v_p = \frac{c_0}{n} = \frac{1}{\sqrt{\epsilon_0 \mu_0 \epsilon_r \mu_r}} = \nu_0 \frac{\lambda_0}{n}, \tag{2.17}$$

where c_0 is the vacuum speed of light, ϵ_0, μ_0, ϵ_r and μ_r are the permittivity and permeability of vacuum and of the material, respectively, and λ_0 is the wavelength of the light. The group velocity of laser pulses is then given by:

$$v_g = v_p - \lambda \frac{dv_p}{d\lambda}. \tag{2.18}$$

For broadband laser pulses, the difference in individual phase velocities of the different frequency components will cause delays of the different spectral parts of the light pulse with respect to each other, leading to a linear chirp of the laser pulse.

When light passes through matter, photons of the incident light can be absorbed in the medium. This absorption of light can be described by Lambert-Beers law:

$$I(z) = I_0 \cdot \exp(-\alpha z), \tag{2.19}$$

where z is the penetration depth of the light in the medium, I_0 is the intensity of the light at $z=0$ and α is the absorption coefficient which can be derived from the imaginary part of the complex refractive index by:

$$\alpha = \frac{4\pi}{\lambda} n_{imag}, \tag{2.20}$$

with λ as wavelength of the incident light. It can be seen that this absorption coefficient and thus the transmission $T = I/I_0$ of a medium are a function of the corresponding wavelength. With these parameters, an absorption cross section for a medium can be defined by:

$$\sigma(\lambda) = \frac{\alpha(\lambda)}{N_{part}}, \tag{2.21}$$

where N_{part} is the particle density of the corresponding medium. These cross sections are important for the modeling of rate equations to describe the populations of the energy levels for laser active materials. In the case of absorption, the corresponding cross section can directly be measured for example by using a white-light source and measuring the transmitted spectrum of the corresponding medium. The emission cross sections of laser active materials are measured by triggering fluorescence of the medium and measuring the emission spectrum.

2.2 Nonlinear optics

The interaction of light with matter can be divided into linear and nonlinear interaction. The distinction between these two cases is given by the response of the polarization of the medium on the laser electric field. The polarization in the linear case is given by [31]:

$$\vec{P}_{lin}(\vec{r},t) = \epsilon_0 \chi^{(1)}(\vec{r}) \vec{E}(\vec{r},t), \tag{2.22}$$

where ϵ_0 is the dielectric constant of vacuum and $\chi^{(1)}$ is the linear electric susceptibility of the medium. The linear interactions of light with matter are e.g. dispersion, refraction and absorption (see section 2.1.4).

If the electric field reaches magnitudes exceeding 10^4 V/cm, the interaction of the light with matter enters the nonlinear regime, where the polarization term given in equation 2.22 needs to be modified to take into account its nonlinear terms. The resulting polarization for the nonlinear regime reads as follows:

$$\vec{P}(\vec{r},t) = \vec{P}_{lin}(\vec{r},t) + \vec{P}_{nl}(\vec{r},t), \tag{2.23}$$

with the nonlinear polarization term:

$$\vec{P}_{nl}(\vec{r},t) = \epsilon_0 \chi^{(2)}(\vec{r})\vec{E}^2(\vec{r},t) + \epsilon_0 \chi^{(3)}(\vec{r})\vec{E}^3(\vec{r},t) + \cdots . \tag{2.24}$$

The types of nonlinear interactions are categorized by the order of the nonlinear susceptibility. The following list gives an overview about the relevant nonlinear interactions which are important in this thesis:

Second-Order effects

- Second harmonic generation (SHG)
- Sum and difference frequency generation (SFG, DFG)
- Optical parametric amplification (OPA)

Third-Order effects

- Kerr effect, including self-focussing and self-phase modulation

A detailed description of these nonlinear interactions will be given in the following.

Nonlinear interactions: The $\chi^{(2)}$ nonlinearity

In the case of two equal monochromatic waves with the same polarization and frequency ν_{fund}, the second order polarization of the medium is described by the product of the two electric fields [31]:

$$P^{(2)} = \epsilon_0 \chi^{(2)} \vec{E}_1 \vec{E}_2 = \epsilon_0 \chi^{(2)} \vec{E}^2 = P^{(2)}(0) + P^{(2)}(2\nu_{fund}), \tag{2.25}$$

where two polarization terms with frequency $\nu = 0$ and $\nu = 2\nu_0$ appear. The first term describes a rectified field in the medium, which is a macroscopic charge separation in the material. The second term describes the polarization oscillation with twice the frequency of the incident wave. This polarization wave emits a new light wave with twice the optical frequency which is referred to as the second harmonic of the fundamental wave. The efficiency of this process strongly depends the phase relations between the fundamental and the second harmonic wave. The intensity of the generated second harmonic wave depends on the position z along the beam axis in the crystal and can be described by:

$$I_{SHG}(z) = I_{fund}^2 \frac{2\pi^2 d^2 z^2}{\epsilon_0 c_0 \lambda_{fund}^2 n_{fund}^2 n_{SHG}} \left[\frac{\sin(\Delta k z/2)}{\Delta k/2} \right]^2 , \tag{2.26}$$

where I_{fund} is the intensity of the fundamental wave, d is the relevant matrix element derived from the $\chi^{(2)}$-tensor, n_{fund} and n_{SHG} are the refractive indices for the fundamental and the second harmonic wave and Δk is the phase mismatch. The intensity of the converted frequency shows an oscillatory behavior along the z-axis in the crystal. To avoid this oscillatory behavior and thus optimization of the frequency doubling process, the phase mismatch should fulfill the following condition:

$$\Delta k = |k_{SHG} - 2k_{fund}| \equiv 0, \tag{2.27}$$

with the wave numbers k_{fund} and k_{SHG} of the fundamental and the second harmonic wave. Phase matching of the second harmonic generation process can be achieved in anisotropic materials like birefringent crystals, for example beta barium borate (BBO, uniaxial crystal). The orientation of the crystal can be chosen such that the fundamental wave is propagating in the ordinary axis of the crystal, while the second harmonic is generated in the angle-dependent extraordinary axis, which is then called type-I phase matching. In the case of type-II phase matching, the two fundamental beams have perpendicular polarization. The fundamental waves propagate through the medium in the ordinary and in the extraordinary axis, respectively, and the generated second harmonic beam has extraordinary polarization. The conditions for the two types of phase matching are:

$$k_{SHG}(e) = k_{fund}(o) + k_{fund}(o) \tag{2.28}$$

for type-I phase matching and

$$k_{SHG}(e) = k_{fund}(o) + k_{fund}(e) \tag{2.29}$$

for type-II phase matching, where o and e are the ordinary and extraordinary waves.

The best phase matching angle, which is the angle between the optical axis of the crystal and the beam axis, can then be derived with following formula [31]:

$$\sin^2(\Theta_{pm}) = \frac{\frac{1}{n_{o,1}^2} - \frac{1}{n_{o,2}^2}}{\frac{1}{n_{e,2}^2} - \frac{1}{n_{o,2}^2}}, \tag{2.30}$$

with $n_{o,1}$, $n_{o,2}$ and $n_{e,2}$ as refractive indices of the ordinary and extraordinary axis for the fundamental (1) and second harmonic (2) wavelengths. Figure 2.3 shows the indicatrix of an uniaxial crystal for type-I phase matching.

From this figure, it can be seen that for a certain angle Θ_{pm}, which can be derived from equation 2.30, the ordinary axis of the fundamental beam and the extraordinary axis of the second harmonic beam have the same refractive index and thus the wave vector mismatch is kept close to zero. The first demonstration of second-harmonic generation has been reported for crystalline quartz [2]. Since then, a number of various

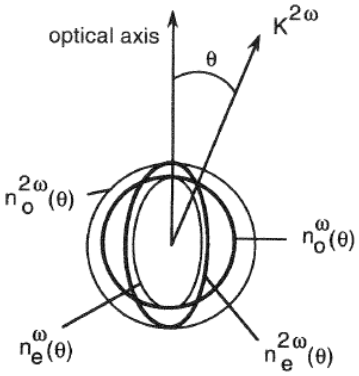

Figure 2.3: Indicatrix of an uniaxial crystal [33].

materials has found application for second harmonic generation. The best crystals for second-harmonic generation are Beta-Barium Borate (BBO), Lithium Niobate (LBO), Potassium Titanyl Phosphate (KTP) as well as Potassium Dihydrogen Phosphate (KDP). Very high conversion efficiencies have been shown for KTP (85 %, [34]) and for LBO (82 %, [35]).

In a more general case, where the incident waves have different frequencies ν_1 and ν_2, frequency mixing of the two waves can be achieved. This means that in addition to second-harmonic generation with $\nu = 2\nu_1$ and $\nu = 2\nu_2$ and the DC component with $\nu = 0$, two new waves with the sum frequency

$$\nu_{sum} = \nu_1 + \nu_2 \tag{2.31}$$

and the difference frequency

$$\nu_{diff} = |\nu_1 - \nu_2| \tag{2.32}$$

can be generated. These processes are referred to as sum frequency generation (SFG) and difference frequency generation (DFG). These two mechanisms have applications in optical parametric amplification as DFG (see section 2.2) and for the balanced detection of the timing of two different light sources. The balanced detection is described in more detail in section 4.5 as a tool for stabilizing the arrival time between the pump and the OPCPA seed pulses.

Nonlinear interactions: The $\chi^{(3)}$ nonlinearity

The nonlinear polarization for third-order effects is defined by [31]:

$$\vec{P}^{(3)} = \epsilon_0 \chi^{(3)} \vec{E}_1 \vec{E}_2 \vec{E}_3. \tag{2.33}$$

This equation describes the interaction of three light fields, which can originate from the same laser beam or from different beams. The third-order nonlinear susceptibility $\chi^{(3)}$ is a four-dimensional tensor. For isotropic materials, second-order effects are not present. Thus, only the third-order effects need to be taken into account. Based on the third-order nonlinear polarization, optical birefringence can be induced in isotropic materials, leading to a change of the refractive index, which is dependent on the intensity and polarization direction of the incident light pulses. Assuming a beam with linear polarization in x-direction, the change of the refractive index is given by [31]:

$$\Delta n_x = \frac{3}{4}\frac{e_{11}}{2n_0}E_x^2 = K_{Kerr}\lambda E_x^2, \tag{2.34}$$

where e_{11} is the first $\chi^{(3)}$-tensor matrix element, n_0 is the intrinsic refractive index of the material, K_{Kerr} is the material dependant Kerr constant and λ is the wavelength of the incident light field. This so called Kerr effect can be used for manipulating the polarization of an incident light beam by applying a strong electric field to a medium. For low intensity laser beams, where the electric field of the light has no influence on the Kerr effect, the change in the refractive index is only dependent on the external electric field which is applied to the material.

For high laser intensities with a Gaussian distribution, as for example given in equation 2.1, the change of the refractive index is intensity dependent. The strength of this refractive index change is then given by [31]:

$$n(r,I) = n_0 + \Delta n_r = n_0 + \frac{3}{8}\frac{e_{11}}{n_0}E^2(r) = n_0 + \frac{3}{4}\frac{e_{11}}{n_0^2 c_0 \epsilon_0}I(r) = n_0 + n_2 I(r), \tag{2.35}$$

where n_2 is the nonlinear refractive index of the medium.

This modulation of the index of refraction leads to a focussing effect on the light beam, referred to as Kerr lens. If the beam is focussed by Kerr lensing, the intensity in the medium will increase and thus strengthen the effect. This increasing effect of the Kerr lens will at some point be interrupted by the divergence of the Gaussian beam, which gets larger for decreasing beam diameters. This leads to an equilibrium of divergence and focussing where the light propagates as in a waveguide with constant diameter.

An important factor for Kerr lensing is the definition of a critical power P_{crit} where Kerr lensing sets in [31]:

$$P_{crit} = \frac{2}{3}\frac{\epsilon_0 c_0 \lambda^2 n_0}{\pi e_{11}}. \tag{2.36}$$

For peak powers below the critical power, the wavefronts of the incident light beam will remain unaffected. At the critical power, the Kerr lens counteracts the divergence of the laser beam such that the beam diameter will remain the same throughout the propagation distance, which is called self-trapping of the laser beam. Beyond the critical power, Kerr lensing sets in. For a very thin medium, where the equilibrium stated above is not reached, the dioptric power of the Kerr lens can be given by [30]:

$$\frac{1}{f} = \frac{4n_2 d}{\pi w^4} P, \tag{2.37}$$

where d is the thickness of the medium and w and P are the beam radius and power of the incident laser pulses, respectively. If the medium is thick enough to reach the equilibrium, the distance z_f from the incoupling facet of the medium to the point where the waveguide starts is given by [31]:

$$z_f = \frac{\pi w^2}{\lambda \sqrt{\frac{P}{P_{crit}} - 1}}. \tag{2.38}$$

Although the effect of Kerr lensing can be detrimental in most applications, it can also be useful for some special purposes. For example, the generation of white-light in a transparent medium in order to reach a large spectral bandwidth by self-phase modulation (see below) or passive mode-locking of Titanium Sapphire lasers.

In the temporal domain, the Kerr effect can lead to a change of the refractive index dependent on the temporal shape of the intensity distribution of the laser pulses. This will change the phase velocity of the frequency components of the light pulse within the envelope of the pulse, leading to a temporal chirp of the pulses. For a material of length L, the phase change of the light is given by [31]:

$$\frac{d\phi}{dt} = \nu_0 \left(1 - \frac{L}{c_0}\frac{dn_2}{dt}\right). \tag{2.39}$$

Strong self-phase modulation leads to the creation of new frequency components, which results to spectral broadening of the laser pulses [36]. These new optical frequencies are well ordered within the envelope of the laser pulses in the temporal domain. Due to this fact, the broadened pulses can be compressed by means of a dispersive element, as e.g. done in reference [37] with a grating compressor. There 35 fs pulses could be compressed to a pulse duration of sub-4 fs, or 1.5 optical cycles in the pulse envelope.

An important quantity to describe the nonlinear accumulated phase is the B-Integral, defined by [38]:

$$B = \frac{2\pi}{\lambda} \int_0^L n_2 I(z) dz, \tag{2.40}$$

with L as the medium length. The B-integral describes the on-axis nonlinear phase shift which an intense laser pulse accumulates by transmission through material. If the B-integral of a laser pulse is well below 1, the influence of self-phase modulation and self focusing can be considered to be very small. For B-integral values exceeding 3, strong self-focusing in the passed medium may occur, leading to a collapse of the beam radius to very small values. This effect can be detrimental for the amplification of laser pulses in solid-state laser amplifiers.

2.3 Amplification of laser pulses

This section is dedicated to the techniques for amplification of laser pulses. Firstly, the technique of chirped-pulse amplification (CPA), which is important for amplification of pulses to high energies used in solid-state lasers and in optical parametric amplifiers is described in section 2.3.1. Optical parametric amplification (OPA) in combination with the CPA technique is referred to as the optical parametric chirped-pulse amplification (OPCPA) and will be described in section 2.3.2. Section 2.3.3 will give an introduction on the properties of diode pumped solid-state lasers, with the corresponding rate equations given in section 2.3.4. The sections 2.3.5 to 2.3.7 will then give an overview on the three amplifier technologies used in the context of this thesis, which are fiber laser amplifiers, Innoslab amplifiers and thin-disk amplifier technology.

2.3.1 Chirped-pulse amplification

A very important technique for the amplification of laser pulses to high energies is the chirped-pulse amplification (CPA). It is based on stretching the laser pulses in the temporal domain with for example a grating stretcher, introducing a linear chirp in the laser pulse. The pulses are then amplified to high pulse energies and then recompressed by removing the temporal chirp of the laser pulses with an adequate dispersive element. A schematic of the CPA technique is shown in figure 2.4.

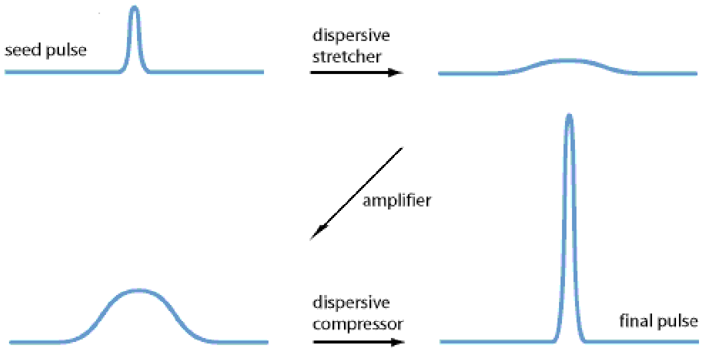

Figure 2.4: Schematic of chirped-pulse amplification [30]. The seed laser pulses are stretched in time by means of a dispersive element, tremendously reducing the pulse peak power. The pulses are then amplified and after that compressed in a complementary dispersive medium.

The advantage of this technique is that the intensity of the pulses is dramatically lowered in the amplification medium. Thus, optical damages or nonlinearities arising from high peak powers are avoided. The concept of chirped-pulse amplification was first demonstrated in reference [39]. The implementation of this technique lead to a breakthrough in the amplification of laser pulses to peak powers beyond the terawatt range. Petawatt laser pulses have been demonstrated for example in reference [40], with pulse energies of 660 J, compressed to 440 fs with a pulse peak power of 1.5 PW. Typical stretching factors in the CPA technique are in the range of 1000 to 10000, stretching pulses from hundrets of femtoseconds to nanosecond pulse durations.

Fiber laser systems also tremendously benefit from CPA because of the very small mode field diameters in the fiber. Pulse durations in the nanosecond regime are required to reduce nonlinear effects such as self-focussing and self-phase modulation in the fiber. Although being a very powerful technique, CPA can not be driven to very large stretching and compression ratios due to a large amount of dispersion which would be required from the stretcher and compressor. This would lead to complicated stretcher setups with very long beam paths. This would result in strong stability fluctuations of the entire amplifier system. Methods for reaching higher pulse energies from a fiber amplifier by increasing the mode field diameter of the fiber are described in section 2.3.5.

2.3.2 Optical parametric chirped-pulse amplification

Optical parametric amplification [41, 42] is a second order nonlinear effect, described in more detail in section 2.1.3. It is based on difference frequency generation, where two laser pulses of different wavelength, the pump and the signal wave, overlapped in a medium with a large $\chi^{(2)}$-nonlinearity, generate a third wave called the idler. Generation of the idler is an important effect crucial to conserve energy and momentum of the light waves participating in the parametric process. The pump wavelength needs to be shorter than the signal wavelength, such that photons of the pump pulse are converted to photons of the (lower energetic) signal wavelength and the idler wavelength. The conversion is an instantaneous process, there is no energy storage in the medium. The advantage is a very low thermal load of the gain material and thus amplification of high energy pulses at high repetition rates is possible. The physical conservation rules for OPCPA are described by the following equations:

$$\omega_s = \omega_p - \omega_i \tag{2.41}$$

is the energy conservation equation, with the angular frequencies ω_s, ω_p and ω_i for the seed, pump and idler pulses, respectively, and

$$\Delta\vec{k} = \vec{k}_p - \vec{k}_s - \vec{k}_i \overset{!}{=} 0 \tag{2.42}$$

is the momentum conservation rule. While the energy conservation is intrinsically fulfilled, the momentum conservation needs to be satisfied through phase matching in the nonlinear medium as already described in section 2.1.3. The efficiency of the parametric process depends partly from phase matching. The best conversion efficiency can be obtained if the phase relation between pump, signal and idler has a constant value of

$$\Phi = \phi_p - \phi_i - \phi_s = -\frac{\pi}{2}, \tag{2.43}$$

which is always fulfilled at the beginning of amplification, where the idler wave is not present. The latter then takes a phase value of

$$\phi_i(0) = \phi_p(0) - \phi_s(0) + \frac{\pi}{2}. \tag{2.44}$$

While propagating through the nonlinear medium, the phase of pump, signal and idler accumulate with increasing length in the crystal, leading to a rise of the wave-vector mismatch Δk. If this phase-mismatch reaches a value of π, the energy flow reverses. The characteristic coherence length of the parametric process is

$$L_{coh} = \frac{\pi}{|\Delta \vec{k}|}. \tag{2.45}$$

The coherence length can be increased by choosing the optimal phase matching conditions. This can be done in different ways, for example by quasi-phase matching in a periodically poled crystal [43] or by birefringent phase matching in a nonlinear crystal. Birefringent phase matching can be achieved in two different ways, the collinear interaction of pump and signal and the non-collinear interaction [44]. Figure 2.5 shows a schematic of these two methods.

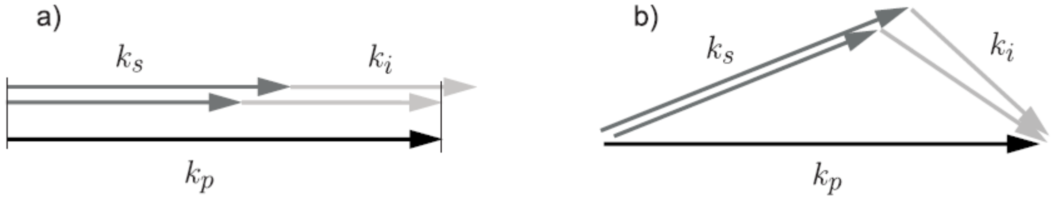

Figure 2.5: Schematic of a) collinear and b) non-collinear interactions of the pump and signal beam in the parametric amplification medium [45].

In the case of collinear phase matching, the conditions are easy to achieve by rotating the crystal into the required angle where the best phase matching conditions are fulfilled (see also section 2.1.3). For the amplification of broadband pulses, this geometry has on the other hand the disadvantage that best phase matching can only be achieved for a very narrow spectral range for the seed if a narrowband pump beam is used. With non-collinear geometry, phase matching for the different frequency components is achieved by an angular spread of the generated idler wave. In this configuration, a new degree of freedom is needed to satisfy the phase matching conditions, which is the angle between the pump and the signal beam in the parametric gain medium. Very broadband signal pulses can be amplified in a non-collinear optical parametric amplifier, bringing ultrashort laser pulses with high pulse energies into reach [46, 47]. This is, together with the reduced heat generation due to the parametric nature of the amplification process, a striking advantage of OPAs compared with solid-state laser amplifiers.

Spontaneous decay of the pump photons into a signal and an idler photon can also occur during the amplification, called optical parametric fluorescence (OPF). This parasitic effect can generate a background on the amplified pulses, leading to a reduced temporal contrast. To avoid generation of OPF, a seed with sufficiently high pulse energy is needed.

The combination of OPA with the CPA technique to OPCPA greatly benefits the optical parametric amplification process [48, 49]. Not only can the intensity of the laser pulses in the amplification medium be tremendously reduced, it is also possible to use pump pulses in the picosecond range which can be generated by diode pumped solid-state lasers (see section 2.3).

OPCPA offers a variety of advantages compared to solid state CPA laser systems:

- A very high parametric gain can be achieved in a single OPCPA stage, the implementation of several amplifier stages or complicated multipass schemes can be avoided.
- OPCPA is not limited to laser transitions of active ions as in solid-state laser systems. A very broad bandwidth range can be amplified with OPCPA.
- Much weaker thermal effects in the amplification medium are to be expected than in solid-state laser systems since no energy storage in the medium is needed for the amplification. This allows for high average power amplification. In addition, the efficiency of an OPCPA is very high since there are nearly no losses in parasitic lasing of the medium.
- Given a good pump beam quality, which can be achieved for example by fiber laser systems, the output of the OPCPA stages will also have a very high beam quality.
- OPCPA allows for the generation of wavelength regimes where no laser material has transition lines. For example, wavelengths in the mid-infrared can be generated by using the generated idler instead of the amplified seed of the OPCPA.

However, despite the advantages of OPCPA, some disadvantages of this technique are the requirement of matching pulse durations of pump and signal and a precisely matched arrival time of the pulses in the amplification medium. In addition, the pump beam needs to match severe requirements: A high beam quality and high stability of the pulse energy as well as the pointing of the pump pulses are essential to operate a functional OPCPA system. Besides matching these requirements of the pump source, a careful dispersion management in the entire amplifier chain is also crucial [50]. Thus, very short pulse durations of OPCPA systems have been shown in the recent years, approaching the few-optical-cycle regime of the output pulses [28, 29, 51–53]. This in combination with the high achievable gain, lasers exceeding the terawatt range of pulse peak power have been shown in references [54–58].

2.3.3 Diode pumped solid-state lasers

Light amplification in diode pumped solid-state laser (DPSSL) systems relies on the population inversion of an upper and lower manifold in an active medium. The gain medium is pumped by a diode laser with an emission wavelength matching the best absorption cross section. Laser transitions then occur at the wavelength where the emission cross section is maximal for the medium. By seeding the pumped laser medium with photons matching the emission wavelength, stimulated emission occurs. This leads to the emission of photons with the same wavelength as the seed light, leading to the amplification of the incident beam. The amplification factor then depends on the strength of the population inversion between the upper and lower laser manifold and the intensity of the incident light.

Improvements on diode laser technology, such as very high pump powers and good beam quality, made high pump intensities available. Thus, DPSSL amplifiers have become powerful and easy to handle devices for the amplification of light. In addition, the use of three-level gain media such as Ytterbium YAG as laser active material has become feasible. A very high pump fluence is needed to populate the upper laser manifold in these quasi three-level systems (see section 2.4). Diode lasers used for pumping Neodymium and Ytterbium laser amplifiers rely on Gallium Arsenide (GaAs) as active medium. The emission wavelength can be chosen by fabrication to match the absorption transitions of the corresponding material. Highest output powers can be reached by combining several diodes to a diode bar, then combining diode bars to a stack and finally combining these stacks to an array. The output powers of these diode arrays are usually in the range of several hundreds of watts.

In the next sections, the three laser technologies used for the experimental setup are presented. This includes fiber laser systems, Innoslab technology as well as the thin-disk laser technology. The characteristics of these laser systems are compared, advantages and disadvantages for high power laser operation are explained, necessary properties to provide the pump pulses for an OPCPA system.

2.3.4 Rate equations

The foundation for the theoretical models used in this thesis is a set of basic rate equations. These equations describe the resonant linear interaction of a medium with light. The equation for populating the upper state is the following (equations taken from [31]):

$$\frac{dN_2}{dt} = \sigma_{12} \cdot I_p \cdot N_1, \tag{2.46}$$

where N_1 and N_2 are the lower and upper state population densities, σ_{12} is the transition cross section from the lower to the upper state and I_p is the intensity of the pump laser. For stimulated emission, the rate equation reads as follows:

$$\frac{dN_2}{dt} = -\sigma_{21} \cdot I_l \cdot N_2, \tag{2.47}$$

with I_l as intensity of the seed laser pulses and σ_{21} as transition cross section from the upper to the lower laser level. The rate equation for spontaneous decay of the upper state is:

$$\frac{dN_2}{dt} = -\frac{1}{\tau_{21}} \cdot N_2, \tag{2.48}$$

With these three equations, the dynamics of the upper state population in the gain medium can be fully described.

An important effect for amplifiers using a pumped gain medium is gain saturation. This is explained by the fact that an amplifier cannot have an arbitrarily high gain for high seed pulse energies. If a laser pulse is amplified in the gain medium, the number of excited laser ions will be reduced, reducing the population inversion for the further amplification. The Frantz-Nodvick equation can be used for modeling the gain and thus the output energy of the amplifier [30]:

$$E_{out} = E_{sat} \ln \left[1 + \exp\left(g_0\right) \left(\exp\left(\frac{E_{in}}{E_{sat}} \right) - 1 \right) \right], \tag{2.49}$$

where E_{out}, E_{sat} and E_{in} are the output, saturation and input energy, respectively. g_0 describes the initial gain value given by the amount of population inversion. The saturation energy is calculated by:

$$E_{sat} = A \cdot F_{sat} = \frac{A \cdot h\nu}{\sigma_{em} + \sigma_{abs}}, \tag{2.50}$$

with A as mode area of the seed beam, $h\nu$ as photon energy of the emission wavelength and σ_{em} and σ_{abs} as emission and absorption cross sections of the laser active material at the emission wavelength.

With the Frantz-Nodvick equation, the gain factor g_p for a pulse in the amplification medium can be calculated to:

$$\exp\left(g_p\right) = \frac{E_{sat}}{E_{in}} \ln\left[1 + \exp\left(g_0\right)\left(\exp\left(\frac{E_{in}}{E_{sat}}\right) - 1\right)\right]. \tag{2.51}$$

The effect of gain saturation is considered in the simulation described in chapter 3 by a reduced population inversion of the gain medium after each pass of the seed pulses on the thin-disk gain medium.

2.3.5 Fiber laser systems

In the past decades, a number of different fiber amplifier concepts has been developed. We use a rod-type fiber amplifier technique (rod length of 1 m versus a diameter of the active core of several tens of microns). The very large surface-to-volume ratio allows good heat removal in the fiber.

In the most simple version, a fiber amplifier consists of a glass fiber doped with a rare earth element [59]. The pump light propagates together with the seed beam in the fiber core. It is absorbed by the active dopant in the fiber, leading to an inversion of the laser levels. The co-propagating seed beam is then amplified. Using the same active core for pump and seed light puts strong constraints to the pump source, where diffraction-limited beam quality is needed to couple the pump light into the fiber. This limits the pump power and thus the output power of the amplifier. This is avoided by using a fiber with a large mode field area, which in contrast reduces the quality of the amplified output beam. A solution to this problem was the invention of the double-clad step-index fiber, where the seed beam is guided in the doped inner core of the fiber and the pump beam is guided in the inner cladding, which has a much larger mode field diameter (and numerical aperture). This has first been shown in reference [60]. A schematic of a double-clad fiber amplifier is shown in figure 2.6.

The advantage of this technique is the possibility to use a pump laser source with reduced beam quality, but higher output power, as for example the output of laser diodes. The high beam quality of the output is maintained near diffraction-limit. In continuous mode, the output power of this type of amplifier was increased step by step from 30 W in 1997 to far more than 1 kW for modern fiber laser designs [61–65], maintaining a very good beam quality of the amplified output.

It has to be considered that even with the technique of chirped-pulse amplification, the intensities of the amplified pulses reach very high values in the fiber gain medium due to the very small mode field area in the active inner core of the fiber. This leads to phase distortions of the pulses due to self-phase modulation and can in extreme cases lead to the destruction of the gain medium by self focusing of the beam in the active fiber core. This can be avoided by increasing the mode field diameter of the active core. On the other hand, as stated above, this would be accompanied by

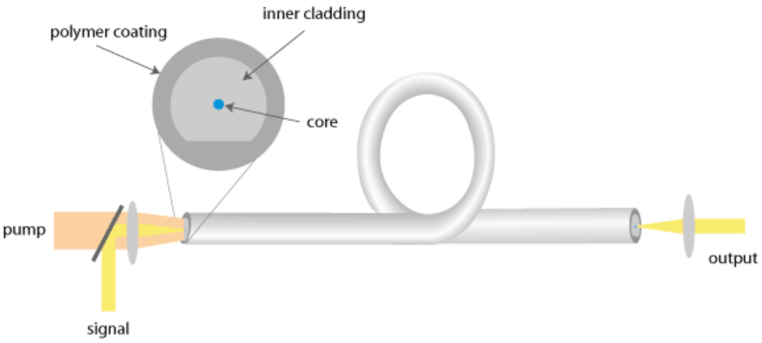

Figure 2.6: Schematic of the double-clad fiber technique [30]. The pump light is launched in the inner cladding of the fiber and overlapped with the active core. The seed light is guided and amplified in the inner core, leading to a good output beam quality.

a worse beam quality of the fiber output. To estimate if a fiber amplifier with large mode area can achieve single mode operation, it is useful to introduce a normalized frequency V (or V-parameter) which is dependant on the refractive indices of the core n_c and the cladding n_{clad} of the fiber as well as the effective mode field diameter a_{eff} [66]:

$$V = \frac{2\pi}{\lambda} a_{eff} \cdot NA = \frac{2\pi}{\lambda} a_{eff} \sqrt{n_c^2 - n_{clad}^2}, \tag{2.52}$$

where NA is the numerical aperture of the fiber. It can be shown that for $V < 2.405$ single-mode operation of the fiber amplifier can be achieved [67]. By careful fabrication of the fiber media, large-mode area (LMA) fibers with several 10 μm core diameter could be demonstrated [68–70]. Further discrimination of higher modes can be achieved by introducing tapered sections in the fiber [71]. Applying these techniques, the single-mode operation of a fiber amplifier with 50 μm core diameter was shown [72]. In this way, LMA fiber amplifiers with V-parameters between 5 and 10 could be manufactured. Although this value yields that the fiber is not operated in single mode, still very high beam qualities with M^2 values well below 1.5 can be reached. In addition to the fabrication of the refractive index step between core and cladding, bending losses can be introduced to discriminate the higher order modes in the fiber medium. This has been theoretically described in reference [73] and experimentally shown for example in reference [74]. A five orders of magnitude difference of the bending losses between the fundamental and the first higher mode can be reached.

Further modeling of the refractive index profile and thus improving the mode properties of a fiber can be achieved by introducing small air holes along the fiber core. This is then called a photonic-crystal fiber (PCF) [75]. Figure 2.7 shows a cut through such a PCF.

In this figure, the gray shaded area shows the glass rod of the fiber and the black

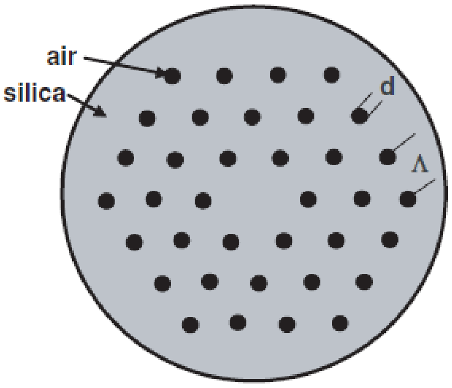

Figure 2.7: Schematic view of a photonic crystal fiber [65]. The gray shaded area indicates the the inner cladding for pump guiding, while the black dots show the air holes which are fabricated into the fiber. Λ and d are the hole distance (pitch) and the hole diameter, respectively. The left-out hole in the middle is used as active core for seed beam guiding in the fiber.

spots depict the air holes. Two important parameters of a PCF are the hole diameter d and the hole distance Λ, the so-called pitch. The laser mode is guided in the middle of the fiber, where one hole is missing. This area of the fiber can be doped with active ions for the amplification of laser radiation. For this type of fiber, the V-parameter defined in equation 2.52 can be modified to replace the effective mode-field diameter by the fact that the refractive index step is achieved by leaving the central hole out. The effective refractive index of the cladding is then dependant on the wavelength. The new V-parameter then is [65]:

$$V_{PCF} = \frac{2\pi}{\lambda}\Lambda\sqrt{n_c^2(\lambda) - n_{clad}^2(\lambda)}. \tag{2.53}$$

The single mode condition requires V_{PCF} to be smaller than π. The ratio between hole diameter and hole distance then gives the operation mode of the fiber amplifier. For values of $d/\Lambda > 0.4$, the fiber performs in single mode if the relation between the wavelengths of pump and seed is large enough. For $d/\Lambda < 0.4$, the fiber becomes single-mode for all wavelengths. In this regime, the fiber is called endlessly single mode, which has been demonstrated and theoretically described in [76, 77]. This endlessly single-mode behavior is known from step index fibers and can be used to scale the PCF to single-mode operation. For further scaling of the mode field diameter in the PCF amplifier, more missing holes can be introduced which was shown for example for three missing holes [78] or for seven missing holes with then more than 50 μm mode field diameter with fundamental mode guidance [79]. By surrounding the inner cladding of the fiber with e.g. a web of silica bridges, a double-clad PCF is formed [80, 81].

This increases the numerical aperture of the pump light, where the inner clad can be reduced in size, increasing the brightness of the pump source in the fiber amplifier [82]. In the recent years, a fiber amplifier capable of producing an output power of 830 W at a repetition rate of 78 MHz with femtosecond pulse duration has been demonstrated [83]. Further scaling of the mode area can be achieved by increasing the hole distance and diameters of the PCF amplifiers. If the distance reaches values of more than 10 times the wavelength of the guided light, the fiber is called a large-pitch fiber (LPF). With this type of fiber, average output powers of more than 290 W with beam quality less than $M^2 = 1.4$ have been reported [84]. In addition to that, recently a pulse energy of 26 mJ at a repetition rate of 5 kHz with nanosecond pulse durations has been shown [85].

The fiber amplifier technique used in this thesis is a large mode area PCF rod amplifier. It has the outer dimensions of a rod-type amplifier, which are typically in the range of a few millimeters, where a PCF is fabricated in the middle of the rod [86]. The length of the amplifier is limited to below 1 m. The nonlinearity of such fiber is very low, which allows high pump powers. The thickness of the outer cladding gives the fiber enough mechanical stability to avoid coating of the fiber, where usually damages occur at very high power extractions [87].

Fiber amplifiers are suitable for high average output power operation, but are restricted to high repetition rates and thus low pulse energies, where the peak intensities of the pulses are not in the regime for nonlinear interactions with the medium. This is of tremendous importance because the light propagates a very long distance in the fiber medium. This restriction can be circumvented by the method of coherent combination of different laser sources which has been developed in the recent years. There are different approaches to coherently combine fiber sources, for example combination in a polarizer [88, 89], where distinct polarizations of the single sources are combined, combination in tiled apertures [90, 91] or diffractive optical components [92]. All these techniques are capable of producing output powers in the kW range, but in any of these cases, a very sophisticated interferometrically stable setup is needed to provide timing and phase control of the amplified pulses in the combining element.

2.3.6 Innoslab amplifiers

Slab laser amplifiers, as the name suggests, have a slab shaped laser crystal as active gain medium. Pumping of the gain medium can be done either by surface or by edge pumping. The first possibility is favored for pump sources with very poor spatial coherence such as flashlamps. For pump sources with good spatial coherence, e.g. laser diodes, edge pumping is favored because of the increased length of the gain medium passed by the pump beam, leading to a higher pump absorption efficiency. An additional advantage of edge pumping is that the large surfaces of the crystal can be used for efficient cooling. This makes the technology suitable for high pump powers.

Difficult for slab amplifiers is the power extraction. This is because of the asymmetric shape of the laser gain medium. In the edge pumped geometry, where cooling is achieved over the large surfaces of the gain medium, a strong thermal lens evolves in the direction of the heat sinks. This thermal lens is one-dimensional, so that the laser beam is focused in one direction, but is unaffected in the other. One way of extracting the power is to use the Slab laser in a zig-zag geometry, where the laser beam follows a zig-zag path in the crystal, following the direction of the one-dimensional heat flow. This has the effect that the thermal lens averages out over the beam path. This has been shown for example in [93, 94]. Figure 2.8 shows a schematic of the geometry.

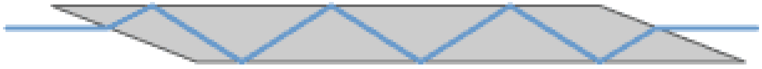

Figure 2.8: Zig-zag beam path in a slab crystal (side view) [30]. The seed beam is coupled into the crystal at brewster angled facets to keep the coupling losses low. The beam is then kept in the crystal by total internal reflection, following a zig-zag path in the laser crystal.

The beam is kept in the crystal by total internal reflection at the boundaries, except at the brewster angled in- and outcoupling edges of the slab medium. Pumping of the gain medium occurs perpendicular to the amplified seed beam. With this type of amplifier a very high output power can be reached with good beam quality. Average output powers of 1 kW have been shown with a Nd:YAG zig-zag slab laser [95].

A disadvantage of this type of power extraction is that only a fraction of the pumped gain medium is used for amplification. This leads to problems in the power extraction efficiency and also to parasitic lasing in the regions where no seed is present. A workaround for this effect is to fold the beam several times through the amplification medium in the plane perpendicular to the thermal lens. This can then be used to reproduce the beam waist at every pass of the seed in the amplification medium, leaving the beam size in the other axis constant. This way, a much better use of the gain medium can be achieved, leading to a suppression of parasitic lasing.

The slab laser amplifier used in the frame of this work is based on Innoslab technology (compare [16]). The large surfaces of the crystal are mounted in a heat sink to provide good heat removal. Pumping of the gain medium is achieved by diode laser stacks which are focussed to a line into the crystal by external optics. This is performed in the direction of the seed laser beam. Figure 2.9 shows a schematic of the setup.

The seed beam is folded through the crystal several times by a confocal arrangement of curved mirrors. This way, the laser mode is reproduced in the direction of

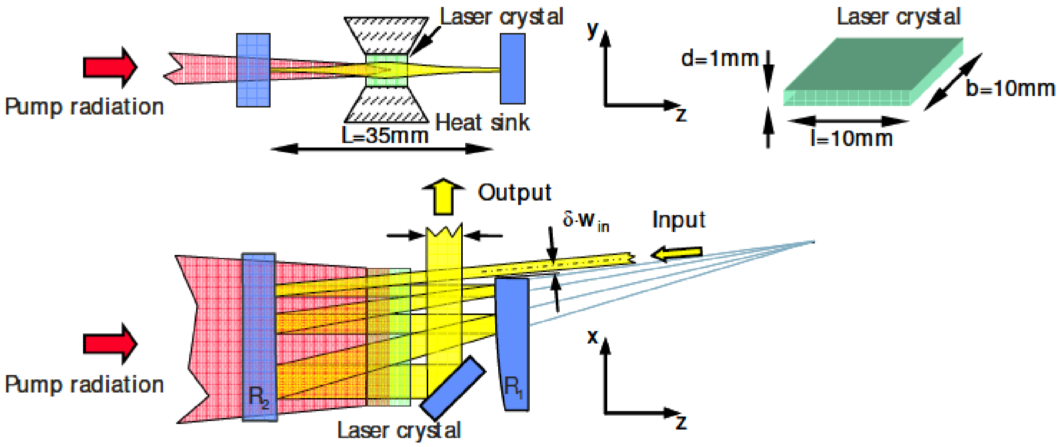

Figure 2.9: Schematic of the Innoslab setup [16]. Top left: Top view of the Innoslab multipass arrangement. The mode of the seed beam is reproduced during each pass of amplification by the thermal lens evolving in the gain medium. Bottom left: Side view of the multipass arrangement. The seed beam is expanded for every pass through the multipass by a confocal arrangement of two curved mirrors with radii of curvature R_1 and R_2. Top right: Schematic of the slab crystal as it is used in the experimental setup.

the thermal lens with every pass and expanded in the other direction by a constant factor. The intensity of the amplified beam is kept constant throughout the entire amplification process, which leads to a constant amplification factor with every pass. With this arrangement, very high amplification factors of up to 1000 can be achieved without reaching the damage threshold of the gain medium or the amplifier optics, which is then restricted to the amplification of pulses in the nanosecond regime. The great advantage of this method for power extraction is that the entire gain medium is used for the amplification of the incident beam, leading to very high pump-to-seed conversion efficiencies and the suppression of parasitic lasing. An output power of 400 W has already been shown in [16].

For the amplification of short pulses in the picosecond regime to high pulse energies, the CPA technique described in section 2.3.2 can be used. Seeding can be performed with fiber laser amplifiers which deliver a broad bandwidth. This has been shown in reference [96], where a spectral bandwidth of a fiber amplifier supporting compression to 720 fs at repetition rates of 100 kHz up to 1 MHz has been demonstrated.

Further scaling of this amplifier technique can be achieved by using a second amplifier stage with only one pass through the amplifier medium. The beam then needs to be matched to the aperture of the amplifier crystal, which demands a strongly elliptical beam mode. This can be achieved by an arrangement of spherical and cylindrical lenses to prepare the beam for the amplification and bringing it back to a round mode shape after the amplification. An amplifier with a multipass amplification stage and a single pass booster amplification stage has been demonstrated with an output power of 1.1 kW [97].

2.3.7 Thin-disk amplifiers

Thin-disk laser amplifiers have a very thin laser active medium. The technology was first introduced in the year 1994 [17]. The thin-disk can then be considered as an active mirror for the amplification of light (for example as end mirror in a cavity). The difference to slab and rod type lasers is the large aspect ratio of the gain medium, which is the ratio between the diameter of the gain medium and its thickness. The front surface of the disk is coated for maximum transmission of the seed and the pump light, while the back plane is coated for maximum reflection of both wavelengths. A schematic of the thin-disk concept is shown in figure 2.10.

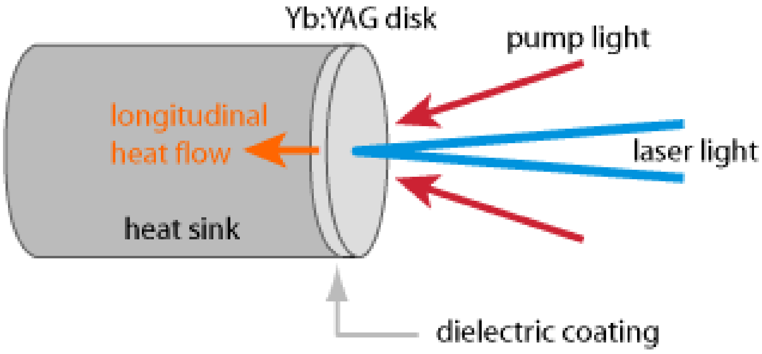

Figure 2.10: Concept of the thin-disk laser geometry [30]. The face-pumped configuration is shown, where the pump light is coupled on the gain medium with an angle on the front surface of the disk. The seed beam is coupled perpendicular to the pumped area. Reflection of pump and seed light is performed by a high reflectivity coating on the back face of the disk, double passing the disk gain medium. The heat sink on the back of the disk provides a 1-dimensional heat flow through the gain medium which drastically reduces the effect of thermal lensing in this type of configuration.

The disk gain medium is mounted to a heat sink which provides very efficient cooling of the medium due to its small thickness, where the heat generation takes place very close to its surface. Thus, only weak thermal lensing will occur in the disk because of the low thermal load and the one-dimensional heat flow pointing in the direction of the amplified beam. Power scaling of thin-disk lasers can be achieved by increasing the mode field diameter on the gain medium. For example, for doubling the pump power, the pumped area needs to be doubled to keep the intensity and thus the heat generation in the gain medium constant. The thermal lens will then be reduced by the doubled cooling surface of the disk, which just compensates the increased sensitivity on thermal changes of the refractive index due to the larger mode field of the seed beam. The power scaling is thus not limited by thermal lensing or stress of the disk gain medium, but by the difficult fabrication of disks with very large aspects ratios. Due to these properties of the gain medium, near diffraction-limited output beams with very high output powers can be realized [98–100].

Pumping of the gain medium can be achieved either by edge-pumping or by face-pumping (see figure 2.10 for the latter case). Both methods have their advantages and disadvantages. The advantage of edge-pumping is that the effective length of the gain medium is very large, leading to a very efficient absorption of the pump light. This also puts low constraints to the pump light source. Laser diodes can be used which are directly placed at the edges of the disk. But since most of the pump light is then absorbed at the edges of the disk, it has the disadvantage that the power distribution in the active medium is not homogeneous in the seeded area (which is the center part of the thin-disk). For face-pumping, a homogeneous distribution of the pump light at the area where the seed beam is present can be attained. In contrast, a pump light source with a high beam quality is required. This can be achieved for example by using the output of a fiber laser, which has very good beam quality. Another possibility is to use the direct output of laser diodes and implementing a homogenizer setup to obtain a homogeneous pump beam profile on the disk. Thus, face-pumping of the gain medium is the preferred method. A problem is that due to the small thickness of the gain medium, many pump passes on the disk are required for efficient absorption of the pump light. This is performed by reflection of the pump beam several times on the disk by a large parabolic mirror and retro-reflecting mirrors, which is shown in figure 2.11.

Due to the small thickness of the thin-disk gain medium, a very low single pass gain around 1.2 is achieved for power extraction. A large number of passes is needed for efficient laser operation. This can be attained in different ways, depending on the thin-disk laser setup as oscillator or amplifier. In the case of a thin-disk oscillator, a high number of passes is intrinsic to the cavity design. The small nonlinearities caused by the use of a thin gain medium together with the power scaling properties of that concept lead to highest output powers for mode-locked laser operation. These reach values of more than 140 W, reported in [101, 102]. For an amplifier system operated in vacuum, the output power could even be increased to 275 W [103]. Pulse energies of several tens of μJ were reported for picosecond and sub-picosecond pulse durations [104–106]. Even pulse durations of around 200 fs are possible using the large emission bandwidth of Yb:YAG as gain medium (see section 2.4) [107, 108].

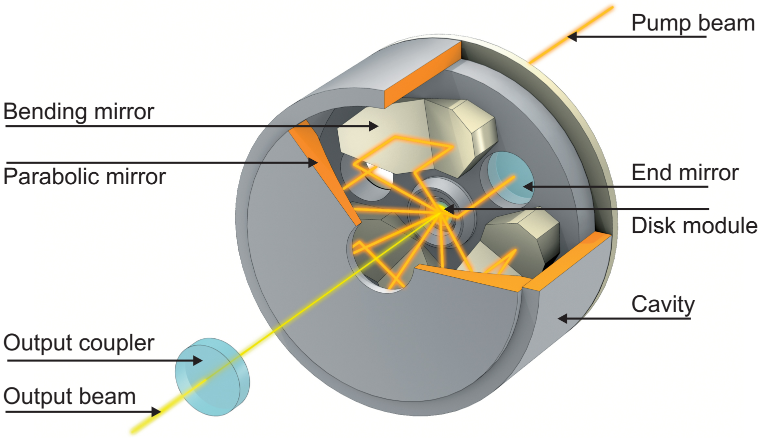

Figure 2.11: Multipass cavity for the pump beam in a thin-disk laser head [Trumpf Laser GmbH]. The pump beam is coupled through a window on the back side of the cavity and projected onto the disk by a parabolic mirror. After each pass on the disk, the beam is projected to a new path by prism shaped bending mirrors. An end mirror sends the pump beam back after 12 passes on the gain medium for optimal pump absorption in the gain medium. The seed beam is coupled onto the disk through a hole at the center of the parabolic mirror.

The laser head can be used as active element in a regenerative amplifier for reaching higher output powers with thin-disk technology [109, 110]. This is achieved by coupling the seed beam into an amplifier cavity by a polarizer and a Pockels cell. A large number of round trips on the gain medium is possible. A schematic of a regenerative amplifier using a thin-disk laser head is shown in figure 2.12.

With this type of amplifier, high output powers at high repetition rates can be achieved [111, 112]. For example, output energies of 25 mJ with picosecond pulse duration at 3 kHz repetition rate has been shown in reference [113]. A limiting factor on this technique is the use of an active switching element in the cavity, which adds a nonlinear phase contribution to the amplified pulses. This limits the output pulse energy of regenerative amplifiers to several 10 mJ.

In order to circumvent the limiting factor of the active switching element, the thin-disk laser head needs to be operated in a multipass setup. This avoids passing the light through material and thus tremendously reduces the nonlinearities in the amplification process. Therefore, every pass on the disk needs a new beam path. A large amount of mirrors is needed to form the multipass. This makes the technology vulnerable to fluctuations of beam pointing and temperature drifts. A workaround for this stability problem is relay imaging of every pass on the disk. In spite of this

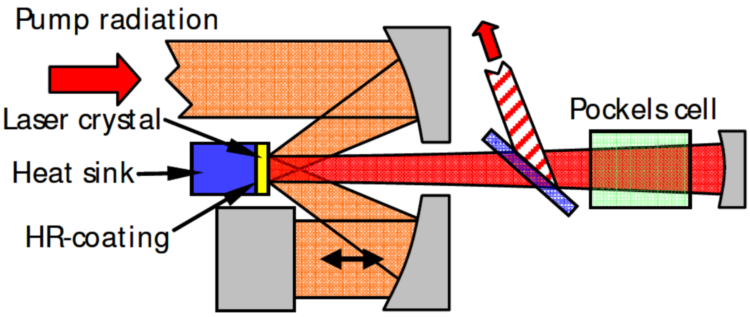

Figure 2.12: Schematic of a thin-disk regenerative amplifier [16]. The pump beam is folded to the disk gain medium by a parabolic mirror and retro-reflecting prism mirrors. The seed beam is coupled into and out of the cavity by a thin-film polarizer and a Pockels cell.

limitation, with a careful alignment of the multipass, pulse energies in the joule range are possible at low repetition rate [114]. At high repetition rates in the kHz regime, pulse energies in the mJ range are possible [115, 116], leading to output powers of several kilowatts.

A very important limiting factor for the efficiency of operation of a thin-disk laser is the influence of amplified spontaneous emission (ASE) on the amplifier dynamics due to the properties of the thin-disk gain medium. This effect has been described for large-aperture disk lasers in [117, 118]. The origin of the ASE in the disk laser is spontaneous emission of the upper states. This is radiated isotropically into the medium, where a certain fraction will be re-absorbed in the gain medium due to the quasi three-level nature of the gain material Yb:YAG. But some fraction of the ASE can be back reflected at the disk boundaries by total internal reflection (TIR) into the pumped area of the gain medium where it will be further amplified. The total internal reflection angle is calculated by:

$$\alpha_{TIR} = \arcsin \frac{n_{air}}{n_{disk}}, \tag{2.54}$$

with the refractive indices n_{air} and n_{disk} of air and the disk medium. The spontaneous emitted photons can pass the pumped region of the disk several times, leading to a strong amplification. This reduces the inversion available for the seed photons. More detailed descriptions of the ASE dynamics are given in [119–122]. Since the dimension of the gain medium in forward direction is very small and in addition to that the front face of the disk has an anti-reflective coating, ASE modes can only evolve perpendicular to the large surfaces inside the disk medium. Therefore, ASE does not contribute to any noise of the amplified seed beam. The different ASE modes are summarized into two categories: The ring-type modes, which evolve in the plane of the disk and are reflected by the boundaries such that a ring-type trajectory is created, and the transversal modes which directly pass the pumped region of the disk, performing a zig-zag path through the gain medium. Figure 2.13 shows the two different ASE modes which can evolve in the disk.

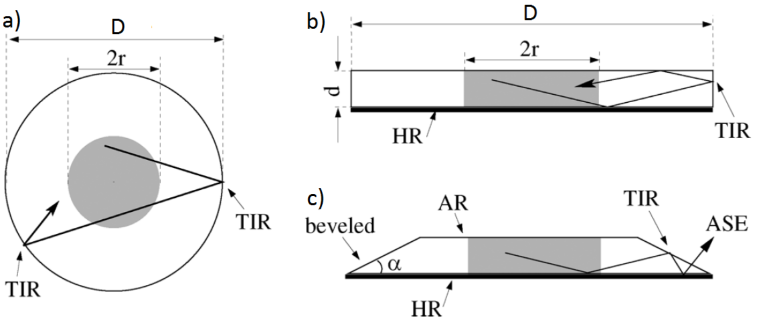

Figure 2.13: ASE modes in a disk gain medium (gray shaded area is the pumped region): a) ring-type modes which are kept inside the disk by total internal reflection only at the disk boundaries, b) transversal modes which are kept in the disk by total internal reflection at the disk surfaces and the boundaries and c) reduction of transversal modes by beveling the disk boundaries [123].

From this figure, it can be seen how different ASE modes are kept in the gain medium by means of total internal reflection. In the past, different approaches to suppress these ASE modes have been developed. To reduce the ring-type modes, the pump spot size has to be smaller than the minimum distance of the ASE modes to the center of the disk. This distance is given by [124]:

$$R_{min} = \frac{D_{disk}}{2} \sin \alpha_{TIR} = \frac{D_{disk}}{2} \frac{n_{air}}{n_{disk}}. \tag{2.55}$$

The second approach, as already shown in figure 2.13, is to bevel the boundaries of the disk gain medium to transmit the transversal modes out of the medium. Another more sophisticated approach is to introduce a so called anti-ASE cap onto the disk, an undoped layer where the ASE is not further amplified. This has for example been shown in reference [125]. Additionally, the boundaries of the disk gain medium can be coated with an ASE-absorbing layer which reduces the amount of back-reflected photons in the pumped region.

2.4 Spectral properties of Yb:YAG

In the past decades, various laser active materials have found application in solid-state lasers. The most prominent examples are Titanium Sapphire (Ti:Sa), Neodymium doped Yttrium Aluminium Garnet (Nd:YAG) and Ytterbium doped Yttrium Aluminium Garnet (Yb:YAG). These materials are used in different types of amplifier where their best properties are exploited.

The laser active material used for the amplifiers in this thesis is Yb:YAG. The emission wavelength of Yb:YAG is centered at 1030 nm and the pump wavelength is around 940 nm. Table 2.1 gives an overview of the properties of the host material YAG.

Property	Value	Units
Index of refraction	1.8173	
Dispersion	760	$\mathrm{fs}^2/\mathrm{cm}$
Nonlinear index	12.4	$10^{-16}\,\mathrm{cm}^2/\mathrm{W}$
Thermal expansion	7.8 - 8.2	$10^{-6}\,\mathrm{K}^{-1}$
dn/dT	8.9	$10^{-6}\,\mathrm{K}^{-1}$

Table 2.1: Properties of the host material YAG [126].

The laser ions used in the host material YAG stated in table 2.1, Ytterbium and Neodymium, have very different properties which are compared in the tables 2.2 and 2.3. The material used in this thesis is Yb:YAG, which is a quasi-three-level gain medium and has advantages compared to Nd:YAG, but also some disadvantages due to its quasi three-level system (compared to the four-level system Nd:YAG). Figure 2.14 shows the energy level scheme of Yb:YAG with the corresponding laser transitions and the partition function values for the occupation of the different energy sublevels. The transition wavelengths of the different sub-levels are also shown in this figure.

The following list gives the motivation for the choice of Yb:YAG as laser active medium in the amplifiers used in the context of this thesis and for the development of the thin-disk amplifier:

- Yb:YAG has a very small quantum defect, which leads to a efficient pumping without excessive generation of heat in the active medium, reducing the cooling requirements for high average power laser amplifiers. The quantum defect energy E_q is calculated as [30]:

  $$E_q = E_{pump} \cdot \left(1 - \frac{\lambda_{pump}}{\lambda_{laser}}\right), \tag{2.56}$$

  with $E_{pump} = h\nu_{pump}$ the pump photon energy and λ_{pump} and λ_{laser} the pump and laser emission wavelength, respectively. If equation 2.56 is divided by the pump photon energy, the quantum defect can be calculated. Table 2.2 gives an overview of the quantum defects of the three laser active materials stated at the beginning of this section (from [31]).

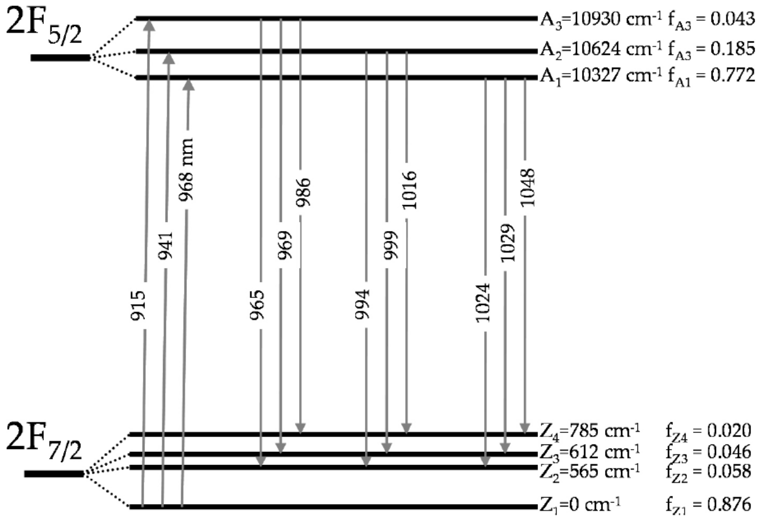

Figure 2.14: Energy level scheme for Yb:YAG [127]

Laser material	λ_{laser} (nm)	λ_{pump} (nm)	E_q/E_{pump} (%)
Yb:YAG	1030	940	8.7
Nd:YAG	1064	808	24
Ti:Sa	800	532	34

Table 2.2: Quantum defects of different laser materials.

From this table, it is obvious that due to its very small quantum defect compared with other laser active materials, Yb:YAG is the most suitable for high power laser operation.

- Yb:YAG also offers a large gain bandwidth, which is important for the generation of short pulses. Figure 2.15 shows the wavelength dependent absorption and emission cross sections of Yb:YAG.

  The main absorption peaks of Yb:YAG are located at 915 nm, 941 nm and 968 nm and the emission peak wavelength is located at 1030 nm. Table 2.3 gives an overview about the spectroscopic properties of the absorption and emission behaviors of Yb:YAG and Nd:YAG (all values given for 300 K).

- The upper-state lifetime of the Ytterbium ions in the laser active medium is on the order of a millisecond, which is high compared to other gain mediums. This is very important for the use of this gain medium as burst-mode amplifier, since an efficient pre-pumping phase is possible only with a reasonable high lifetime. The lifetime depends on the doping concentration. Table 2.4 gives an overview of the upper state lifetimes for different doping concentrations.

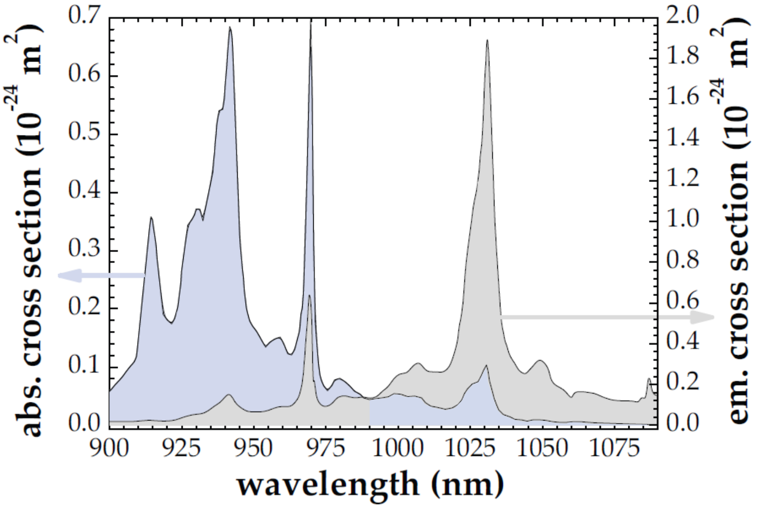

Figure 2.15: Emission and absorption cross sections for Yb:YAG [127]

Parameter	Yb:YAG	Nd:YAG	Units
pump transition wavelength	941	818	nm
pump transition peak cross-section, σ_p	0.7	6.7	10^{-20}cm^2
pump transition linewidth	18	<4	nm
laser transition wavelength	1030	1064	nm
laser transition peak cross-section, σ_l	2.1	21	10^{-20}cm^2
laser transition linewidth	6	0.6	nm

Table 2.3: Spectroscopic properties of Yb:YAG and Nd:YAG [128].

For a doping concentration of 7 at. %, which is used for the thin-disk lasers presented in this thesis, the fluorescence lifetime of 951 μs is used for the theoretical modeling. Measurements on the temperature dependence of the lifetimes show that for a temperature region between 150 and 400 K, which is the temperature region for the thin-disk laser, the lifetime can be considered as constant [132].

In spite of all these advantages of Yb:YAG as laser active medium, the quasi-three level nature of this material has to be considered. This leads to a very strong re-absorption of the amplified seed. Thus, very high pump intensities are required in order to counteract the reabsorption. This is, as stated in section 2.3.3, possible with very high power laser diode arrays.

Concentration [% at.]	Lifetime τ_f [μs]	Source
<1	949	[129]
<10	951	[130]
<15	955	[131]

Table 2.4: Fluorescence lifetimes of different doping concentrations in Yb:YAG.

Chapter 3

Analytical model of the thin-disk amplifier

An analytical model of the thin-disk multipass amplifier is presented in this chapter. Based on the basic rate equations of the laser medium, a quasi-2-dimensional model is developed. The model includes the losses due to amplified spontaneous emission (ASE). The model is used to simulate the output power and energy characteristics of the amplifier setup in different configurations. The special challenge for the modeling of the amplifier in this case is the simulation of the amplification of an entire burst pattern. This leads to a divided calculation of the amplifier in two steps, first a pre-amplification phase, where population inversion of the active gain medium by the pump light is established, and after that the main amplification phase of the input burst pattern. According to the burst-mode amplification of pulses with a burst repetition rate of 10 Hz, the laser amplifier is never operated in an equilibrium due to the fact that the upper state lifetime of the laser active ions is much smaller the the time between two bursts. This has to be taken into account in the simulation. First, the layout of the model is given in section 3.1. After the introduction to the model, the implementation of the rate equations into the MatLab code is given in section 3.2. With the simulation tool set up, first the influence of different parameters on the amplification characteristics are given without the influence of ASE (section 3.3), followed by the implementation of ASE in the code in section 3.4.

3.1 Layout of the model

In the setup, the disk gain module is modeled as a two-dimensional medium with a thickness d and a spatial width D. Figure 3.1 shows the layout of the disk as it is used in the analytical model together with the directions of the pump and seed beam as well as the ASE modes as implemented in the model.

Pump and seed beam are coupled to the disk on the large surface D. The pump

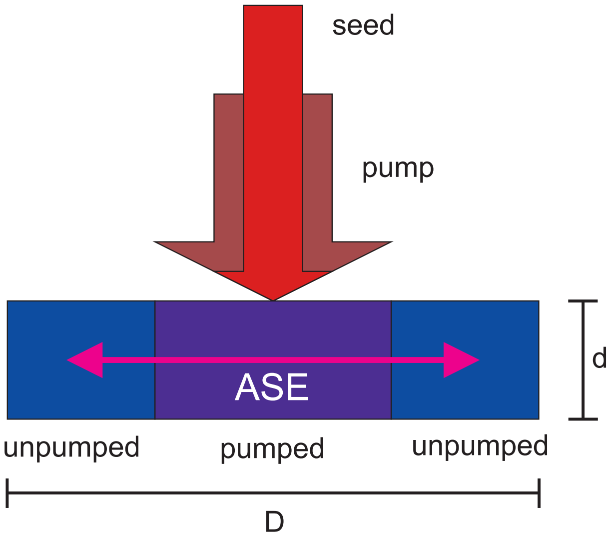

Figure 3.1: Layout of the disk in the analytical model. The disk with diameter D and thickness d is pumped on the face plane, leading to a pumped area marked in purple. This area is then seeded by the pulses which are to be amplified. ASE modes develop in the transversal direction, are amplified in the pumped area and reabsorbed in the remaining unpumped areas. Reflection of the ASE modes then occurs at the boundaries of the disk.

light then creates population inversion in the center part of the disk with the intensity given by the spatial characteristics of the pump light together with the pump power, which is then seeded with the seed pulses of the amplified beam. For the creation of population inversion and for the amplification of the seed pulses, the only dimension used in the simulation is the thickness d of the disk module. The ASE is modeled by radial modes which pass the pumped region of the disk where the ASE is amplified, then passes the unpumped region of the disk where reabsorption of the ASE takes place and after that the modes are back-reflected by the disk boundaries for another round-trip. For the modeling of the ASE, the corresponding dimension is the spatial width D of the disk.

As already stated at the beginning of this chapter, the dynamics of the simulation are divided into two steps, the pre-amplification phase and the main amplification phase. The pre-amplfication phase is needed to reach a certain state of population inversion in the laser active medium such that the first pulse of the burst pattern experiences an amplification similar to the subsequent pulses of the burst. A schematic block diagram of the simulation is shown in figure 3.2.

The simulation is set up such that during the pumping time the arising ASE gets directly amplified while the inversion is created by the pump light. This is due to the

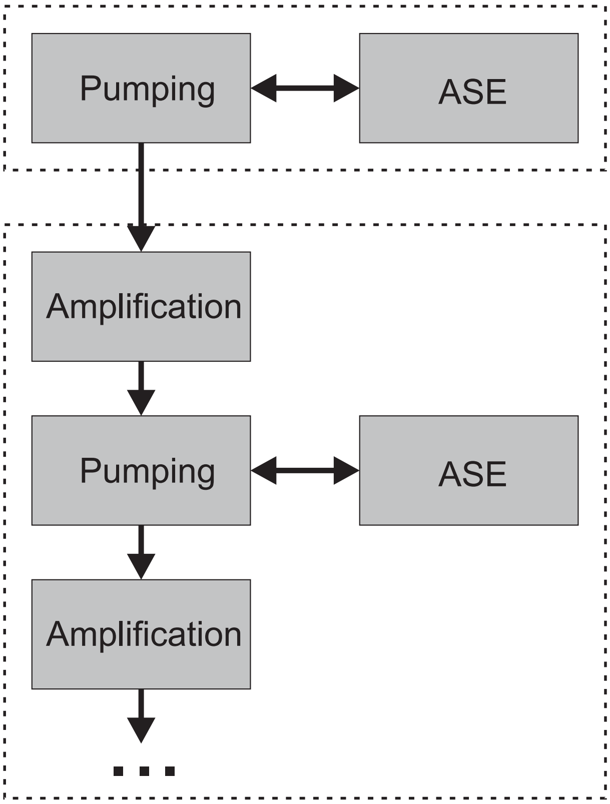

Figure 3.2: Block diagram of the analytical model. Starting with the pre-amplification phase in the upper dashed box, the population inversion in the active medium is modeled. Subsequently, the main amplification phase follows in the lower dashed box, where the pulses in the burst pattern are amplified with intermediate pumping of the gain medium.

direct coupling of the dynamics of pumping the laser gain medium with the dynamics of the ASE development in the disk. The amplification of the spontaneous emission directly decreases the number of active ions in the upper level manifold. After the pre-pumping phase is completed, the first pulse of the pulse train (burst) is amplified with a given number M_r of passes on the gain medium. After amplification of this pulse, the medium is re-pumped by the pump source, whereafter the second pulse of the burst gets amplified. This scheme is continued until the amplification of all pulses in the burst is modeled. Since the time scale on which the amplification occurs (up to 120 m multipass length, passed by a pulse in 400 ns) is very short compared to the time scale in between the pulses (10 μs for 100 kHz repetition rate), the dynamics of ASE don't need to be modeled during the amplification of the laser pulses. The pre-pumping time needs to be chosen such that all pulses in the burst experience approximately the same amplification and thus a flat burst shape is modeled.

3.2 Implementation of the rate equations

The model based on the basic rate equations stated in chapter 2.3.1 is implemented in a MatLab code. Pumping the gain medium is combined with the spontaneous decay of the active ions in the upper state manifold. To account for the dynamics of the upper state with the spontaneous decay and the rise of ASE, the pumping is divided into finite steps in the temporal domain. The rate of creation of the population inversion is then modeled by:

$$dN_2 = \frac{\Delta T}{N_{steps}} \left(\frac{1}{\hbar\omega_p} \eta_{abs} \frac{I_p}{d_{cr}} - \frac{N_2}{\tau_f} \right). \tag{3.1}$$

The term in front of the brackets describes the time steps used for the pumping with N_{steps} as the number of steps used in the simulation. To minimize the error introduced by the dynamics of ASE and pump absorption in the gain medium, a number of 100 steps was found to be the optimal value for the simulation. With less steps, there would be an influence on the dynamics by means of reducing the total created population inversion in the active medium. With a higher number of steps, the dynamics of the simulated results are similar, but the processing speed of the simulation is reduced. The value ΔT is the time required for pumping the material. In the case of the pre-pumping phase, this is given by the pre-pumping time while for the amplification phase it is given by the pulse repetition rate of the amplified seed. The second term in the brackets describes the spontaneous decay of the upper state level with density N_2 and the upper state lifetime τ_f. The first term in the brackets then describes the pumping of the gain medium with the photon energy of the pump light $\hbar\omega_p$, the pump light intensity I_p and the thickness of the material d_{cr} which is passed by the pump light. For a full description of the upper state dynamics, saturation effects have to be taken into account. This is achieved by the absorption efficiency η_{abs} of the pump photons in the material:

$$\eta_{abs} = 1 - \exp\left[-M_p d_{cr} \left(\sigma_{abs,p} N_{dop} - (\sigma_{abs,p} + \sigma_{em,p}) N_2\right)\right], \tag{3.2}$$

with M_p as the number of pump passes on the disk, N_{dop} as the doping concentration of the laser active material and $\sigma_{abs,p}$ and $\sigma_{em,p}$ as the absorption and emission cross sections of the material at the pump wavelength. After each step of pumping, the density of the upper state level is calculated by:

$$N_2(n+1) = N_2(n) + dN_2. \tag{3.3}$$

With these equations, the pump absorbtion of the active material is fully described. The rise of the ASE photons in each time step is then described by the spontaneous decay of the upper state manifold:

$$dN_{ASE} = \frac{\Delta T}{N_{steps}} \eta_{ASE} \frac{N_2}{\tau_f}. \tag{3.4}$$

The efficiency term η_{ASE} is introduced, which originates from the fact that the fluorescence is emitted isotropically and with the full spectral range which is shown in figure 2.15. To account for the directions where the photons are emitted, the angular distribution which contributes to ASE is calculated by using the total internal reflection at the disk faces and boundaries. The relative fraction of the total created photons contributing to ASE is calculated to 62,86 %. The contribution of the spectral fraction of ASE is calculated by integrating the fluorescence spectrum and comparing it with the fraction which will be amplified by the population inversion of the gain material. This fraction is calculated to be 16 %. The total density of ASE photons in the gain medium is then derived according to equation 3.3:

$$N_{ASE}(n+1) = N_{ASE}(n) + dN_{ASE}. \tag{3.5}$$

For the amplification of the ASE photons, two different gains for the different regions of the disk have to be defined. The general description of the small signal gain of the laser active material is given by:

$$g = N_2(\sigma_{em,l} + \sigma_{abs_l}) - N_{dop}\sigma_{abs,l}. \tag{3.6}$$

The emission cross section $\sigma_{em,l}$ and the absorption cross section $\sigma_{abs,l}$ of the laser wavelength are used. The ASE photons then pass two different regions of the disk, the pumped and the unpumped region. The amplification factor is given by:

$$dN_{ASE} = N_{ASE}(\exp(g \cdot d_{mat}) - 1), \tag{3.7}$$

where d_{mat} is the distance traveled by the ASE photons in the material. This is for the pumped region the size of the pump spot and for the unpumped region given by the diameter of the disk reduced by the pump spot size. After each passage of the photons through the corresponding parts of the disk, the total number of exited state ions is reduced by dN_{ASE}, while the number of ASE photons in the disk is increased by the same amount. After each passage, reflection losses at the disk boundaries need to be taken into account, reducing the total number of photons at each reflection. For the thickness of the material passed by the ASE photons, the angular distribution also has to be taken into account. This has already been done for the calculation of the fraction of spontaneous emitted photons contributing to the ASE. The effective thickness is achieved by calculating the path lengths at each emission angle of the spontaneously emitted photons in the disk and averaging over all these path lengths. This leads in our case to a factor of 1.4, which has to be multiplied to the value d_{mat} in order to obtain the real path length for the individual photons.

Finally, the amplification of the seed laser pulses E_{sig} for each individual pass on the disk module is included in the model. This is done with following equation:

$$E_{sig,out} = E_{sig,in} \cdot \sqrt{1-L} \cdot \exp(g \cdot d_{cr}), \tag{3.8}$$

where g is the small signal gain given in equation 3.6 and d_{cr} is the thickness of the thin-disk. Same as for the pump absorption, this takes into account the double pass of the seed pulses during every single pass through the multipass setup. The factor L is a dimensionless loss parameter which has to be taken into account due to the large amount of optics used in the multipass. This can be kept very small because of the quality of the mirrors used in the experimental setup (reflectivity well above 99 %). The reduction of the active ions in the upper state is then described by:

$$N_{2,after} = N_{2,before} - g\frac{I_{sig}}{\hbar\omega_l}, \tag{3.9}$$

with the intensity I_{sig} and the photon energy $\hbar\omega_l$ of the seed pulses. This calculation has to be performed for every pass of the seed pulses on the thin-disk. The total number of passes is then given by M_r. Table 3.1 gives a summary of the parameters used for the simulation.

Parameter name	Formula sign	Value	Units
Pre-pumping time	ΔT	< 500	μs
Re-pumping time	ΔT	10	μs
Temperature	T	293.15	K
Pump photon energy	$\hbar\omega_p$	$2.11{\cdot}10^{-19}$	J
Pump absorption cross section	$\sigma_{abs,p}$	$3.97{\cdot}10^{-25}$	m^2
Pump emission cross section	$\sigma_{em,p}$	$8.39{\cdot}10^{-26}$	m^2
Pump spot size (FWHM)	d_{pump}	7.35	mm
Pump power	P_{pump}	12.4	kW
Number of pump passes	M_p	24	
Pump beam shape		Supergaussian	
Seed photon energy	$\hbar\omega_l$	$1.93{\cdot}10^{-19}$	J
Seed absorption cross section	$\sigma_{abs,l}$	$1.29{\cdot}10^{-25}$	m^2
Seed emission cross section	$\sigma_{em,l}$	$2.16{\cdot}10^{-24}$	m^2
Seed spot size (FWHM)	d_{seed}	2.0	mm
Seed pulse energy	E_{seed}	375	μJ
Number of seed passes	M_r	30	
Number of pulses in burst		80	
Seed beam shape		Gaussian	
Crystal thickness	d	360	μm
Crystal diameter	D	17	mm
Doping concentration	N_{dop}	7	% at.
Fluorescence lifetime	τ_f	951	μs
Multipass losses	L	0.001	

Table 3.1: Parameters used for the simulation.

With all these equations and the corresponding parameters, the dynamics of the thin-disk amplifier can be simulated for different experimental parameters.

3.3 Results without ASE

As described already in section 2.3, the ASE modes develop mainly in the transversal direction in the thin-disk gain medium. Thus, ASE can not directly be measured in the thin-disk setup because it is not reachable with measurement devices. So first modeling is achieved without the influence of ASE to give an estimation of the maximum achievable output power with the thin-disk laser amplifier.

3.3.1 Influence of pre-pumping time

The first investigation done with the code is the influence of the amount of pre-pumping time on the burst shape. Therefore, one simulation was done without any pre-pumping time and one simulation with a too large amount of pre-pumping time. The resulting burst shapes of these simulations are displayed in figure 3.3.

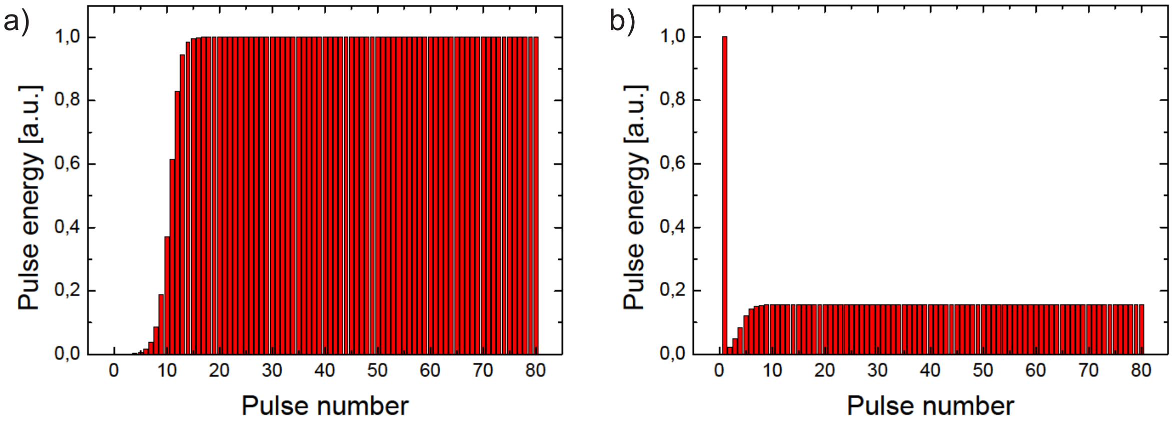

Figure 3.3: Burst shapes of the amplifier output: a) No and b) too long pre-pumping time. In the case of no pre-pumping time, population inversion is established during the burst which leads to a reduced amplification of the first couple of pulses. In the case of too much pre-pumping time, the first pulse in the burst experiences a very high amplification, depleting the population inversion which leads for the second pulse to the behavior of the case of no pre-pumping time.

In the first case, where the pre-pumping time is zero, the first pulses in the burst encounter only a very low population inversion in the active gain medium and are not fully amplified. The population inversion is then established during the burst by the intermediate pumping of the gain medium. This leads to an asymmetric burst shape with a rising edge at the beginning of the burst. In the second case, where the pre-pumping time is very long, the first pulse of the burst encounters a very high population inversion in the gain medium, which is far above the inversion level which is needed to establish a flat burst with approximately the same amplification for all pulses in the burst. Thus, the first pulse is amplified to a very high energy level, depleting the population inversion for the subsequent pulses. The inversion level for a flat burst shape then has to be re-established during the remaining part of the burst. Choosing a too long pre-pumping time can be dangerous for the optics used in the experimental setup, as the first pulse can be amplified to an energy level above the damage threshold of the optics and the thin-disk gain medium used in the setup. The experimentally and theoretically found optimum of the pre-pumping time to achieve a flat burst shape has been found to be $300\,\mu$s.

3.3.2 Influence of doping concentration

For the investigation of the influence of the doping concentration on the amplification in the thin-disk amplifier, the code was used with a total number of 30 passes on the thin-disk gain medium. The pre-pumping time was chosen such that a flat burst is generated in the output of the amplifier. Figure 3.4 shows the maximum achievable output burst energy in dependence on the doping concentration in a region of 1 to 20 at. %.

The total output energy of the amplifier is increasing to a maximum at around 7 at. % doping concentration. If this value is exceeded, the output energy starts to decrease for higher doping levels of the active medium. This is explained by reabsorption of the light in the active ions which depends on the total number of active ions in the medium. With a high level of doping concentration, the pump is absorbed by a fraction of the active ions, leaving a certain amount of them in the lower level. Due to the quasi-three-level nature of the active medium Yb:YAG, these lower level ions will then absorb a fraction of the seed light in the thin-disk gain medium, leading to a decrease of the total output energy for high doping levels of the crystal.

3.3.3 Influence of number of passes

To find the influence of the number of passes on the amplification of the laser pulses in the amplifier, the simulation was set up with the optimal 7 at. % doping concentration of the crystal. The pre-pumping time was again chosen such that the output burst shape is flat. The number of passes was chosen between 1 and 30 passes, which is experimentally realized in the setup. Between 1 and 15 passes, the step size in the

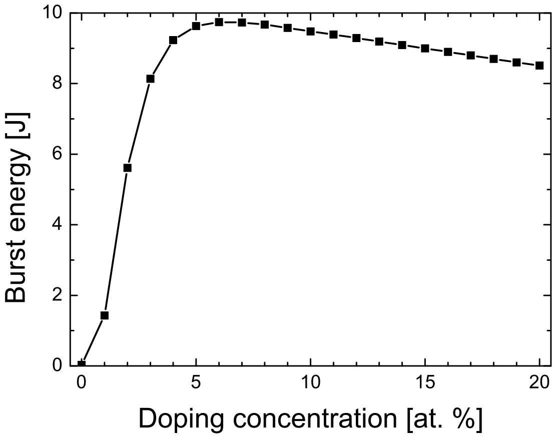

Figure 3.4: Influence of the doping concentration on the maximum achievable output burst energy. For values above 7 at. %, the total output energy starts to decrease due to reabsorption in the active ions.

simulation is 1 pass, for more than 15 passes the step size is increased to 2 because the higher number of passes can only be realized in the setup by retracing the multipass, using every pass in the setup twice (refer to section 4.4 for details on the experimental setup). Figure 3.5 shows the simulation results depending on the number of passes in the amplifier setup.

It can be seen that for a total number of passes on the disk gain medium of around 20, the total output burst energy of the amplifier starts to saturate. The slight increase for even higher number of passes can be explained by the gain saturation described in section 2.3.4, which leads to only slight amplification of the laser pulses for each additional pass on the gain medium. It is important to note that ASE is not included in the model at this point. With the effects of ASE, the amplification per pass will be reduced, as will be shown in the following section.

3.3.4 Gain curve for optimal parameters

With the optimum parameters found for the amplifier, the characteristics of the burst-mode amplification can be simulated without the influence of ASE. This gives an estimate of the highest achievable output burst energy of the amplifier. Therefore, a number of passes of 30 is chosen with a doping concentration of the gain medium of 7 at. % and the right pre-pumping time to achieve a flat burst shape out of the amplifier. The resulting amplifier characteristics are displayed in figure 3.6.

It can be seen that with considerable input parameters for the amplifier, a

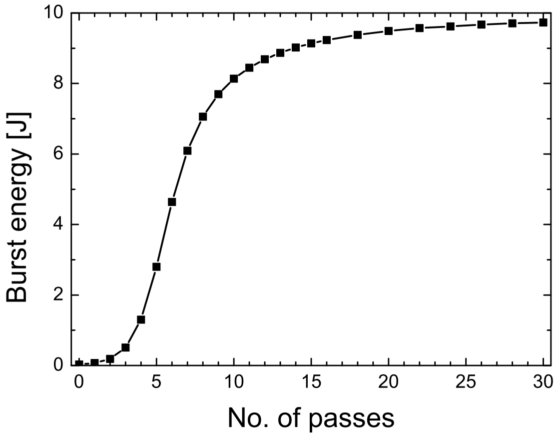

Figure 3.5: Influence of the number of passes on the maximum achievable output burst energy. At a number of around 20 passes on the disk gain medium, the total output energy of the amplifier starts to saturate with only a slight increase to a higher number of passes.

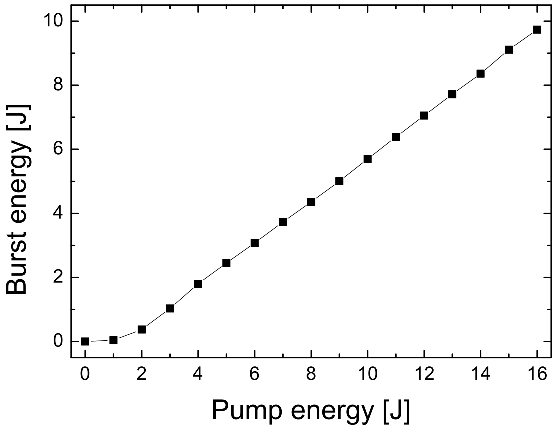

Figure 3.6: Amplifier characteristics for the optimal parameters of the multipass setup. 30 passes are used with an adequate pre-pumping time and a gain medium with 7 at. % doping concentration.

maximum output burst energy around 9.7 J can be achieved. This leads together with the maximum achievable pump energy in the amplifier of 16 J to an optical efficiency of 60 %. The input parameters for the simulation are also the parameters of the disk amplifier medium used in the experimental setup. As already mentioned above, these simulations do not include the influence of ASE on the amplifier characteristics. A survey of the ASE influence will be given in the following.

3.4 Simulations with ASE

As already mentioned at the beginning of the last section, the ASE itself can not be directly measured in the experimental setup. But with the simulation code and experimental results, an estimate of the characteristics can be performed. The free parameter left to model the ASE characteristics is the reflection of the ASE modes at the disk boundaries. Figure 3.7 shows the impact of different reflection coefficients at the disk boundaries.

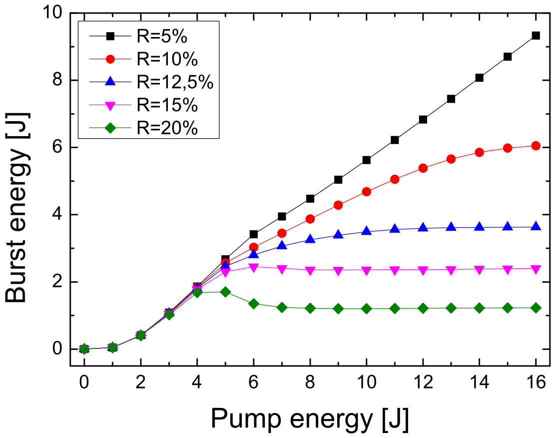

Figure 3.7: Influence of the reflectivity for the amplified spontaneous emission at the disk boundaries on the amplification. The blue line shows the results which best match the experimentally achieved characteristics of the multipass amplifier.

As will be shown in the experimental results chapter (see section 5.4), a good confinement of theoretical predictions and experimental results is achieved at a reflectivity of 12.5 % (the blue line in figure 3.7). For less reflectivity, the ASE modes which develop in the gain medium don't encounter enough amplification to match the losses due to reabsorption in the outer, unpumped regions of the disk and the reflection at the boundaries. For a higher reflection, the ASE is amplified such that there is not enough population inversion left for the amplification of the seed laser pulses. This manifests in a roll-over at a certain pump energy at which the ASE encounters enough amplification to form a stable mode in the amplifier medium. With this parameter fixed, a study is performed to evaluate the influence of the number of passes on the amplifier characteristics with ASE taken into account. For this study, the maximum output burst energy at full pump energy is simulated. The results of this simulation are displayed in figure 3.8.

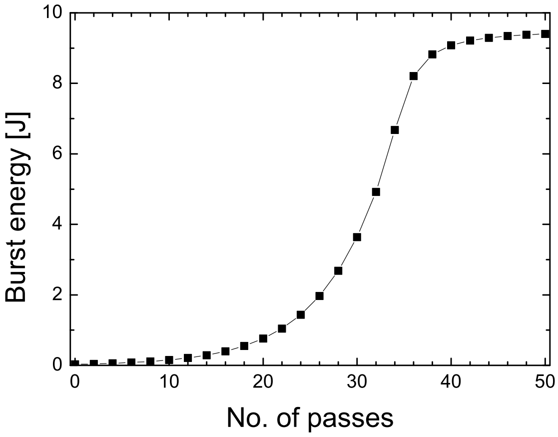

Figure 3.8: Influence of the number of passes on the maximum achievable output burst energy with ASE taken into account (with 12.5 % reflectivity at the disk boundaries). The saturation of the amplifier output is shifted to a reasonable higher number of passes compared to the case where ASE is not taken into account. This is due to the reduced population inversion available for seed pulse amplification by the amplification of ASE modes in the gain medium.

It can be seen that the number of passes on the gain medium where saturation in the amplifier can be achieved is shifted to a reasonable higher number. This is due to the fact that the amplification of the seed pulses reduces the inversion which is available for the amplification of ASE more efficiently for a higher number of passes. Thus, due to reabsorption and reflectivity losses, the ASE gets nearly fully suppressed for a high number of seed passes. Unfortunately, the higher number of passes was not achievable in the experiment due to setup constraints. The available space for additional mirrors and also the stability of the entire multipass setup needed to be considered.

Chapter 4

Experimental setup

In this chapter, the different experimental setups for testing of the pump amplifier system are explained. The Titanium-Sapphire oscillators used in the experiment are described in section 4.1. The entire amplifier system is based on a fiber CPA system with subsequent power amplifiers. The fiber amplifier system is described in section 4.2. For the subsequent amplifier systems, there are two different options, one is an Yb:YAG Innoslab laser amplifier (section 4.3) and the other option is an Yb:YAG thin-disk amplifier, which is described in detail in section 4.4. A temporal diagnostic tool for pump-seed synchronization is set up and tested for using the amplifier systems as pump amplifier for the OPCPA system. This is described in section 4.5.

4.1 Titanium Sapphire Oscillator

The seed source of the pump amplifier systems is a Titanium Sapphire (Ti:Sa) oscillator. The oscillator used for the experiments is a Rainbow from Femtolasers. It has a broadband spectral output ranging from 650 nm to 1000 nm. The same oscillator is used as a seed for a non-collinear optical parametric chirped-pulse amplifier (n-OPCPA) system. A photonic crystal fiber (PCF) was used to attain a spectral shift to 1030 nm. The output power of this PCF solitonic shifter is 800 μW at 108.33 MHz. This is used to seed the subsequent fiber amplifier stages which will be described in detail in the next section.

In later experiments, a new oscillator provided by Venteon Laser Technologies GmbH was used for the seed generation for the fiber amplifier system and as seed for the OPCPA system. A Pulse:One OPCPA seed system with a spectral bandwidth ranging from 620 nm to more than 1100 nm. An output port at 1030 nm is used directly for the seeding of the fiber amplifier system. Accordingly, there is no need of a PCF wavelength shifter which has caused instabilities in timing as well as in output power in the former oscillator setup.

Since the output characteristics of the fiber amplifier system is not dependant on the type of pump seed source used in the individual experiments, it will not be stated which type of oscillator has been used for the individual amplifier setups. The difference in the use of the two types of oscillator is the impact on the OPCPA systems. The different output spectra play a role. In addition to that, the oscillator provided by Venteon has a much higher long term stability compared to the Rainbow oscillator. This also has an impact on the characteristics of the individual systems on the long term stability of the pump amplifier system. The lack of a PCF solitonic shifter in the case of the Venteon oscillator provides a very stable seed beam for the fiber amplifier system for day to day operation as well as for long term measurements with the laser system.

4.2 Fiber amplifier

The fiber amplifier system used for all experiments consists of two pre-amplification fibers, two main fiber rod amplifiers and a stretcher/compressor setup. An overview sketch of the setup is given in figure 4.1.

The seed laser beam originating from the oscillator is coupled into a single-mode, polarization-maintaining fiber with a length of about 100 m to stretch the femtosecond pulses to picosecond pulse durations. These pulses are then coupled into an active Yb-doped fiber amplifier. The repetition rate is subsequently reduced to 2 MHz by an acusto-optic modulator (AOM). The output of the first pre-amplification stage is 5 mW at 2 MHz repetition rate. These pulses are then further stretched to 2.2 ns with an Öffner-type grating stretcher. After stretching, the pulses are coupled into a second pre-amplification system similar to the first one. After this second preamplifier, the repetition rate of the pulses is further reduced by a second AOM. It can be chosen between the full 2 MHz from the first AOM down to several kHz. At 100 kHz repetition rate, the output power of this second pre-amplification system is 2.3 mW.

The output of this preamplifier is then coupled into a large-pitch Yb:glass fiber rod with 40 μm inner core diameter, the first main amplifier. Independent of the repetition rate of the input, the laser beam is amplified to 2 W average output power in this amplifier. Subsequently, a third AOM is used to either further reduce the repetition rate for continuous-mode operation or to form the burst of pulses for the burst-mode operation of the amplifier system. In the latter case, the second AOM defines the intra-burst repetition rate while the third AOM defines the length of the burst and thus the number of pulses in the burst. After this third AOM, a second main amplifier rod with 80 μm inner core diameter follows which is capable of amplifying the seed beam up to 50 W of output power, either in continuous mode or as an intra-burst output power in the burst-mode operation.

For pulse compression after the amplification, a 4-pass Treacy compressor is used. The second grating is the same as the stretcher grating, with an additional

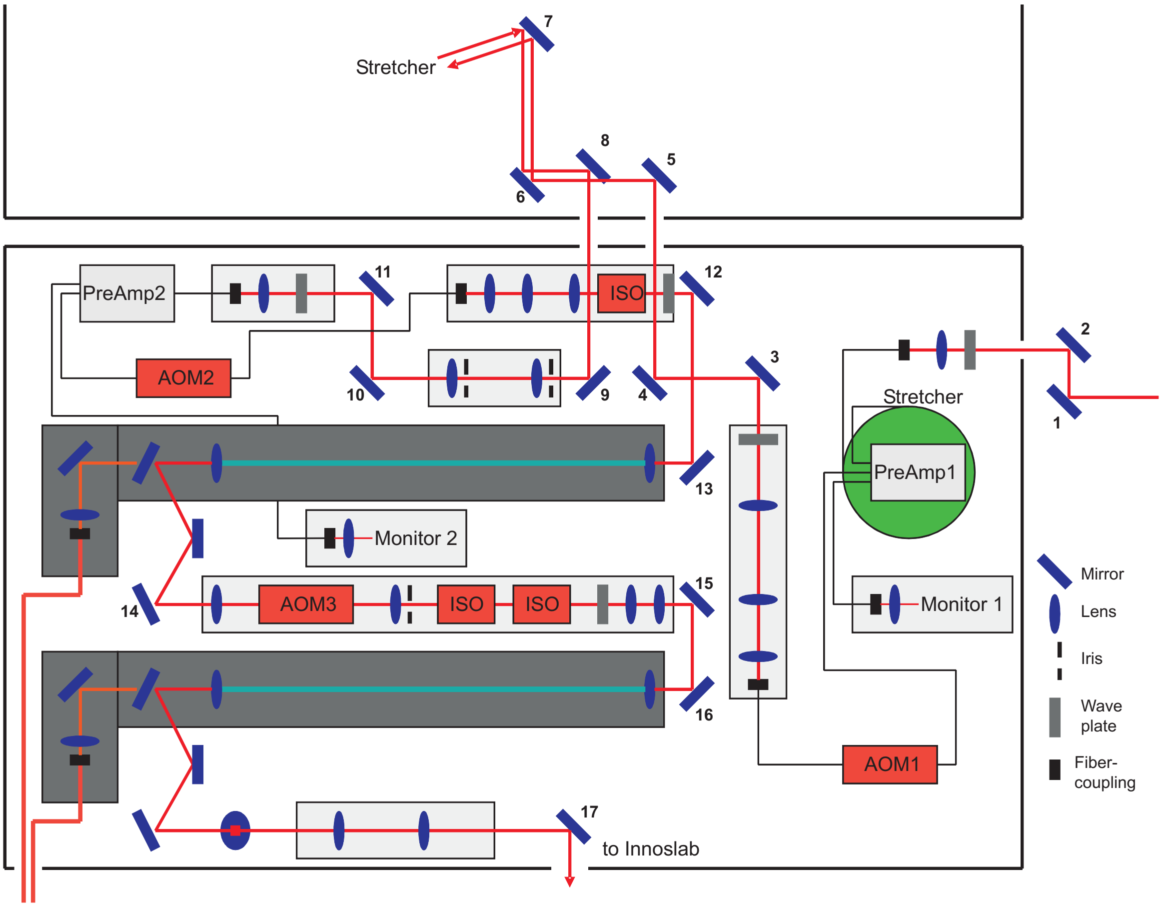

Figure 4.1: Schematic setup of the fiber amplification system. The seed is coupled into the fiber stretcher and the first pre-amplification stage (PreAmp1) by mirrors 1 and 2. In the case of the Venteon oscillator, incoupling is directly achieved by a fiber. The repetition rate is reduced in the first acusto-optic modulator (AOM1). Afterwards, the pulses are stretched to 2 ns in an Öffner-type stretcher (not shown in the schematic). A second pre-amplification stage and further reduction of the repetition rate follow. In the grey shaded area, the two main amplification stages are shown. The first one is a PCF-rod with 40 μm core diameter and the second one is a PCF-rod with 80 μm core diameter. Between the two main amplifiers, the repetition rate can be further reduced or the burst can be generated by AOM3. ISO: Optical isolator.

small grating to form a grating pair. This grating compressor is also used for the compression of the pulses from the Innoslab and thin-disk amplifiers. The gratings used are dielectric multilayer gratings which provide a total compressor transmission of approximately 80 %.

4.3 Yb:YAG Innoslab amplifier

The Innoslab laser technology has already been described in section 2.3.6, but will be explained in more detail here. The central part of the Innoslab amplifier is a slab shaped crystal with the dimensions of 10x10x1 mm^3. The laser medium is pumped by laser diodes with an emission wavelength of 941 nm. The diode light is focused to a line onto the front plane of the crystal. This leads in combination with the heat removal perpendicular to the pump beam to a thermal lens which is also perpendicular to the pump beam. The seed beam is then coupled into the crystal collinear with the pump beam and then folded several times through the gain medium. In one direction, the mode of the beam is directly reproduced by the thermal lens while in the other direction, the beam size is increased for every pass by a confocal arrangement of curved mirrors. Thus, the intensity of the amplified beam stays the same for every pass in the gain medium keeping the efficiency of the laser operation constant and avoiding optical damage to the components. Although passing several times through the gain medium, the Innoslab amplifier can be considered as a single pass amplifier since for every pass a new section of the gain medium is used. A schematic of the Innoslab technique is shown in figure 4.2.

In the case of experiments, three different types of Innoslab amplifiers were tested. The mechanical properties stated above are the same for all three devices, the difference is the number of passes used in the amplifier crystal and in the total output power of the pumping diodes. The first amplifier used is a 250 W output power amplifier. The pump radiation is provided by four diode stacks with a total output power of 600 W. This output is collimated and focused as a line in the amplification medium. On the seed side, 9 passes are used in the amplification medium, leading to a total output power of 250 W. The results with this type of amplifier will be presented in section 5.1.1.

The second type of Innoslab amplifier used in this thesis is specified to have 500 W output power. In principle, it relies on the same setup as the 250 W amplifier stated above. The pump is generated by eight diode stacks with a total output power of around 1.1 kW. Again 9 passes in the amplification medium are used to amplify the pulses, leading to a total amplification to 500 W output power. The results with the 500 W Innoslab amplifier are presented in section 5.1.2. This amplifier will be used both for the amplification of pump pulses for the OPCPA system and for seeding the thin-disk amplifier (see section 5.3).

To further increase the output energy of the Innoslab amplifiers, a 1.5 kW booster amplifier based on the Innoslab technology is implemented in the setup. It consists of two amplification stages as stated for the 500 W amplifier. The pump of each

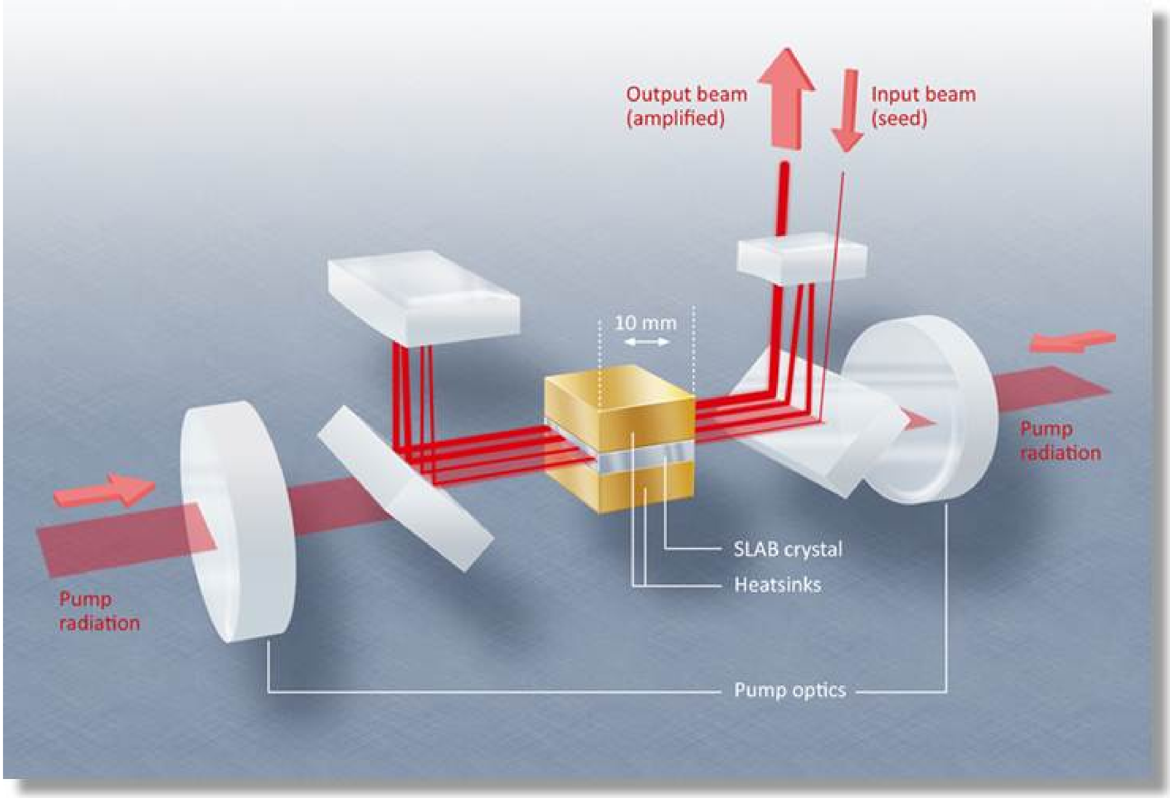

Figure 4.2: Schematic of the Innoslab technology [picture provided by Amphos GmbH]. The input seed beam is folded several times through the amplification medium by folding mirrors and curved end mirrors. There, for every pass, a new section of the amplification medium is used. The curved mirrors expand the beam for every pass to maintain a constant intensity of the amplified beam in the gain medium. The pump is coupled into the slab crystal through one of the folding mirrors.

individual stage is similar to the pump setup in the 500 W amplifier stage. The difference of this booster amplifier stages lies in the coupling of the seed beam to the amplification medium. It is coupled in as a strongly elliptic beam, fitting to the aperture of the gain medium. Thus, only a single pass in the gain medium is used, which is sufficient for the full power extraction of the laser crystal. Each stage amplifies the seed beam by a factor of 2 and 1.5, respectively, adding 500 W of output power to the seed beam. Thus, an output of 1.5 kW is achieved. This amplifier stage can either be used as pump amplifier for the OPCPA system (section 5.1.3) or for seed generation of the thin-disk amplifier (section 5.5).

Innoslab laser amplifiers are commercial laser systems provided by Amphos

GmbH, no further details can be given on the pump source, pump and beam optics used in the setup.

4.4 Yb:YAG thin-disk multipass amplifier

The setup of the thin-disk amplifier consists of a pump laser head commercially available at Trumpf Laser GmbH and a home-made multipass setup. The pump source consists of six stacks of laser diodes which are collimated and homogenized. The pump radiation is then folded on the thin-disk gain medium by a parabolic mirror and retro-reflecting prism mirrors. 24 pump passes on the gain medium are realized. The pump beam path in the laser head is shown in figure 2.11. The pump diodes have an emission wavelength of 940 nm. The total nominal pump power of the diodes is 10 kW, but in the burst operation mode they can be operated with a higher voltage leading to 12.4 kW total pump power during the 1.3 ms pump pulse (rectangular temporal shape). The gain medium of the thin-disk amplifier is an Yb:YAG disk with a diameter of 17 mm and a thickness of 360 μm. The radius of curvature of the gain medium is 20 m, which leads to a focal length of the amplifier module of 10 m. It is mounted on a heat sink providing heat removal through the back plane of the disk. Thus, the influence of thermal lensing due to high power pumping of the gain medium is kept low.

The seed multipass is formed by two planes of mirrors. Figure 4.3a shows a schematic of the setup. The plane with the back-reflecting mirrors is formed by an array of up to 30 plane mirrors. Part of these direct the beam onto the thin-disk gain medium and the other part directs the beam to the array of folding mirrors. The latter one consists partly of defocusing mirrors to counteract the focusing effect of the curved disk. The radius of curvature of these mirrors is 8 m. The folding mirror array is projecting the beam to a new beam path after each pass on the disk form a multipass arrangement. The entire setup is composed such that the angles between the beams are kept small. This is necessary to avoid losses in the reflectivity of the multipass mirrors. Thus, the number of passes is restricted by the distance between the mirror array and the thin-disk gain medium. This distance is in turn critical concerning the stability of the whole amplifier system. Longer distances introduce strong pointing and temporal fluctuations caused by air flow and temperature changes. Figure 4.3b and 4.3c show the order in which the beam passes the individual mirrors of the array of back-reflecting mirrors and the mirror array, respectively.

Starting at mirror 1 on the mirror array, the beam is directed to the disk module and arrives on mirror 2. It is then folded to mirror 1 on the back reflecting mirror array, which then folds the beam to mirror 3 on the mirror array. The second pass on the disk is realized by using mirror 3 and 4. The beam is folded 15 times on the disk module where the rectangular mirrors on the back reflecting array indicate periscope

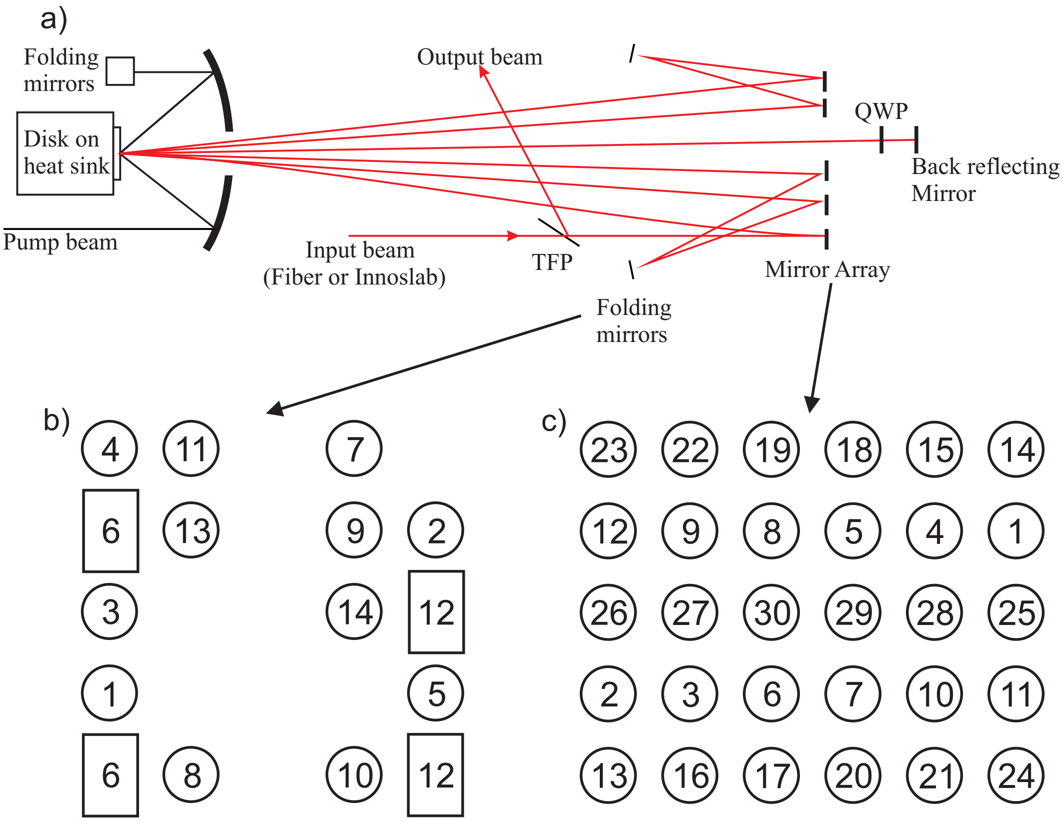

Figure 4.3: Schematic of the multipass setup for the thin-disk amplifier. a) Schematic of the entire setup. The seed beam originating from either the fiber or the Innoslab laser is coupled into the multipass in transmission through a thin-film polarizer (TFP). The beam is then folded up to 15 times on the thin disk gain medium. After the 15 passes, the polarization of the seed beam is rotated by 90° by a double pass through a quarter-wave plate (QWP) and retraced through the multipass setup. Thus, 30 passes on the gain medium are achieved. b) Arrangement of the mirrors in the folding mirror array with the sequence of passes on the individual mirrors. c) Arrangement of the mirrors in the mirror array with the sequence of the passes on the individual mirrors. With retracing, the mirrors are passed a second time in descending order. Outcoupling of the retraced beam is attained by reflection from the TFP.

mirrors to move the beam to a new level on the mirror array. To achieve a higher number of passes on the thin-disk gain medium, there is the possibility to retrace the whole multipass setup. Therefore, mirror 30 on the multipass array is equipped with a quarter-wave plate which rotates the polarization of the seed laser pulses by 90 degree. The number of passes is doubled. The output beam is then coupled out of the multipass array by a thin-film polarizer which transmits the input and reflects the output of the amplifier.

4.5 Pump-seed synchronization for OPCPA

For the synchronization of pump and broadband seed pulses in the OPCPA system, a measurement of temporal drift and jitter is necessary. A balanced cross correlator is used to find the temporal overlap of both pump and seed pulses [133, 134]. This technique relies on sum frequency generation (SFG) in a nonlinear crystal provided that both pump and seed pulse are temporally and spatially overlapped in the medium. After a first pass through the nonlinear medium, the fundamental beams are separated from the generated sum frequency which is detected by a photomultiplier. The fundamental pulses are delayed with respect to each other by a dispersive medium (for example a glass plate) and sent back through the nonlinear medium, generating a second signal of SFG. A schematic of the working principle of balanced cross correlation is given in figure 4.4.

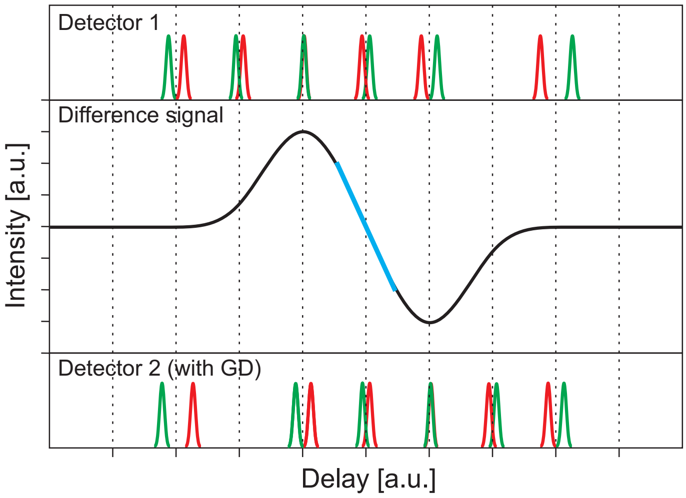

Figure 4.4: Schematic of the working principle of balanced cross correlation. Depending on the delay of the reference (green) and signal (red) pulse, the overlap for sum frequency generation for the different detectors varies. This leads to the characteristic difference signal. The working region of the balanced cross correlator is depicted by a blue line in the difference signal.

There are two possible ways to set up the balanced cross correlator. One way is to use the same nonlinear crystal for both passes of the fundamental beam (single crystal balanced cross-correlator). The second way is realized by using a beamsplitter for the fundamental beams and two nonlinear crystals (two crystal balanced cross-correlator). A schematic of the first type of setup mentioned is given in figure 4.5[1], where two input signals with 800 nm as slave signal and 1550 nm as reference signal with a sum frequency wavelength of 528 nm are measured with the balanced cross correlator.

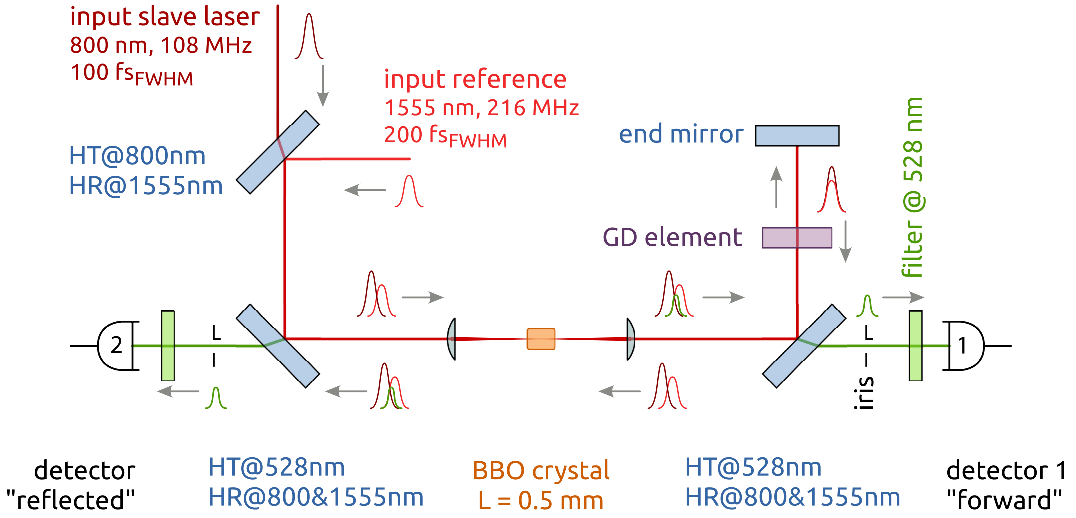

Figure 4.5: Schematic of a single crystal balanced cross-correlator [courtesy of Sebastian Schulz]. The input and reference signals are spatially combined in a dichroic mirror and focussed into a BBO crystal, generating the sum frequency of both signals. The sum frequency signal is separated from the input signals in a dichroic mirror and detected by the forward detector. The input signals then undergo a group delay shift in a glass plate and refocussed into the BBO crystal, generating a second sum frequency signal which is detected by the ”reflected” detector.

This type of setup has been implemented and tested with the fiber amplifier and the oscillator output in our laser setup. The seed signal of the oscillator was filtered with a bandpass filter with a central wavelength of 700 nm and overlapped with the pump pulses at a wavelength of 1030 nm. The corresponding sum frequency wavelength is 417 nm. During the measurements, problems arised with back reflection of the generated signal of the first pass in the BBO in the detector of the second pass, which tremendously influenced the detected signal. To circumvent this type of problem, the two crystal balanced cross correlator is used. It is set up in a F-shaped configuration where in each arm both beams are focused in a type-I BBO crystal. The SFG-signals are filtered with a bandpass filter with a transmission wavelength of

---

[1] courtesy of Sebastian Schulz: seb.schulz@desy.de

(400±20) nm and recorded by photomultipliers of type H6780 from Hamamatsu. A schematic of the setup can be found in figure 4.6.

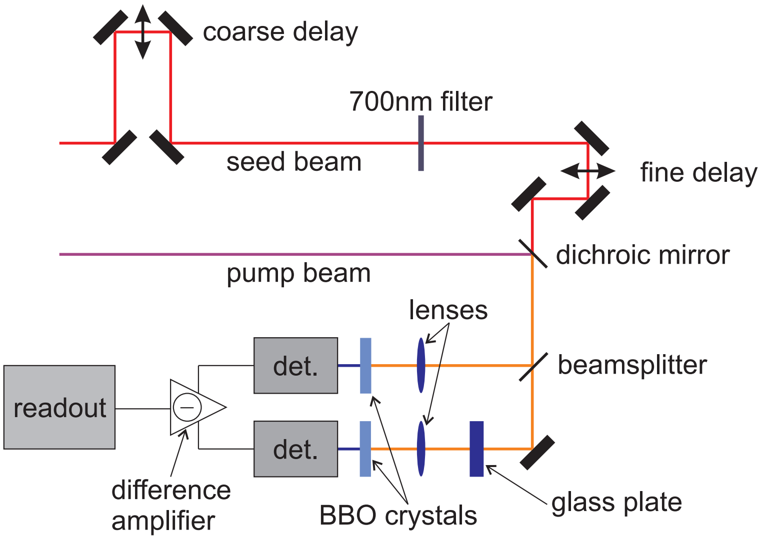

Figure 4.6: Schematic of a two-crystal balanced cross-correlator in F-shape configuration. The input pump and seed signals are spatially combined in a dichroic mirror. After splitting the signals in two branches by a 50/50 beamsplitter, each branch is focused individually into a BBO crystal for sum frequency generation. One of the two branches is equipped with a glass plate for group delay generation of the two input pulses. The two detected signals are amplified in a difference amplifier to provide the balanced detection signal in the readout.

The readout of the two detectors is achieved by a difference amplifier of type DLPVA-100-B-D from FEMTO GmbH. This device provides the difference voltage of the two input signals. If the photomultipliers are well balanced, a direction sensitive output of the balanced cross correlator signal can be achieved. This signal can then be used to operate a delay stage which is situated in the pump beam path to keep a constant timing between the two individual pulses. Thus, the long term stability of the entire OPCPA setup can be tremendously improved since temporal drifts caused by temperature fluctuations are fully compensated.

Chapter 5

Experimental results

The results achieved with the different amplifier schemes are presented and discussed in this chapter. The results with Innoslab amplifier will be presented in section 5.1, where a 250 W system, a 500 W system and a 1.5 kW system have been tested. The results of the investigations on the fiber seeded thin-disk amplifier will be presented in section 5.2. A combination of the thin-disk laser with an Innoslab amplifier as additional seed preamplifier will be presented in section 5.3, where the 500 W Innoslab amplifier has been used as a seeder for the thin-disk amplifier with a reduced number of passes. Consecutively, a comparison of the results of the different thin-disk amplifier experiments with the simulation code presented in chapter 3 is presented in section 5.4, where the influence of the amplified spontaneous emission (ASE) can be modeled by varying the ASE parameters in the code to reach an overlap of the simulated results with the experimental results. Additionally, an investigation on the use of the thin-disk amplifier to reach higher output energies with a stronger seeder and a cascade of two thin-disk amplifiers will be presented. To investigate the capabilities of thin-disk amplifiers in a cascaded setup, experiments have been performed with a 1.5 kW Innoslab seeder, where the experimental results are presented in section 5.5. At the end of the chapter, the measurement results for the pump-seed synchronization for the OPCPA system are presented in section 5.6. These were achieved using the fiber amplifier for the pump pulses and the oscillator output for the seed pulses for the OPCPA.

5.1 Innoslab amplifier

In this section, the results obtained with Yb:YAG Innoslab technology are presented. Starting with a first test of the technology with a 250 W amplifier, the capabilities of this concept are proved (section 5.1.1). The next step was to implement a 500 W Innoslab amplifier (section 5.1.2), which was tested as a stand alone system and later used as a seed amplifier for a thin-disk amplifier (see section 5.3). At last, an Innoslab booster amplifier was installed to increase the pulse energy to the required parameter values of 20 mJ per pulse at 100 kHz repetition rate. The results for this system are presented in section 5.1.3.

5.1.1 250 W amplifier system

The first Innoslab amplifier tested was an amplifier delivering 250 W of output power. The amplifier was operated in a continuous operation mode at different repetition rates. The pulse energy of the output pulses is defined by the output power and the repetition rate of the amplifier to 20 mJ at 12.5 kHz or 2.5 mJ at 100 kHz. These two individual operation points are important, as a pulse energy of 20 mJ is specified for the OPCPA system and the amplifier needs to be capable of amplifying pulses at 100 kHz repetition rate. The pulses were then compressed in a grating compressor. The resulting autocorrelation trace measured with a single-shot autocorrelator is displayed together with a beam profile of the output beam and the seed and output spectrum in figure 5.1. The spectra were taken with a Shamrock spectrometer with a 500 lines per mm grating and a Andor iDus camera. The measured spectra and autocorrelations throughout this work were averaged over the entire burst with 80 pulses at 100 kHz repetition rate.

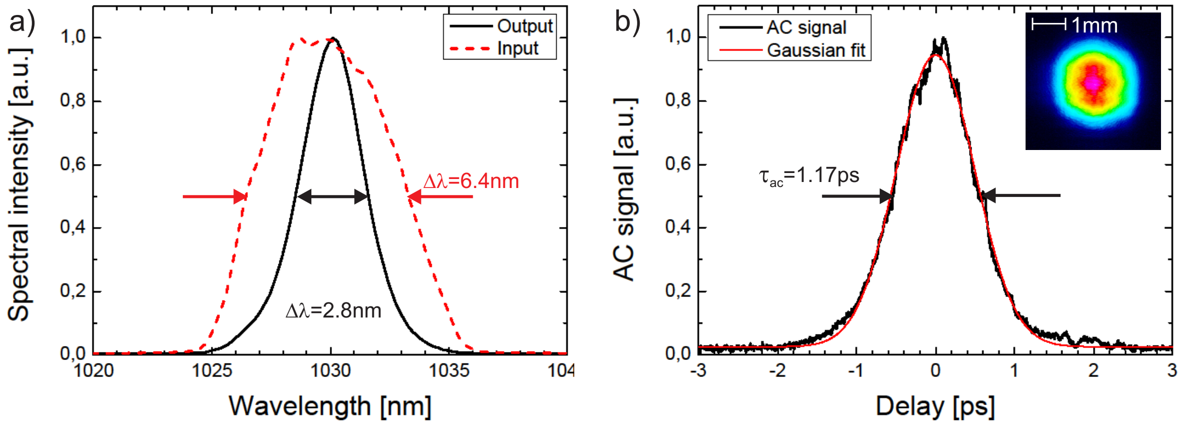

Figure 5.1: Compression of the 250 W Innoslab output. a) Output spectrum of the amplified seed, b) autocorrelation trace and Gaussian fit of the compressed pulses. The inset in b) shows the beam profile of the Innoslab output.

The spectrum of the fiber laser seeder is gain narrowed to 2.8 nm. The Fourier-transform-limited pulse duration would be 599.6 fs. The measured pulse duration at the compressor output is 830 fs assuming a Gaussian pulse shape (1.17 ps autocorrelation width). The test of this amplifier system produced promising results for the implementation of the Innoslab amplifier technology in the OPCPA pump amplifier chain. The results for the final Innoslab amplifiers will be explained in the following sections.

5.1.2 500 W amplifier system

The 500 W Innoslab amplifier system has been tested in burst operation mode with two different intra-burst repetition rates. The first one was 27.5 kHz to use the amplifier system as pump amplifier with high pulse energy for the OPCPA system. The second repetition rate was 100 kHz in order to seed a subsequent thin-disk booster amplifier. The output burst shapes of both operation modes are displayed in figure 5.2. It is acquired with a photodiode of type DET10-A from Thorlabs and recorded with a Tektronix scope (DPO7254). This measurement setup for the burst profiles is used for all measurements of this kind throughout the entire thesis. There, it has to be noted that sampling problems with the scope lead to small oscillations on top of the burst traces.

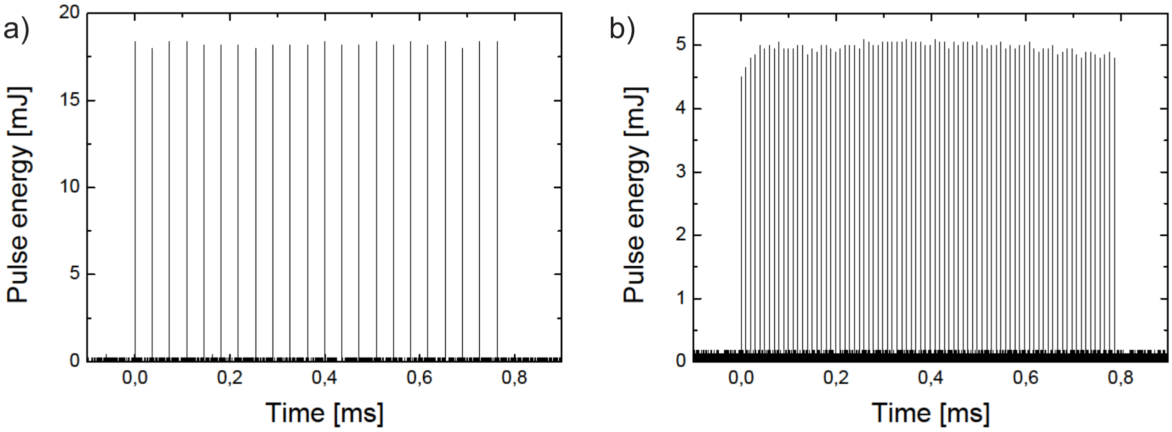

Figure 5.2: Burst shapes of the 500 W Innoslab amplifier. a) 27.5 kHz repetition rate and b) 100 kHz repetition rate. The pulse to pulse energy stabilities are 0.8 % rms for the 27.5 kHz and 1.7 % rms for the 100 kHz case.

The burst presented in figure 5.2a is taken with pulses at 27.5 kHz repetition rate. The burst length is 800 μs with to 22 pulses in the burst. The overall burst energy is 400 mJ, or a pulse energy of 18.2 mJ. This pulse energy can be used for pumping the OPCPA system. The pulse to pulse energy stability within the burst is 0.8 % rms. The desired stability would be 1 %, which is fulfilled in the case of the 27.5 kHz operation. For the case presented in figure 5.2b, the repetition rate is 100 kHz with 80 pulses in the burst. The corresponding single pulse energy is 5 mJ. The pulse to pulse energy stability in this case is 1.7 % rms. This amplifier output has been used for seeding the thin-disk amplifier as will be described in more detail in section 5.3. The pulses at 27.5 kHz repetition rate have been compressed in the grating compressor to be used as pump amplifier for the OPCPA system. The resulting autocorrelation trace is given in figure 5.3.

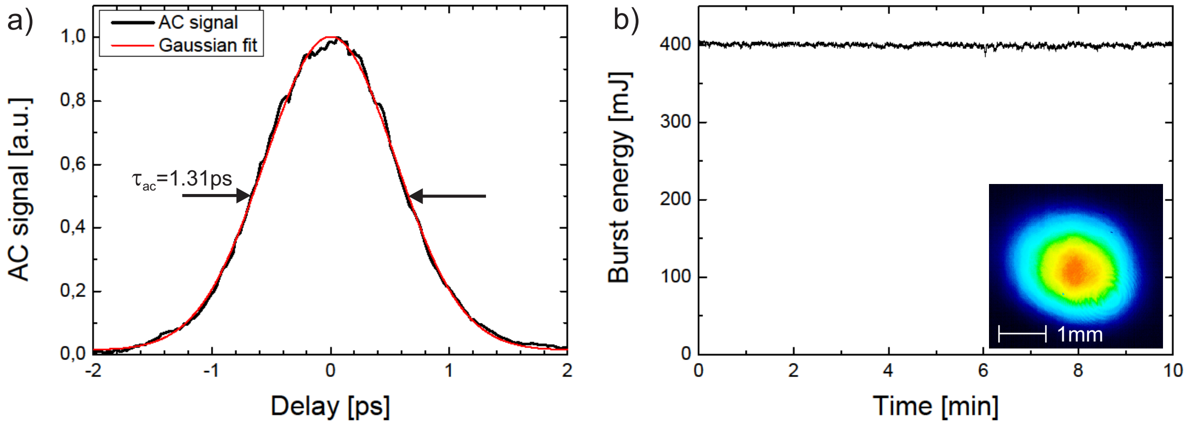

Figure 5.3: a) Autocorrelation measurement and Gaussian fit of the output pulses of the 500 W Innoslab amplifier operated at 27.5 kHz repetition rate. b) Stability measurement of the Innoslab output. The inset shows the output beam profile after compression.

The pulse duration measurement was performed with a PulseCheck 50 autocorrelator from APE GmbH. The measured autocorrelation width of the compressed pulses is 1.31 ps, or a compressed pulse duration of 929 fs. In addition to the pulse duration measurements, the output stability of the amplifier has been measured. The total burst energy stability of the amplifier output is 0.5 % rms at a burst energy of 400 mJ (see figure 5.3b).

5.1.3 1.5 kW booster amplifier system

To further increase the amplified pulse energy from the 500 W Innoslab amplifier, a two-stage Innoslab booster amplifier has been installed and tested. The nominal output power of this system is specified to 1.5 kW in continuous operation. The amplifier has first been tested in continuous operation mode. The resulting output power characteristics of all three amplifier stages can be found in figure 5.4.

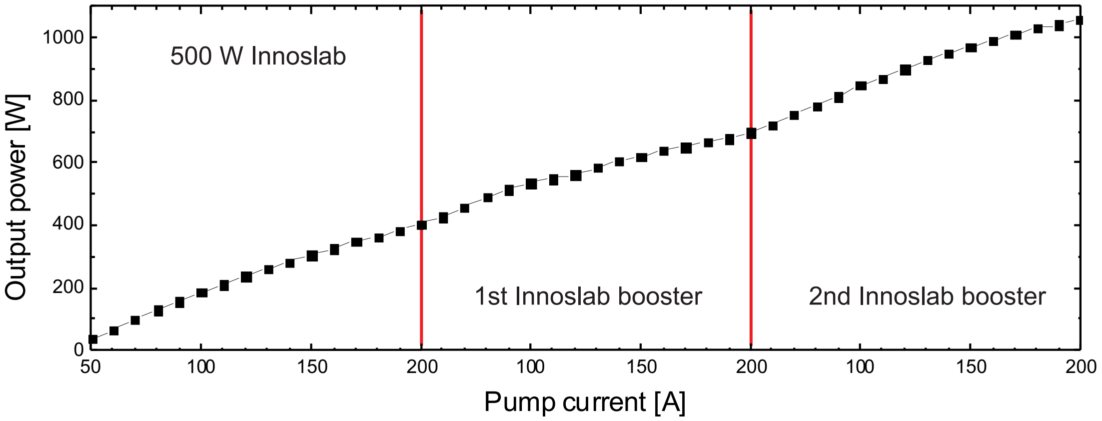

Figure 5.4: Energetics of all three Innoslab amplifier stages. The plot is divided into the first 500 W stage and the two subsequent booster amplifiers.

It can be seen that the maximum output power of the amplifier does not reach the specified 1.5 kW. This is due to a non optimal mode-matching of the amplifier chain. The amplifier was set up for the burst-mode operation, where a different thermal management of the individual amplifier stages has to be taken into account. Due to that fact, a misalignment in the first Innoslab amplifier with 500 W output power can not be avoided in the continuous operation mode. This leads to a distorted beam profile which cannot be amplified to the specified 1.5 kW in the subsequent Innoslab booster amplifiers. The total output power of all three Innoslab amplifier stages was measured to 1.06 kW. After the test of the Innoslab booster in continuous mode, the seeder of the amplifier was switched to the burst-mode operation for testing. The resulting shape of the burst can be found in figure 5.5.

The maximum output power which could be achieved with the amplifier in the burst operation mode is 1.75 kW in the burst. This is tremendously higher than for the continuous mode operation which is explained by the fact that the mode-matching in the amplifier is conceived for burst-mode operation. Additionally, due to the burst-mode operation of the amplifier, pump energy is stored in the active medium prior to seeding which leads to a higher possible amplification of the seed pulses compared to the case of continuous operation. The pulse to pulse energy stability measured for this burst is 2.1 % rms, which is mostly due to the decrease of pulse energy within the burst.

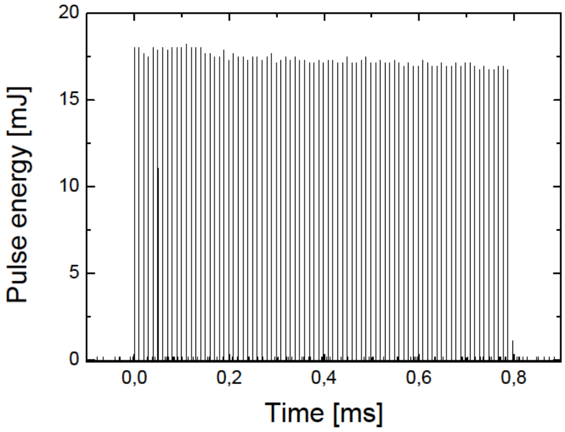

Figure 5.5: Burst profile of the three-stage Innoslab output. The pulse to pulse energy stability is measured to 2.1 % rms.

5.2 Thin-disk amplifier

This section summarizes the thin-disk amplifier results with the fiber amplifier system (section 4.2) as seed source. The focusing properties of the disk module are presented in section 5.2.1 and compared to the theoretical value resulting from the radius of curvature (20 m) of the disk (section 4.4). Followed by that, the results for the amplification of the beam are presented with the different approaches to reduce the effects of amplified spontaneous emission (ASE) stated in section 3.2. The amplification with a large pump spot is given in section 5.2.2. The reduction of ASE influence is then given by reducing the pump spot size (section 5.2.3) and beveling the boundaries of the gain medium (section 5.2.4).

5.2.1 Focus properties of the disk module

Prior to setting up the multipass amplifier system, the focusing properties of the thin-disk module have been measured. For this, a collimated alignment laser at an emission wavelength of 1030 nm (type MIL-F-1030 from CNI Lasers) was reflected from the thin-disk module and the propagation of the beam was measured with a WinCam-D at several distances from the disk module. The results show that the focus length of 10 m (radius of curvature of the disk of 20 m, see section 4.4) is in contradiction with the experiment. Figure 5.6 shows the measured beam diameters depending on the distance from the disk module. These results lead to the assumption that the stated radius of curvature is larger than the real one. The focal length of 6 m, together with the bending effect of the cooling system, leads to an assumed radius of curvature of the disk of 10 m.

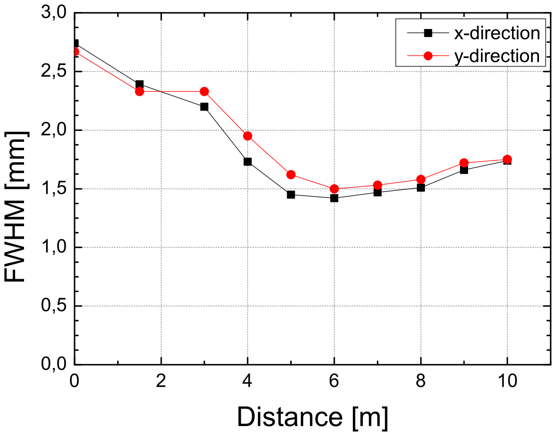

Figure 5.6: Focus properties of the thin disk module depending on the distance from the disk. The measurement shows that the beam starts to diverge after a propagation distance of around 6 m.

The entire multipass was planned with an assumed radius of curvature of 20 m of the disk. After calculations with beam propagation matrices (see section 2.1), defocusing mirrors with a focal length of - 8 m were to be implemented in order to collimate the beam after every second pass on the disk. With the measured focal length, this was not possible to achieve. In order to circumvent too strong divergences of the beam in the multipass, not every second mirror in the back reflecting array could be defocusing. An empiric solution was found to keep the beam sizes on the disk at reasonable values. The resulting plan of the back reflecting array and the propagation of the beam sizes depending on the number of passes on the disk can be found in figure 5.7.

The curved mirrors are marked with a *c*. The beam size is kept between 1 and 3 mm at full width at half maximum (FWHM) on the disk. According to simulations performed with the analytical model presented in chapter 3, the single pass gain is not too much influenced by the beam size. Between the minimum and the maximum value of the beam diameter, a deviation between the corresponding values of the single pass gain is smaller than 8 %. Increasing the total number of passes to 30 is achieved by introducing a telescope to manipulate the divergence of the retraced beam.

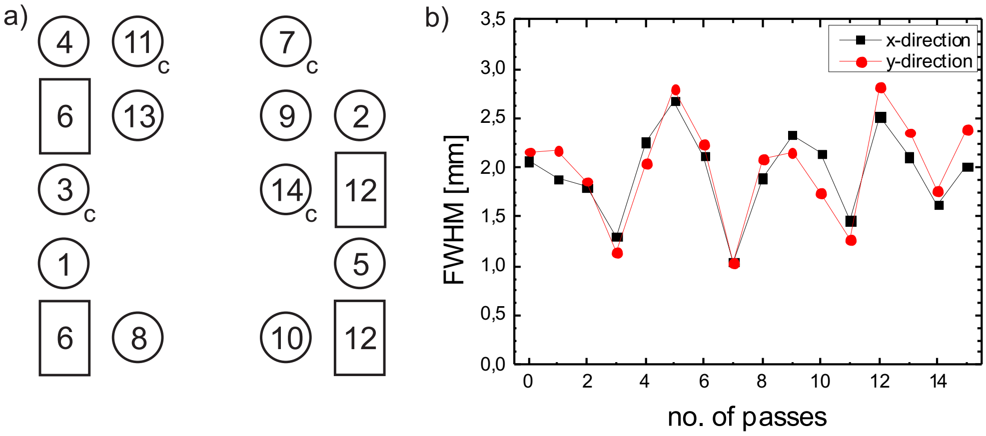

Figure 5.7: a) Position of defocusing mirrors for the 30 pass thin-disk amplifier. Curved mirrors are marked with a *c*. b) Resulting propagation of the seed beam sizes through the first 15 passes on the disk module.

5.2.2 Non-beveled disk, 9.6 mm pump

First tests of the thin-disk amplifier were performed with a pump spot diameter of 9.6 mm on a non-beveled disk. The profile of the pump beam can be found in figure 5.8. For estimating the size of the pump spot, the disk was taken as reference (diameter of 17 mm). The size of the pump spot is then measured by comparing the FWHM of the pump spot with the disk diameter. The measurement was performed at the full pumping power of the thin-disk laser.

The profile of the pump beam shows to be a Supergaussian with a FWHM diameter of 9.63 mm. After taking the profile of the pump beam, a measurement of the total output energy was performed. An energy meter, Ophir Vega with PE50BB-DIF measurement head, was used to measure the maximum output energy of the pump diodes.

The maximum output energy was 16.11 J. With a total pump pulse length of 1.3 ms for the burst mode operation, this results in a maximum output power of 12.4 kW during the pump pulse. The intensity I_{pump} of the pump profile can be calculated:

$$I_{pump} = \frac{P_{pump}}{A_{pump}} = \frac{4 \cdot P_{pump}}{\pi \cdot d_{pump}^2}. \tag{5.1}$$

With a pump power of 12.4 kW and the beam diameter of the pump of 9.63 mm, the resulting pump intensity on the disk calculates to 17 kW/cm^2. The first results with this amplifier setup are shown together with the results of the simulation (see chapter 3) in figure 5.9.

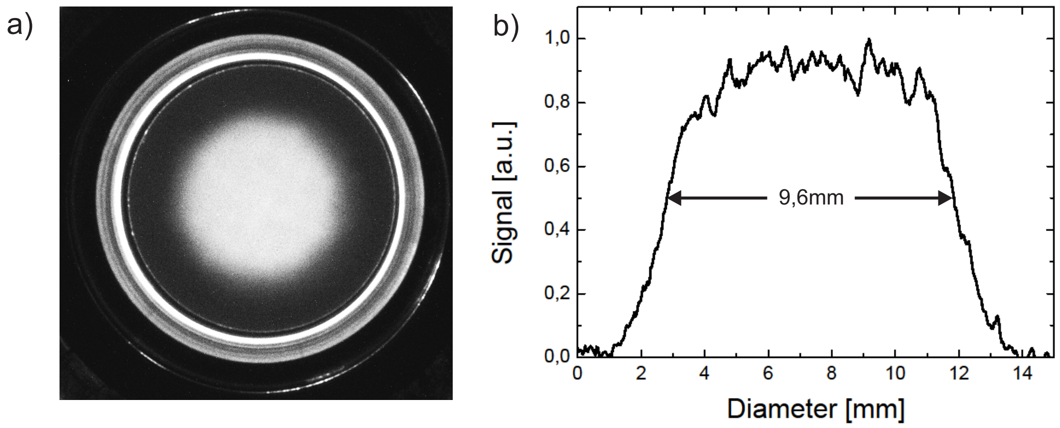

Figure 5.8: Pump profile (a) and line-out (b) of the pump spot on the disk.

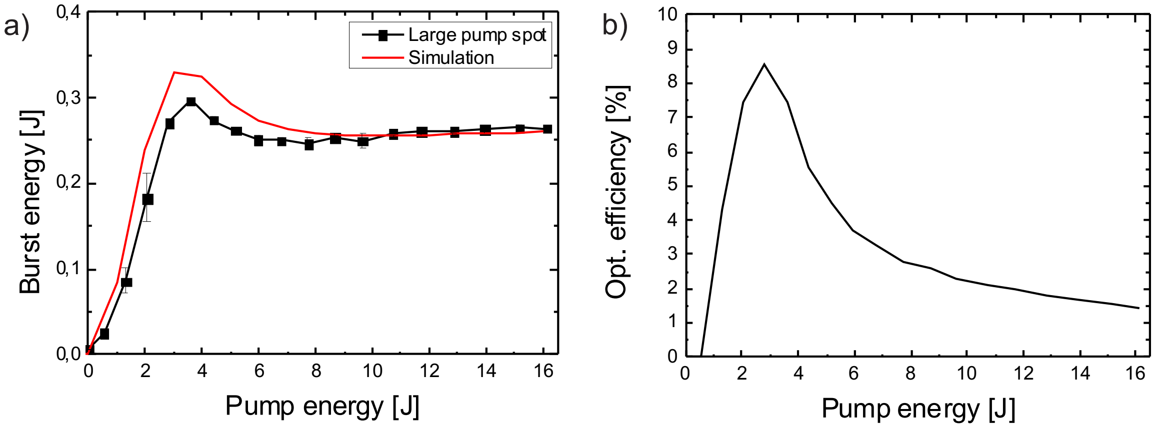

Figure 5.9: Results of thin-disk amplifier with 9.63 mm pump spot and a non-bevelled disk. a) Amplifier characteristics of the output energy depending on the pump energy (black) and simulation results of the amplifier characteristics (red). b) Optical conversion efficiency from pump to seed.

It can be seen from figure 5.9a that already at a pump energy of around 3 J the output of the amplifier reaches a saturation. This shows that the effect of the ASE sets in at low pump energies. The simulated reflection of the ASE at the disk boundaries is

28 %. The maximum output energy in this configuration is 300 mJ, which corresponds to a pulse energy of 3.75 mJ in the burst. With a given seed energy of 375 μJ of the fiber laser amplifier, this corresponds to an amplification factor of 10. With 30 passes in the amplifier, the single pass gain on the thin-disk is 1.08. The optical conversion efficiency η_{opt} is calculated as follows:

$$\eta_{opt} = \frac{E_{out} - E_{in}}{E_{pump}}. \tag{5.2}$$

E_{in}, E_{out} and E_{pump} are the input, output and pump energy. It can be seen from figure 5.9b that the maximum attainable conversion efficiency is 8.5 %. After finding the optimal pump energy for the amplifier, the properties of the setup were characterized. This includes the output energy stability, burst and beam profiles and compression of the output pulses. A stability measurement of the amplifier was performed for a time duration of 90 minutes. The mean value of the output burst energy is 300 mJ with a peak to peak fluctuation of 95 mJ and a standard deviation of 6 mJ, which corresponds to a rms-stability of 2 %. The comparably high value of peak to peak fluctuations has its origin in beam pointing fluctuations caused by air flow in the experimental setup. Figure 5.10 shows the output burst profile of the amplified beam and a spatial beam profile.

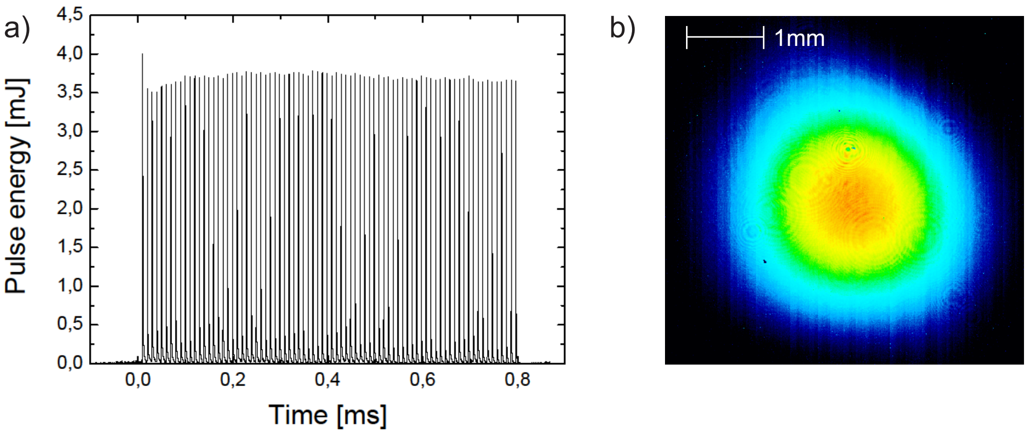

Figure 5.10: a) Burst profile of the amplified output. The pulse to pulse energy stability is 1.5 % rms. b) Beam profile after 30 passes on the thin-disk amplifier.

It can be seen that there are some structures on the burst profile. The higher pulse energy at the beginning of the burst is due to the pre-pumping phase, where a higher inversion is present in the amplification medium. The arising higher amplification of the first pulse depletes the available inversion for the later pulses, which manifests as a dip in the burst profile. After this phase, the amplification reaches an equilibrium, where the individual pulses encounter nearly the same amplification. Due to the ASE, there is still a slight decrease of the pulse energy during the burst. Nevertheless, the pulse to pulse energy stability derived from this measurement is 1.5 % rms. The output of the amplifier has a high quality Gaussian beam profile, as can be seen in figure 5.10b. Since the output of the amplifier is directly used for second-harmonic generation without focussing of the beam, this profile is promising for efficient second-harmonic generation.

The input and output spectrum of the amplifier are displayed in figure 5.11a. It can be seen that the spectrum encounters gain narrowing during the amplification. The FWHM bandwidth of 6.4 nm from the fiber laser seeder is narrowed to 2.8 nm after the thin-disk amplifier. This is in accordance to the gain narrowing of the Innoslab amplifiers.

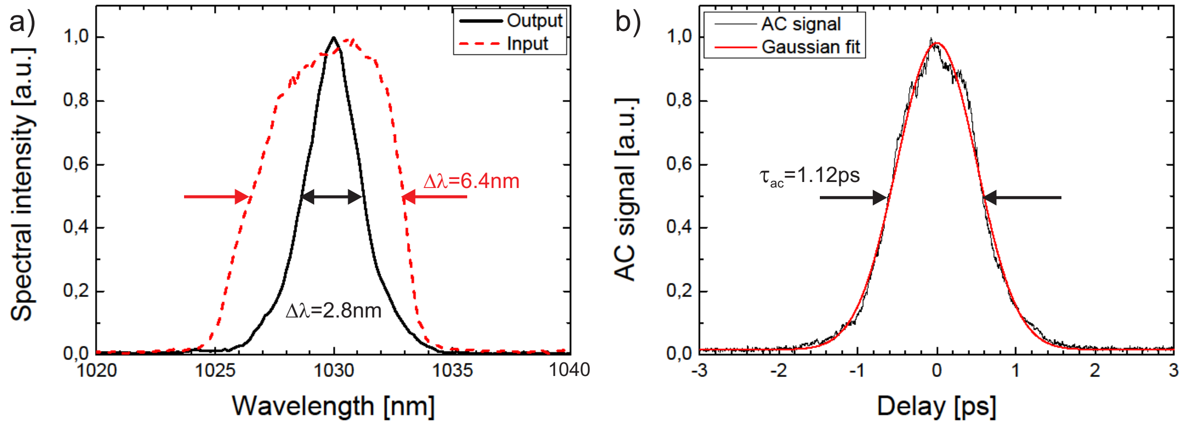

Figure 5.11: a) Spectra of the input (red) and output (black) beams of the thin-disk amplifier. b) Autocorrelation trace and corresponding Gaussian fit of the compressed pulses.

The output of the thin-disk amplifier was then aligned through the grating compressor of the fiber amplifier for compression to sub-ps pulse durations. The resulting autocorrelation trace is shown in figure 5.11b. The measured FWHM width of the autocorrelation is 1.15 ps. For a Gaussian pulse, this results in a pulse duration of 794.8 fs. Compared to the fourier limit of the pulse duration of 599.6 fs, the measured pulse duration is a factor 1.3 larger than the theoretical expectation. This is explained by higher order dispersion which can not be compensated by the grating compressor.

An option to reduce the influence of the ASE is to increase the seed pulse energy of the amplifier. This was achieved by reducing the repetition rate of the fiber laser seeder to 20 kHz while keeping the output power constant. Thus, an increase of a factor of 5 could be achieved. The resulting energetics of the thin-disk amplifier are displayed in figure 5.12.

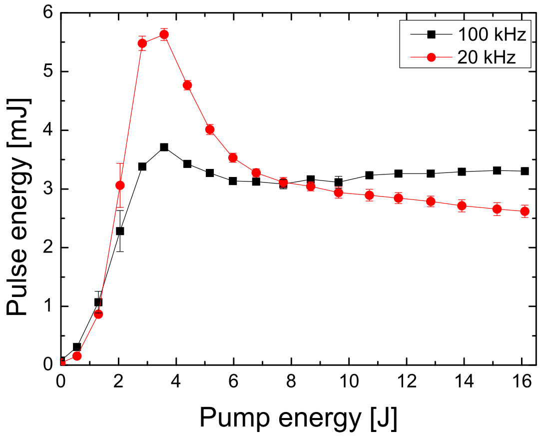

Figure 5.12: Comparison of the amplified pulse energies for 100 kHz and 20 kHz repetition rate in the thin-disk amplifier. For the 20 kHz case, the single pulse energy reaches a higher value than for the 100 kHz case, which is explained by a more sufficient suppression of ASE for a higher seed energy.

It can be seen that the maximum output pulse energy could be doubled by increasing the seed pulse energy. However, ASE is still setting in at around 3 J of pump energy. For pump energies of 8 J and above, the output energy is even smaller than for the lower pulse energy at 100 kHz repetition rate from the seeder. This can be explained by the longer pumping phase in between two amplified pulses, where ASE can be amplified to higher levels, especially at very high pump powers. But these results are promising concerning the use of a 500 W Innoslab amplifier as seed source for the thin-disk amplifier (see section 5.3).

5.2.3 Non-beveled disk, 7.3 mm pump

The next step for reducing the influence of ASE is the reduction of the pump spot diameter. This has on the one hand the effect that ring-type ASE modes are suppressed due to the smaller interaction cross section with the pumped volume of the disk. On the other hand, this increases the intensity of the pump light in the pumped volume. Since the diameter of the seed beam is much smaller than the 9.6 mm pump spot diameter of the first tests, this has no influence on the mode matching in the amplifier. Thus, the inversion available for the seed amplification is increased. A measurement of the pump spot diameter after changing the pump collimation optics is shown in figure 5.13.

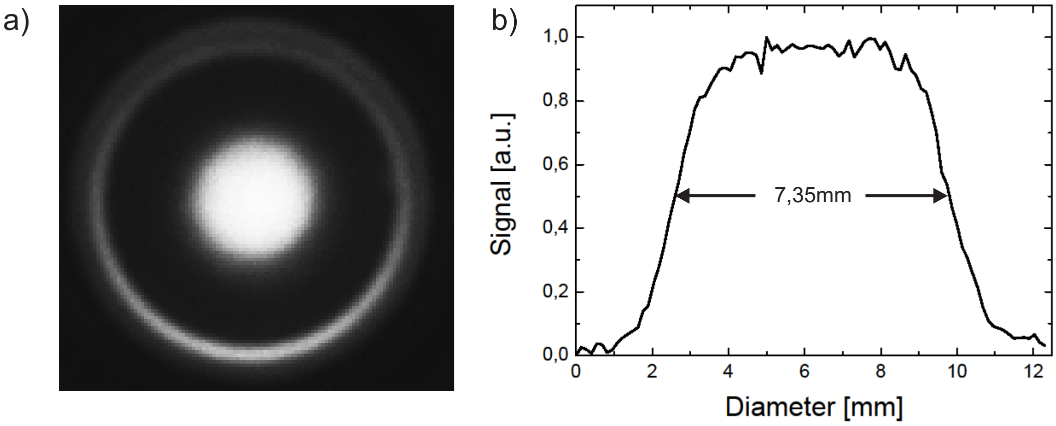

Figure 5.13: Pump profile (a) and line-out (b) of the pump spot on the disk.

From this figure, the FWHM diameter of the pump spot radius is determined to 7.35 mm. With the parameters stated in section 5.1.2 and according to equation 5.1, this leads to an intensity of the pump beam of 29.2 kW/cm^2, which is nearly twice the pump intensity as for the large pump spot diameter. The resulting energetics of the thin-disk amplifier with the smaller pump spot size are presented together with the simulation results in figure 5.14.

For comparison with the larger pump spot, the corresponding energetics curve is also displayed in figure 5.14a. It can be seen that there is still an effect of the ASE for higher pump energies, but the threshold of the inset of these effects has been increased to 7 J pump energy. The gain reaches a maximum and drops again for higher pump energies. This is the same effect as already stated in section 5.2.2. The maximum achievable burst energy of the thin-disk amplifier is 2.05 J, which corresponds to an average pulse energy of 25.6 mJ in the burst at 100 kHz pulse repetition rate. The corresponding optical efficiency is displayed in figure 5.14b. The maximum achievable optical conversion efficiency is 42.3 % at 3.8 J pump energy, which is tremendously higher than with the larger pump spot diameter (a factor of around 5). At the full output power of the amplifier, a stability measurement was performed. The results of this measurement are displayed together with the corresponding burst shape in

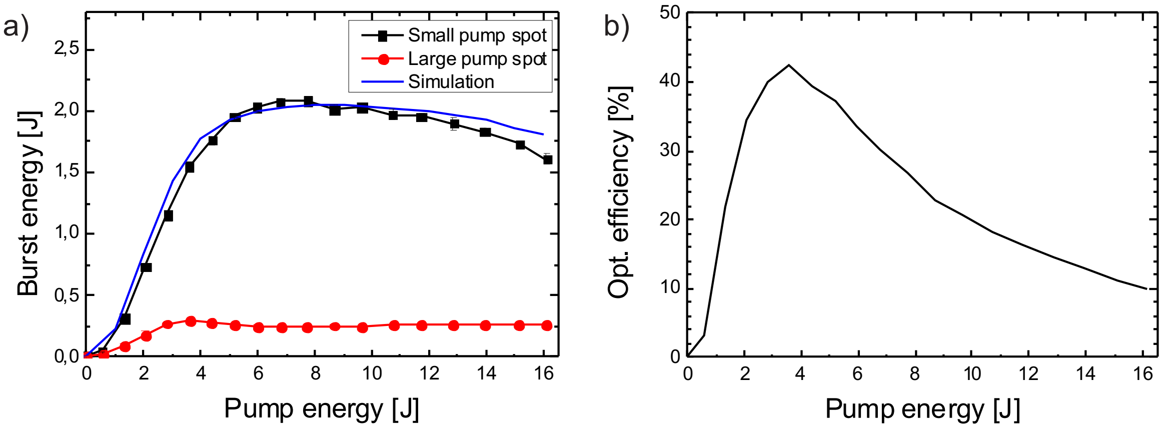

Figure 5.14: Results of thin-disk amplifier with 7.35 mm pump spot and a non-beveled disk. a) Amplifier characteristics of the output burst energy depending on the pump energy (black) together with the simulated characteristics (blue). For comparison, the results with the large pump spot are displayed in red. b) Optical conversion efficiency from pump to seed in the case of the small pump spot.

figure 5.15.

The stability measured over 5 minutes is 0.9 % rms at an average output of 2 J burst energy. The burst profile at this output power showed an asymmetric shape. This is due to the limited time for re-pumping the gain medium. Thus, the inversion needed for the amplification of the later pulses can not be re-established by the pump. Additionally, ASE still plays a role for the amplification of the pulses. At the tailing edge of the burst, the amplifier output reaches an equilibrium such that the last 20 pulses of the burst have the same amplification factor. To achieve a flat burst shape, the pump energy of the amplifier was reduced 3.6 J. Thus, a nearly flat burst shape could be achieved. The resulting burst shape with the reduced pump energy is displayed in figure 5.16.

The output energy of the amplifier is in this case is 1.25 J, which corresponds to an average pulse energy in the burst of 15.6 mJ with a pulse to pulse stability of 2.4 % rms. The shape of the burst displayed in figure 5.16b still is not perfectly flat. It is very similar to the burst achieved with the large pump spot diameter shown in figure 5.10. The explanation for that behavior is again given by the dynamics of the ASE arising in the thin-disk gain medium. The increase at the beginning of the burst is explained by the reduction of ASE due to the fact that the seed depletes the inversion which is then not available for the ASE any more. At the tailing edge of the

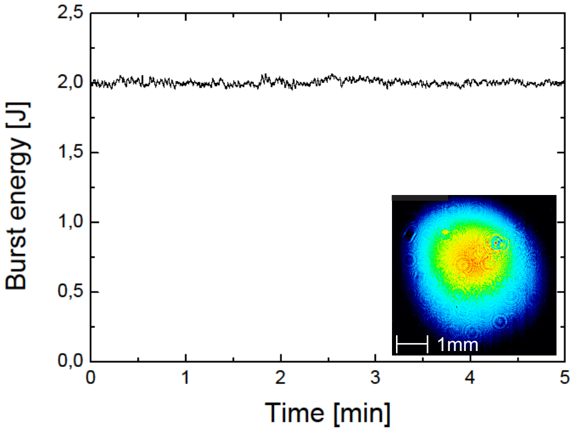

Figure 5.15: Stability measurement of the amplifier output at the maximum output power of the amplifier. The inset in this figure shows the beam profile of the amplified beam for the full 30 passes on the gain medium.

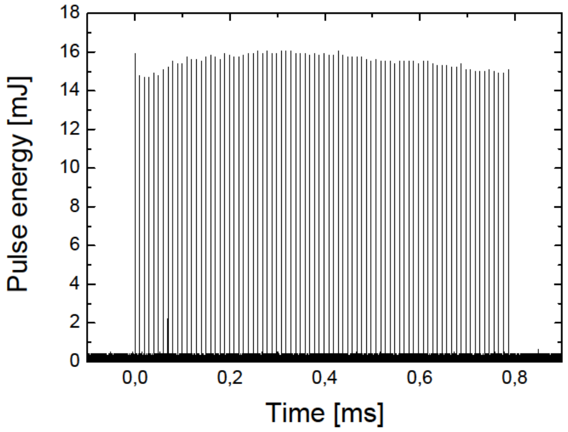

Figure 5.16: Burst profile of the amplifier output with reduced pump energy to achieve an optimized burst shape. The pulse to pulse energy stability is 2.4 % rms.

burst, the amplifier reaches an equilibrium.

With the reduction of the pump spot diameter the output of the thin-disk amplifier could be increased by a factor of nearly 7. The fact that ASE effects are still present in the energetics as well as in the burst shape shows that the increase is not only due to a reduction of the ASE, but due to the increase of the pump intensity on the disk gain medium. Using equation 2.55, it can be calculated that the ratio disk radius and pump spot radius needs to be at least 1.817 (this ratio is then given by the ratio of the refractive indices). This is nearly the case for a pump spot of 9.63 mm diameter and a disk diameter of 17 mm, where the ratio can be calculated to 1.765. Thus, the effect of further reducing the pump spot diameter is relatively small. The ratio for the smaller pump spot of 7.35 mm is then calculated to 2.313. For a further reduction of the ASE, beveling of the disk boundaries is the next step, which is presented in the next sections. Since this was done directly after the achievements presented in this section, no pulse compression measurements where performed. The primary goal for the further development of the thin-disk laser was to reduce the ASE to an absolute minimum.

5.2.4 Beveled disk, 7.3 mm pump

The third way of reducing the effect of ASE in the thin-disk amplifier is beveling the disk boundaries. This was already described in section 2.3.7. The beveling angle introduced in the thin-disk setup is 60°, measured between the back plane of the disk and the disk boundaries, according to figure 2.13. Thus, most of the ASE modes which develop in the gain medium are coupled out of the disk at the boundaries. This leads to very high output powers of the disk laser, as will be described in the following. The results for the energetics and optical efficiency are displayed in figure 5.17.

Again, for comparison with the results achieved in the last step, the results for the non-beveled disk are displayed together with the results for the beveled disk (figure 5.17a). The comparison with the simulation will be presented in section 5.4. The output energy still shows a saturation effect starting around 7 J of pump energy, but this is now due to a saturation of the single pass gain, as will be further investigated in section 5.3. The maximum output energy could be increased to 3.56 J in the burst, which corresponds to an average pulse energy of 44.5 mJ. The average intra-burst output power of 4.45 kW is the highest reported for sub-ps thin-disk multipass amplifiers. The maximum optical conversion efficiency is measured to be 48.5 %, which is slightly higher than with the non-beveled disk, but at a higher pump energy of 5.2 J. The total amplification factor of the amplifier in this configuration is 118, which yields a single pass gain of 1.17 at full pumping power for the 30 passes on the thin-disk gain medium.

In figure 5.18a, the output burst at the maximum pump energy with the maximum output energy is shown. It is obvious that this burst has a very asymmetric shape. Like already explained in section 5.2.3, this is due to the limited re-pumping time in between the pulses in the burst. Unfortunately, the photo-diode was saturated during the measurement so that the first pulses in the burst could not be resolved.

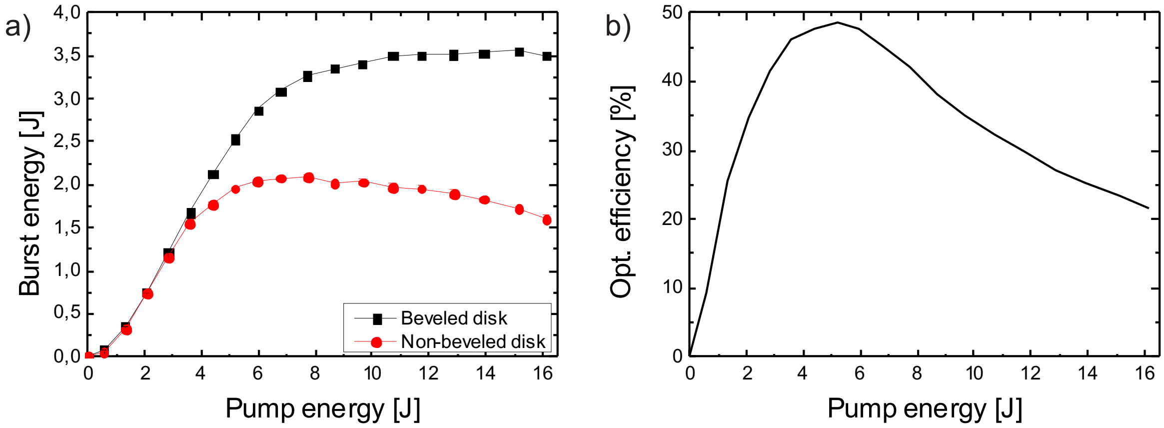

Figure 5.17: Results of thin-disk amplifier with 7.35 mm pump spot and a beveled disk. a) Energetics of the output depending on the pump energy. b) Optical conversion efficiency from pump to seed in the case of the beveled disk.

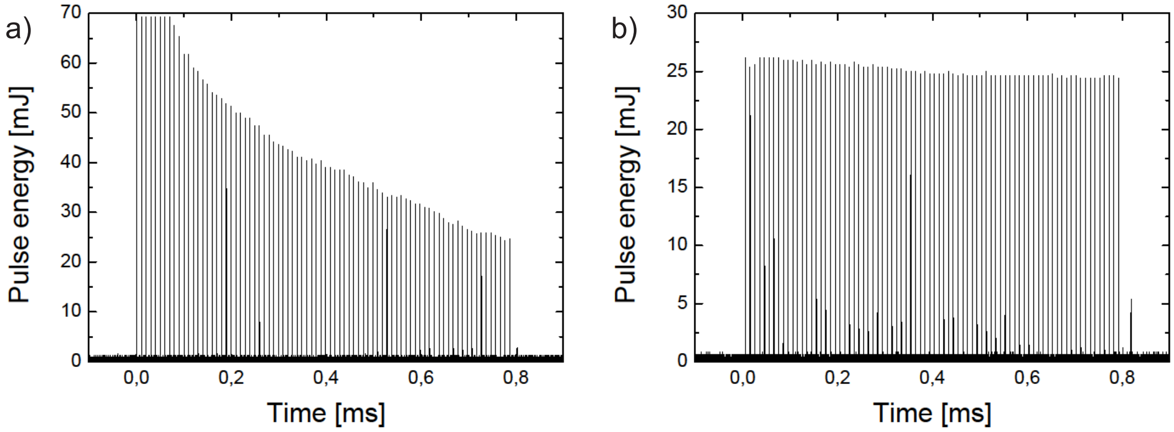

Figure 5.18: Burst shapes of the thin-disk amplifier output: a) Shape at full pump energy, b) optimized burst shape at 4 J pump energy. In the latter case, the pulse to pulse energy stability is measured to 2.3 % rms.

From the trend at the beginning of the burst, it can be estimated that the first pulses of the burst reach values of 100 mJ. To achieve a flat burst profile, the pump energy of the thin-disk amplifier was again reduced to a smaller value. At 4 J pump energy, a flat burst shape could be achieved, which is displayed in figure 5.18b. The output burst energy of the amplifier in this case was 2 J at this pump energy, corresponding to an average pulse energy of 25 mJ in the burst. The burst shape shows a very slight decrease over the burst, where the amplifier reaches equilibrium. The measured pulse to pulse energy stability is 2.3 % rms. This value is higher than the anticipated value of 1 %, which can be attributed to the slight decrease of pulse energy within the burst shape. Compared to the burst at full pump energy, the level of the flat burst corresponds to the last pulses of the burst at full pump energy. With the amplifier operating in the regime of a flat burst, a long-time stability measurement was performed. The duration of this measurement was 70 minutes. The results are shown in figure 5.19.

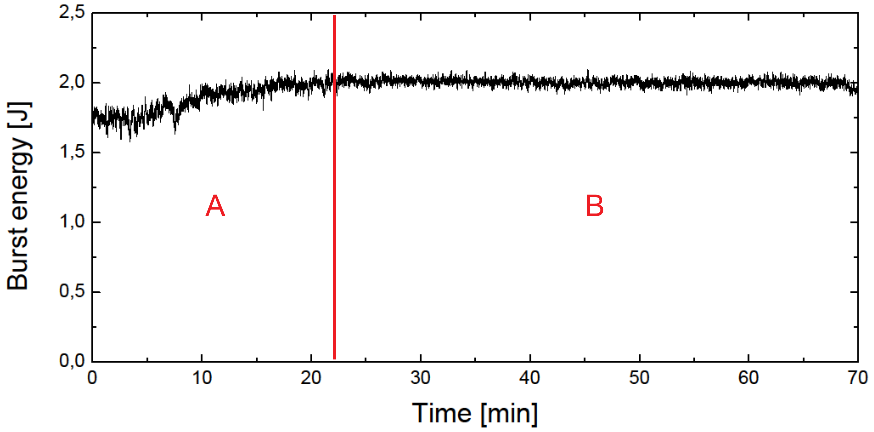

Figure 5.19: Stability measurement of the thin-disk amplifier with optimized burst profile. Section A depicts the warm-up phase of the amplifier, section B is the time with stable operation.

The plot is divided into two different sections, where different dynamics of the amplifier can be observed. In section A, the amplifier is in a warm-up phase, reaching a thermal equilibrium of all optics and the amplifier medium itself. This can be seen by the increase of the burst energy to its maximum value of 2 J at the end of section A. Section B shows the stable operation of the amplifier for more than 45 minutes, which is also shown together with a spatial beam profile of the amplifier output in figure 5.20.

The stability measurement shown in figure 5.20a yields an operation stability of the amplifier of 1.1 % rms over 46 minutes. Compared to the results of the non-beveled disk, this means an improvement in the stability of nearly a factor of 2. The beam profile of the amplifier is shown in figure 5.20b. The ellipticity is 0.9. The output

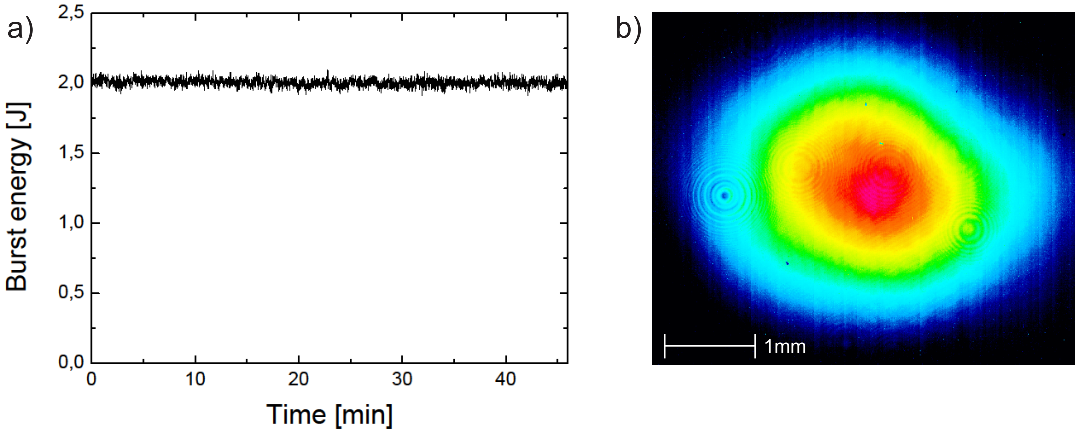

Figure 5.20: a) Detail view of the stable area of the thin-disk amplifier. b) Beam profile of the output beam taken during the stability measurement.

pulses were compressed in the grating compressor after amplification. The results of the compression are shown together with in- and output spectrum in figure 5.21.

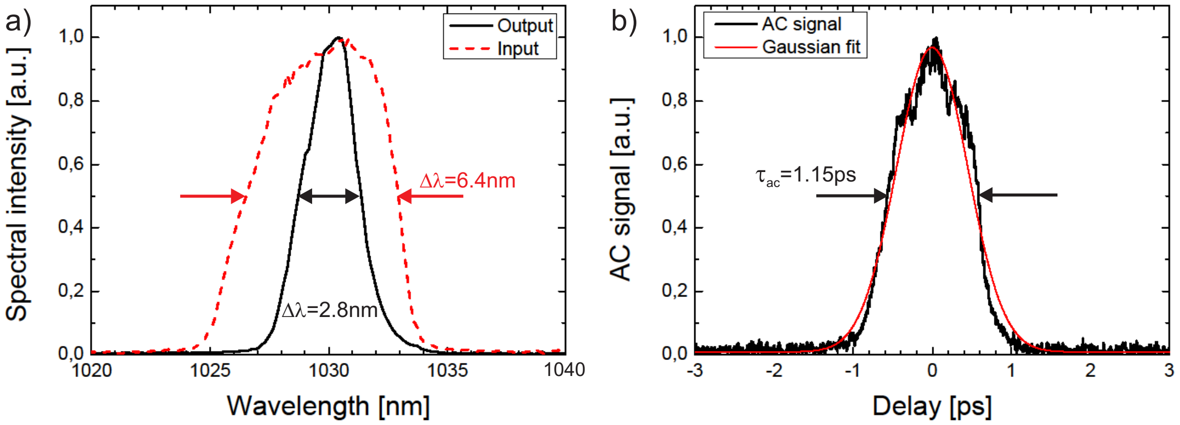

Figure 5.21: a) Spectra of the input (red) and output (black) beams of the thin-disk amplifier. b) Autocorrelation trace of the compressed pulses.

As in the experiment with the large pump spot diameter, the spectrum shown in figure 5.21a was gain narrowed from 6.4 nm to 2.8 nm. The autocorrelation shown in figure 5.21b yields an autocorrelation width of 1.15 ps FWHM. Assuming a Gaussian pulse shape, this leads to a compressed pulse duration of 815.6 fs. This is slightly longer than the result for the large pump spot.

The compressed pulses have been used for second-harmonic generation (BBO crystal with a thickness of 1 mm and type-I phase matching) with an output burst energy of 2.5 J. The resulting burst energy in the second harmonic has been measured to 1 J, corresponding to a pulse energy in the burst of 12.5 mJ. The efficiency of the compressor has been measured to be 80 %, which leads to a compressor output burst energy of 2 J. The SHG burst energy of 1 J then yields a SHG conversion efficiency of 50 %. This leads to a total compression-conversion efficiency of 40 %. The stability of the second harmonic output has been measured to 1.9 %. Due to the nonlinear behavior of the second-harmonic generation process, it is very sensitive to fluctuations of the peak power of the incident laser pulses. This leads to a worse stability of the SHG output. In addition to that, the spatial pointing stability of the amplifier plays an important role. If the pointing in the compressor changes, a slightly different compression of the laser pulses follows. This then manifests in a different peak power of the laser pulses, changing the efficiency of the SHG process. The pointing stability from the fiber laser source has been measured to 40 μm rms with a beam size of 2 mm FWHM. After 15 passes, the stability decreased to 100 μm rms and after 30 passes, the stability was measured to 160 μm rms.

Beveling the disk boundaries had a large impact on the dynamics of the ASE. As will be shown in the next section, this measure is already sufficient for reducing the ASE in the thin-disk gain medium. The output of the thin-disk amplifier is now limited by a saturation of the single pass gain on the thin-disk gain medium.

5.3 Hybrid Innoslab-Thin-disk amplifier

The last experiment for reducing the ASE in the thin-disk amplifier is to increase the seed pulse energy as already stated in section 5.2.2. An Innoslab amplifier with an output power of 500 W (see section 5.1.2) has been implemented in the experimental setup. The total output energy of this Innoslab amplifier is 400 mJ per burst, corresponding to a pulse energy of 5 mJ. Due to space reasons on the optical table, the total number of passes on the thin-disk gain medium had to be reduced in order to keep small angles on the thin-disk, which then also has an impact on the stability of the output energy of the amplifier. The number of passes used for the experiment was 10. The position of the individual optics in the mirror array and in the back reflecting array is shown in figure 5.22.

There, only one defocusing mirror is needed for the entire multipass setup. The results of the Innoslab seeded thin-disk amplifier are shown in figure 5.23.

The fiber seeded results are also included in the energetics curve shown in fig-

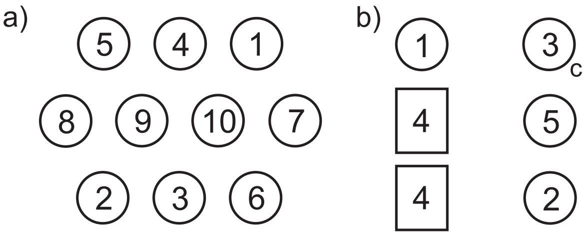

Figure 5.22: Position of the individual mirrors in the array. a) Mirror array for the 5/10 passes on the thin-disk module, b) back reflecting mirror array for the new beam path after every pass on the thin-disk gain medium. The curved mirror is marked with a *c*.

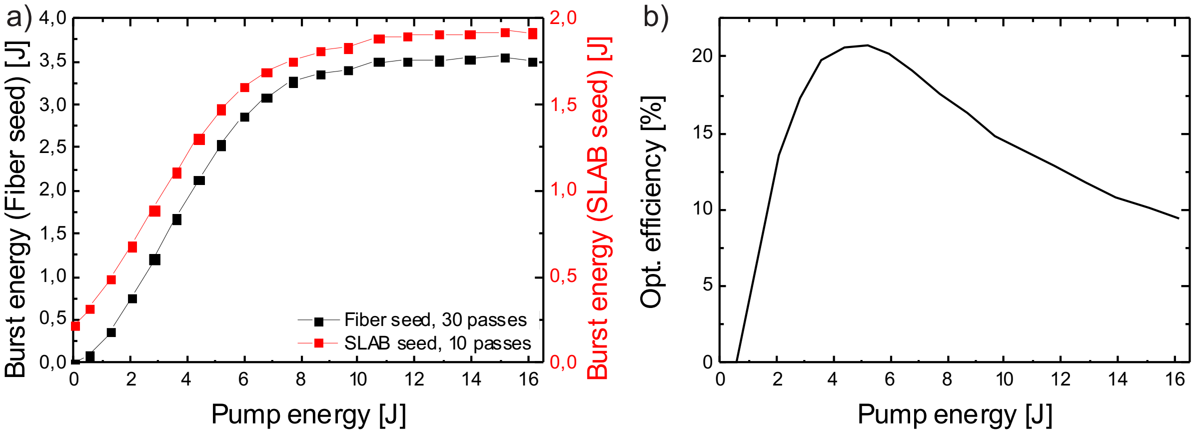

Figure 5.23: Results of thin-disk amplifier with a 5 mJ Innoslab seeder. a) Energetics of the output depending on the pump energy. b) Optical conversion efficiency from pump to seed for the Innoslab seeder.

ure 5.23a for comparison. The results of the simulation for this setup will be presented in section 5.4. It can be seen that the two gain curves have the same amplification characteristics. This leads to the conclusion that already with the beveling of the disk boundaries the influence of the ASE could be reduced such that the limiting factor of the amplifier is a saturation of the single pass gain. The maximum output energy of the Innoslab seeded disk amplifier is 1.96 J in the burst, corresponding to a pulse energy in the burst of 24.5 mJ. Together with the 400 mJ burst energy from the seeder, this leads to an amplification factor of 4.9 with the 10 passes of the thin-disk setup. The single pass gain calculated from these numbers is 1.17, which is exactly the same as for the 30 passes. This shows that the gain of the amplifier is limited by the saturated single pass gain. At full output power of the amplifier, a stability measurement was performed for 5 minutes. The results of this measurement are shown in figure 5.24. The overall stability during this time period is 0.5 % rms at 1.96 J output energy.

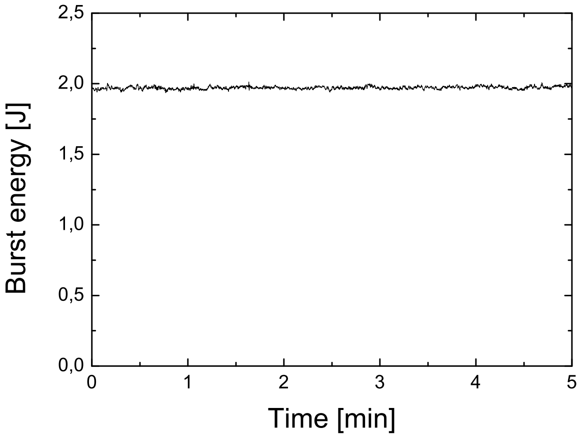

Figure 5.24: Stability measurement of the Innoslab seeded thin-disk output.

One important point to mention is the non-optimal Innoslab amplifier beam profile, as already discussed in section 5.1. Since the near-field of the amplifier is used for second-harmonic generation, a high quality Gaussian beam profile directly out of the amplifier is desirable. Figure 5.25 shows the beam profiles originating directly from the Innoslab amplifier and from the output of the thin-disk amplifier.

From this figure, it can be seen that the output profile of the Innoslab amplifier shows some wing structures on the left and right side of the main peak. To eliminate these structures, two different approaches can be applied. The first one is to introduce a spatial filter at the output of the amplifier, which on the other hand would reduce the pulse energy from the Innoslab amplifier. The second way which was introduced in the thin-disk setup is to use the pump spot of the disk amplifier as a soft aperture for the beam. There, the input beam needs to be dislocated with respect to the pump spot on the disk. This leads to a decreased amplification of the corresponding areas of the beam profile. This was successfully tested with the setup, resulting in the output beam profile shown in figure 5.25b.

The amplified pulses from the Innoslab seeded thin-disk amplifier were then compressed in the grating compressor. The compressed pulse duration was measured with the PulseCheck 50 autocorrelator from APE. The measured autocorrelation width of the compressed pulses is 1.23 ps FWHM. Assuming a Gaussian pulse, a compressed

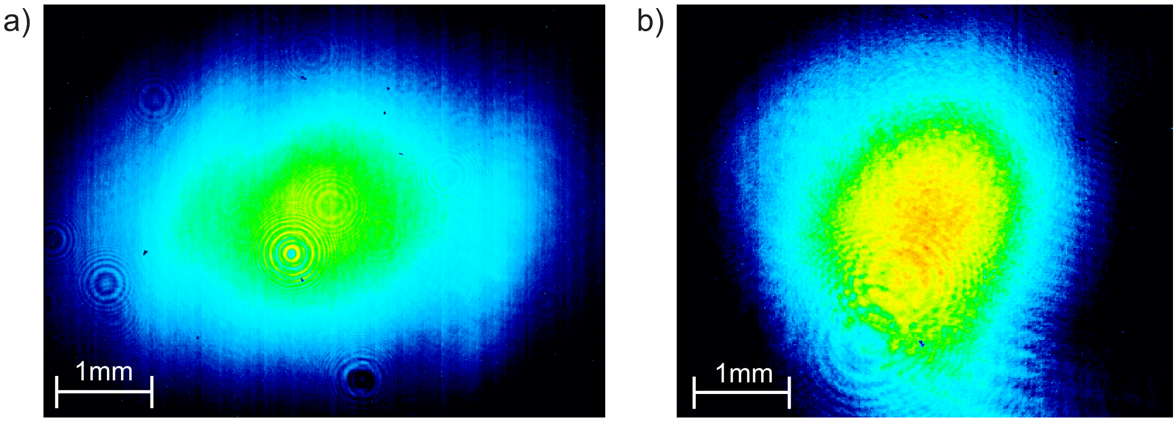

Figure 5.25: Beam profiles of the Innoslab seeder setup: a) input profile directly from the Innoslab amplifier, b) output profile of the thin-disk amplifier.

pulse duration of 872 fs is achieved. This is in well agreement with the measurement performed with the 30 pass fiber seeded thin-disk amplifier. The deviation of around 50 fs has its origin in the reduced resolution of the APE autocorrelator compared to the single-shot autocorrelator used for the measurements stated in section 5.2.

5.4 Comparison of results with simulation

The simulation code introduced in chapter 3 can be used to determine the influence of the ASE on the dynamics of the thin-disk amplifier. The results of the thin-disk with fiber seed, small pump spot and beveled disk as well as for the Innoslab seeder are modeled in the code. The free parameters of the ASE influence are then modeled such that the resulting energetics fit to the results achieved in the two experiments. This is in principle done by taking the parameters stated in chapter 3 and finding a reflection of the ASE at the disk boundaries where the results fit best to the measured values. The resulting curves are displayed in figure 5.26.

It can be seen that for both cases, the fiber seeded thin-disk amplifier shown in figure 5.26a and the Innoslab seeded thin-disk laser shown in figure 5.26b, the simulated energetics fit very well to the measured values. This has been achieved with an effective reflection value of the ASE at the disk boundaries of 12.5 %. This number appears to be high for a beveled disk, where the ASE modes should be completely coupled out at the disk boundaries. But it has to be taken into account that this code uses only one dimension and not all ASE modes which can evolve in the disk can be included. The only modes which are taken into account are the exclusively radial modes which have a normal angle of incidence on the disk boundaries. The

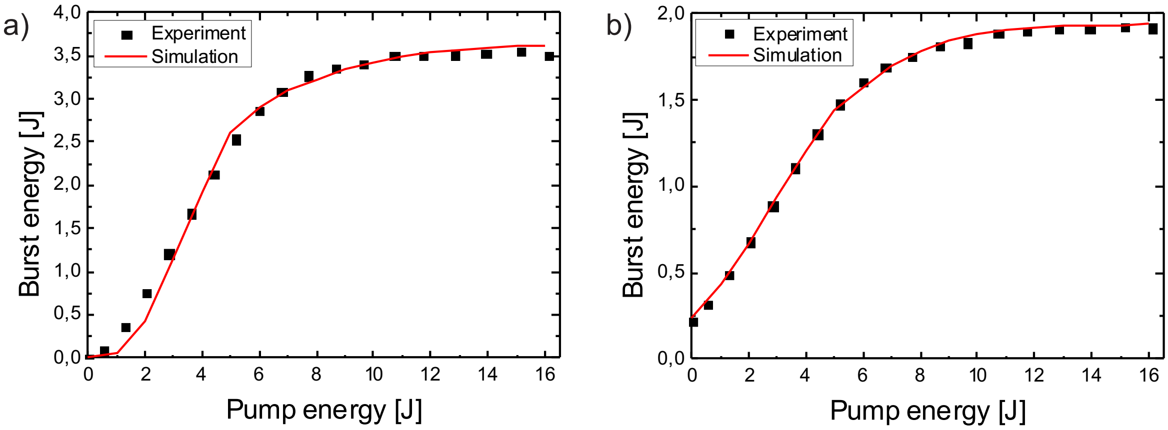

Figure 5.26: Reproduction of the experimental results with the simulation code: a) Fiber seeded thin-disk laser, b) Innoslab seeded thin-disk laser. A good agreement between the simulated and experimental results can be observed in both configurations of the amplifier setup.

modes which are a mixture of ring-type and radial modes need to be modeled by a relative reflection coefficient at the disk boundaries. With the code parameters set for simulation of the thin-disk amplifier dynamics, an estimation of what is needed to push the output energy of the amplifier to higher values can be made.

The plan is to use a cascade of two thin-disk amplifiers seeded by the high power Innoslab amplifier to reach the 10 kW power range. Therefore, simulations have been performed with a 1 kW Innoslab seed for the first thin-disk amplifier with a disk thickness of 750 μm in order to estimate which is the highest output burst energy with a number of 7 passes on the thin-disk gain module. Then, the output of the first thin-disk amplifier is used as a seed for a second thin-disk amplifier. This thin-disk is 360 μm thick and has already been used for the other experiments presented above. The results of this simulation are displayed in figure 5.27.

From figure 5.27a it can be seen that with the 750 μm disk a total amplification to 5.5 J is achievable. This output burst energy corresponds to a pulse energy of 69 mJ or an intra-burst output power of 6.9 kW at 100 kHz pulse repetition rate, respectively. The total gain for the first stage of thin-disk amplifier in this case would be 6.9, which corresponds to a single pass gain of 1.32. If this output is taken as a seed for a second stage of thin-disk amplifier, the resulting output burst energy reaches a value of 12.1 J, which then corresponds to 151 mJ pulse energy or 15.1 kW intra-burst output power. For the second thin-disk amplifier, the total gain would be 2.2, which corresponds to a single-pass gain of 1.12.

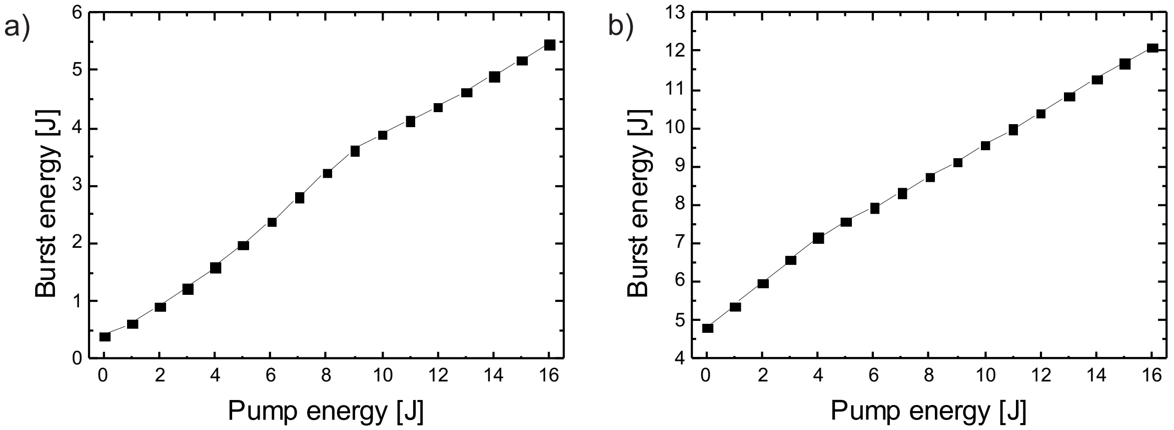

Figure 5.27: Simulation results for the two-stage cascaded thin disk amplifier. a) Performance of the first stage thin-disk with 1 kW Innoslab seed. The overall output burst energy of this amplifier stage is 5.5 J, which corresponds then to an intra-burst output power of 6.9 kW. b) Results for second stage thin-disk amplifier with the seed taken from the first amplifier stage. The maximum achievable output burst energy in this configuration is 12.1 J, corresponding to an intra-burst output power of 15.1 kW.

5.5 14 kW from 2 stage cascaded thin-disk amplifier

To reproduce the simulated results from section 5.4, a two stage cascaded thin-disk amplifier setup has been implemented in the laser system. The setup has been performed similar to the simulations. The output of a 1.5 kW Innoslab amplifier has been used as seed for two cascaded thin-disk multipass amplifiers. Due to some problems with the spatial beam profiles originating from the Innoslab amplifiers, a spatial cleaning of the Innoslab output needed to be implemented. This reduced the available power for seeding the thin-disk amplifiers to around 900 W. A block diagram of the experimental setup can be found in figure 5.28.

The first thin-disk amplifier amplifies pulses to an output burst energy of 5.4 J. This results with the 100 kHz intra-burst repetition rate and the burst length of 800 μs to an intra-burst output power of 7 kW. The gain of this amplifier is then 7.5, with a single pass gain of 1.33 for the 7 passes on the thin-disk gain medium. Furthermore, the output characteristics of the first stage thin-disk amplifier are in good agreement with the simulations presented in section 5.4. The resulting properties of the amplifier

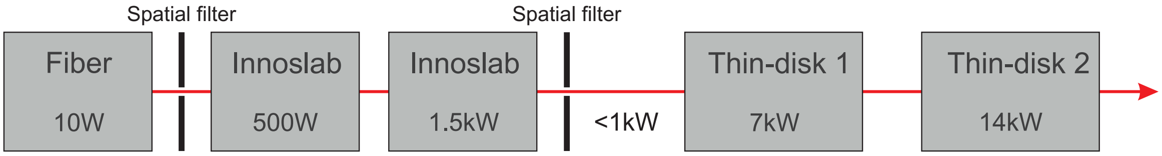

Figure 5.28: Block diagram of the amplifier setup. A 10 W output of the fiber laser is used to seed the 500 W Innoslab amplifier and the subsequent 1.5 kW booster amplifier. Before being used as seed for the disk amplifiers, the output needs to be spatially filtered to get a Gaussian beam. The first thin-disk amplifier then produces an output intra-burst power of 7 kW, which is then amplified to 14 kW in the second thin-disk amplifier.

are shown in figure 5.29a (black dots) together with the simulated results (red line). The single pass gain is nearly double as for the thinner disk. This is in well agreement with the simulations as well as with the assumption that a disk with double thickness should deliver a double single pass gain.

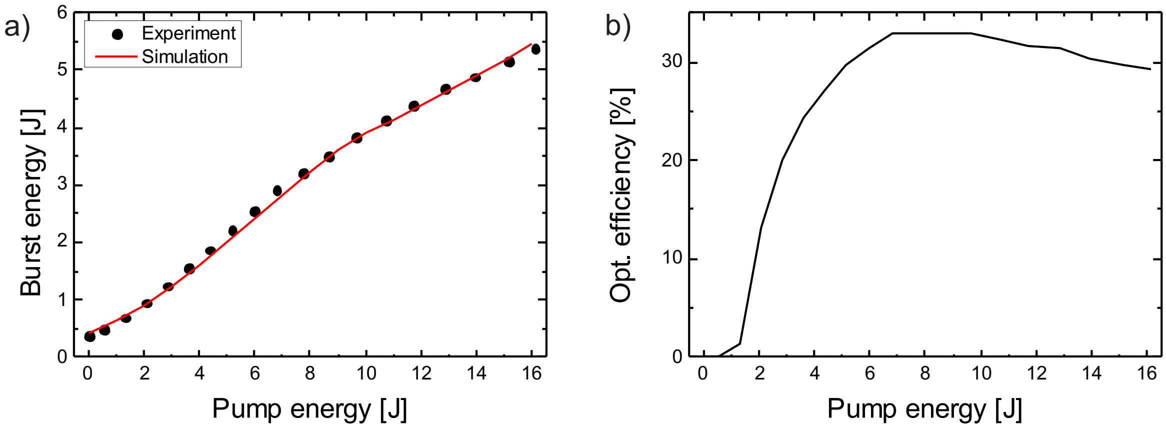

Figure 5.29: Results of the amplification in the first thin-disk amplifier with a 750 μm thick gain medium. a) Amplification characteristics (black dots) together with the simulated results (red line). The experimental results are in well agreement with the simulated values. b) Optical conversion efficiency in the amplifier. The maximum achieved optical conversion efficiency is 33 %.

The optical efficiency of the amplifier shown in figure 5.29b has a maximum value of 33 % at a pump energy of 7 J. For higher pump energies, the conversion efficiency is slightly decreasing which is due to ASE effects in the disk. At full pumping energy, the conversion efficiency is still 30 %, which leads to an extracted energy in the amplifier of 4.8 J. The burst energy stability measured over 5 minutes is 2.5 % rms. The corresponding measurement is shown in figure 5.30a.

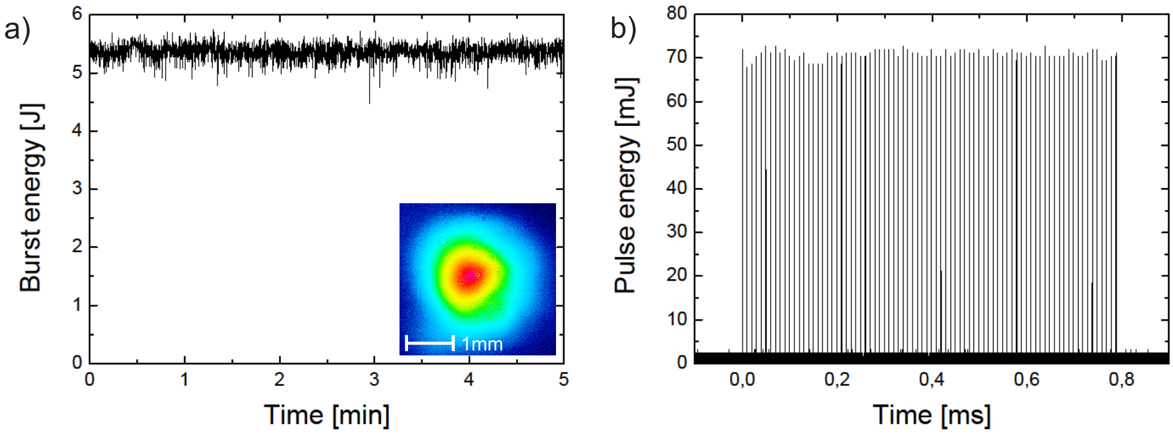

Figure 5.30: Stability measurement of the first thin-disk amplifier. a) Burst energy stability measured over 5 minutes, showing a peak to peak fluctuation of around 1 J, most likely caused by air fluctuations originating from the flow boxes (rms stability of 2.5 %). The inset shows the output beam profile of the amplifier. b) Output burst shape of the amplifier. The shape of the burst shows to be nearly flat with an average output pulse energy of 70 mJ over the entire burst pattern. The measured pulse to pulse energy stability is 1.9 %.

The high peak to peak fluctuations of around 1 J can be explained by pointing fluctuations in the multipass setup. These originate from air fluctuations and the long beam path in the amplifier, since no imaging is used in the experimental setup. The beam profile of the amplifier output is presented in the inset of figure 5.30a. In figure 5.30b, the profile of the output burst is shown, which is flat over the entire pattern. The measured pulse to pulse energy stability for the output burst is 1.9 %. This value is still above the anticipated value of 1 %, but this can be attributed to air fluctuations in the experimental setup. By stabilizing the pointing of the amplifier, also the pulse to pulse fluctuations are due to be reduced. The output of this amplifier has been used to seed a second thin-disk amplifier with another 7 passes on a thin-disk gain medium of 360 μm thickness. The results of this second stage amplifier are shown in figure 5.31. The experimental amplifier characteristics are shown as black dots in figure 5.31a together with the simulated results as a red line.

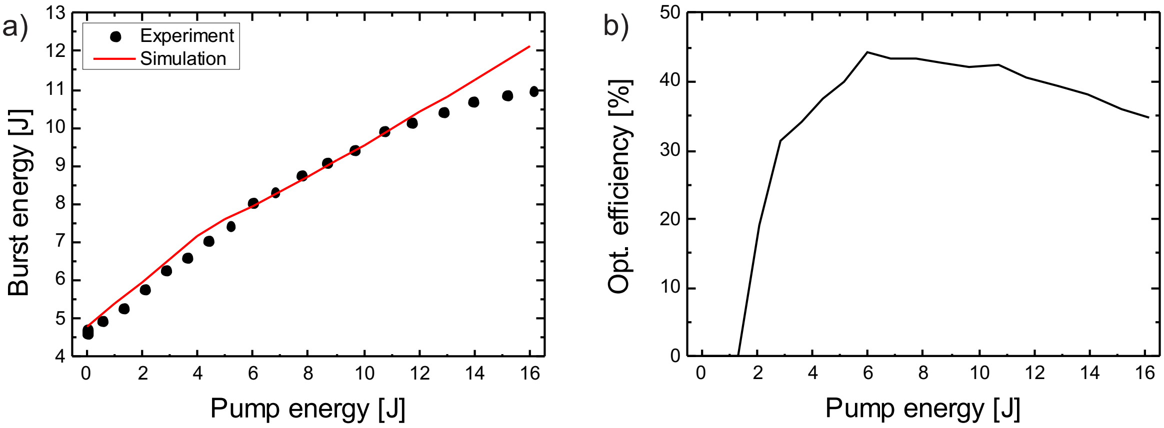

Figure 5.31: Results of the amplification of the second stage thin-disk amplifier, seeded by the full output power of the first thin-disk amplifier stage. a) Amplifier characteristics (black dots) together with the simulated results (red line). The experimental values show a deviation of the output burst energy at high pumping energies. b) Optical conversion efficiency in the second thin-disk amplifier. The maximum achievable conversion efficiency is 44 %.

It can be seen that the experimental results of the amplifier start to deviate from the simulation at a pump energy of around 11 J. This can be explained by the amplification process itself. Due to the high conversion efficiency of around 42 % in this amplifier stage (see figure 5.31b), the pulses in the burst extract an amount of energy which can not be re-established by the pump in the short time until the subsequent pulse. Thus, the amplification of the pulses is not constant during the burst pattern which leads on the one hand to a reduced conversion efficiency for high pump energies and on the other hand to an asymmetric burst shape of the amplifier output at full pumping power. This burst is shown in figure 5.32b. The single pass gain for this amplifier at full pump energy is 1.1, while the simulated single pass gain reaches a value of 1.13.

In figure 5.32a, the stability of the second stage thin-disk amplifier is shown. The measured rms stability of this amplifier output is 3 %, while the peak to peak fluctuation reaches a value of 2.3 J. This is higher than in the first stage and can be explained again by pointing fluctuations in the multipass setup. These are due to the extended beam path for the second multipass higher than in the first and are affected again by air fluctuations and the pointing stabilities of the precedent amplifier stages. The inset in figure 5.32a shows the spatial beam profile of the output of the second thin-disk amplifier. The burst profile shown in figure 5.32b shows an asymmetric

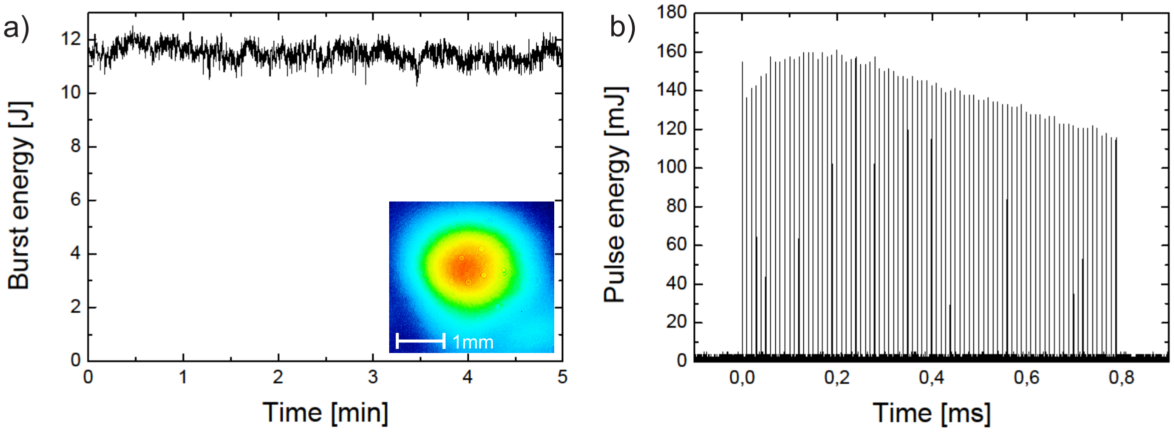

Figure 5.32: Stability measurement for the second thin-disk amplifier. a) Stability measured over 5 minutes, showing a peak to peak fluctuation of 2.3 J caused by air fluctuations (rms burst energy stability of 3 %). The inset in a) shows the spatial beam profile of the amplified pulses. b) Burst profile of the amplified pulses. An asymmetric behavior can be observed.

shape, which is caused by the high gain for the first amplified pulses in the laser active medium. This effect has already been described in section 5.2.3. The spectral width of the amplified pulses is measured to be 2.8 nm, which is in well agreement of the precedent measurements with Yb:YAG amplifiers. Therefore, compression of the pulses to sub-ps pulse durations is expected.

In conclusion, it has been shown that it is possible to reach intra-burst output powers well above the 10 kW level. With the setup shown here, a total intra-burst output power of more than 14 kW was demonstrated. At 100 kHz repetition rate, this implies an average pulse energy in the burst of 140 mJ. In order to reach a flat burst envelope, the repetition rate of the entire amplifier system can be increased such that the extracted energy per pulse is reduced. This measure would also allow to reach high pulse energies at higher repetition rates, for example 14 mJ at 1 MHz repetition rate, which would be the full intra-burst repetition rate of the FLASH facility.

5.6 Pump-seed synchronization

This section is dedicated to the synchronization of pump and seed pulses in the OPCPA system. The measurements presented here are performed with a two-crystal balanced cross-correlator (see section 4.5). First tests were performed using 1030 nm pulses from the fiber amplifier which are cross-correlated with a fraction of the seed pulses from the oscillator.

In addition to the measurements with the balanced cross-correlator, the possibility of controlling the timing drift with the spectral center of gravity (COG) of the OPCPA output pulse spectra is investigated. The COG is calculated by:

$$COG = \frac{\sum_i \lambda_i \cdot I(\lambda_i)}{\sum_i \lambda_i}, \tag{5.3}$$

where λ_i is the wavelength and $I(\lambda_i)$ is the corresponding spectral intensity at the given wavelength.

5.6.1 Calibration of the Cross-correlator

For the calibration of the balanced cross-correlator, the signal was recorded while moving the delay stage in 10 μm steps. This corresponds to a delay of 20 μm (66.67 fs) per step. The measurement was performed by moving the delay stage every 5 seconds and recording the signal from the balanced cross-correlator. The result from this evaluation is shown in figure 5.33.

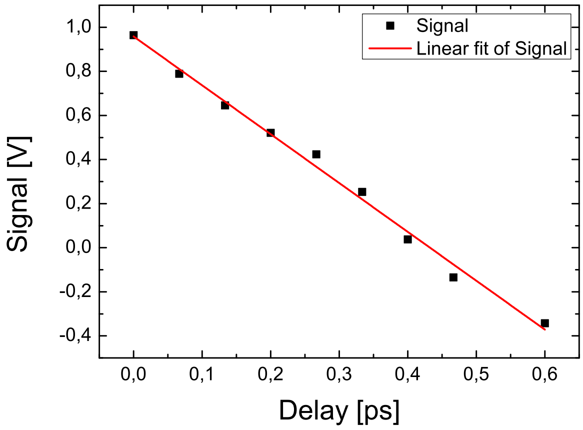

Figure 5.33: Calibration curve of the balanced cross-correlator. Shown is the evaluation of the first negative slope of the slope scan.

This can be fitted to estimate the slope of the cross-correlator and thus the calibration constant. From this fit, the slope of the signal is measured to 2.21±0.07 V/ps. This corresponds to a calibration constant of 451 fs/V. With this number, the temporal drift of the pump laser with respect to the seed laser can be measured. The deviations from the line fit in the evaluation are due to temporal drifts of the laser systems during the measurement.

5.6.2 Free-running system

The first measurement is performed to characterize the drift of the pump laser without any stabilization of the system. A one stage OPCPA setup was used for the experiment. The zero-crossing of the cross-correlator in the slope shown in figure 5.33 was set as starting point for the measurements. A measurement was started for 60 minutes where the output power of the OPCPA system, the output spectrum and the signal from the balanced cross-correlator were logged.

The measurements with the balanced cross-correlator in the free-running system are displayed in figure 5.34a. A positive temporal drift means that the seed pulses are positively delayed with respect to the pump pulses so that the leading edge of the pulses is amplified in the OPCPA system. A total temporal drift of up to 0.5 ps can be observed without stabilization. The dynamics of the OPCPA system follow directly the temporal drift of the amplifier system, which is shown in figure 5.34b. The control of the timing in the OPCPA setup is crucial for a stable operation of the whole system. The amplified spectrum was acquired with a Shamrock spectrometer (150 lines per mm grating, Andor iDus camera) in parallel to the output power of the OPCPA system to investigate the influence of the temporal drift on the spectral properties of the amplified output.

Figure 5.34c shows the evaluation of the spectral COG during the measurement. It is obvious that the COG follows the timing with a direction sensitive behavior. In figure 5.34d, the spectral scan of the OPCPA output is displayed as a 2D color map. For larger time drifts of more than 0.2 ps between pump and seed, a strong influence in the spectral intensity can be observed. This is the case between minutes 10 to 20 of the measurement. In principle, the spectral COG can also be used for stabilizing the timing of the pump and seed lasers. This has been investigated in more detail by correlating the measurements from the spectral COG with the signal from the balanced cross-correlator. A correlation plot of this measurement can be found in figure 5.35.

For a certain time delay between pump and seed, the dependence of the COG on the timing is a linear function. But for larger time drifts of more than 0.2 ps, the dependence enters a nonlinear regime. This leads to the conclusion that the spectral COG is only a good measure for smaller time drifts and thus might be sensitive to fast time drifts, where the balanced cross-correlator is a more robust way to measure the time delay. In addition, the measurements taken with the balanced cross-correlator are more precise.

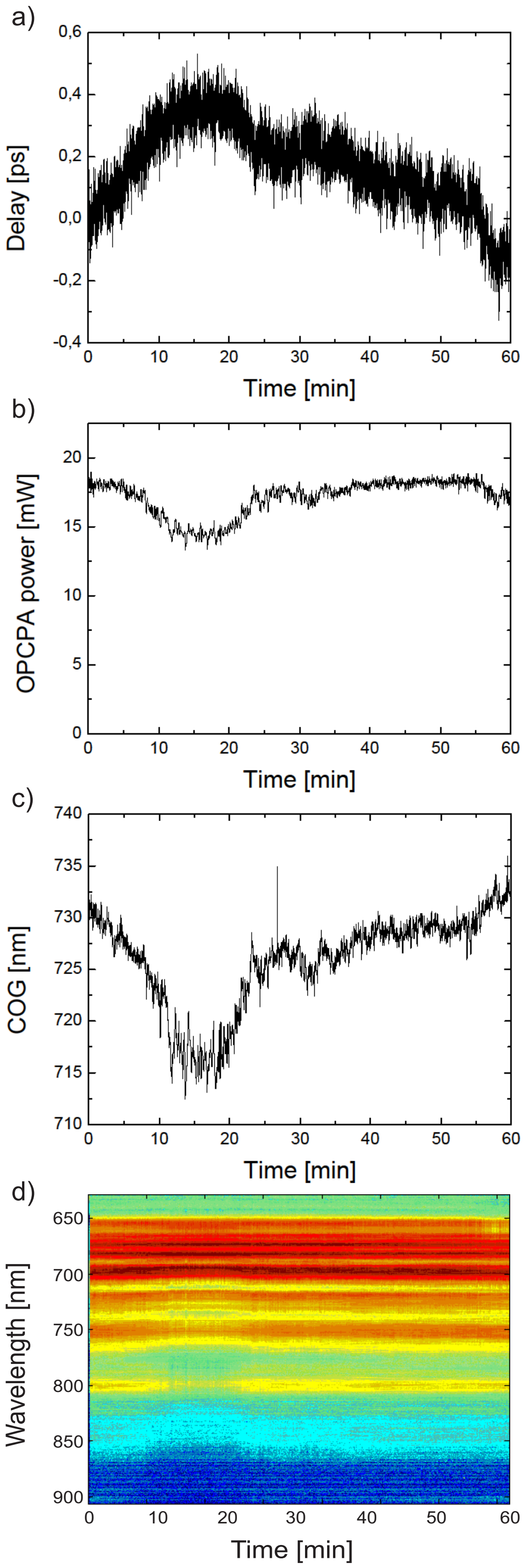

Figure 5.34: Results of the free-running system: a) Delay between pump and seed measured with the balanced cross-correlator. b) OPCPA output power. c) Center of gravity of the measured spectra. d) Output spectra of the OPCPA stage.

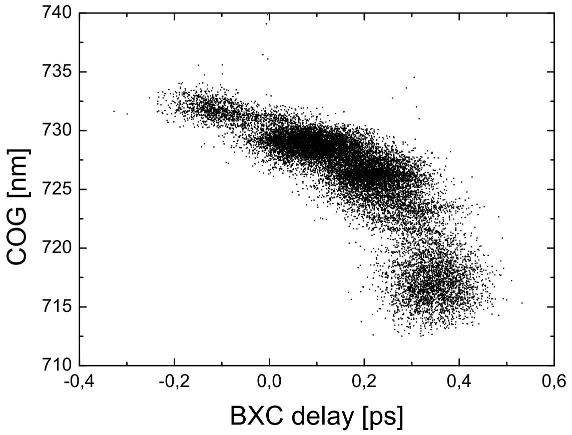

Figure 5.35: Correlation plot of the center of gravity (COG) and the balanced cross-correlator (BXC) measurements. For small time delays below 0.2 ps, the COG has a linear dependence on the temporal delay. For larger time delays, the correlation is nonlinear.

5.6.3 Stabilized system

For the stabilization of the amplifier system, the voltage signal from the balanced cross-correlator is used as a control signal for a delay stage which is implemented in the pump path of the amplifier. The stage is then moved with a proportional feedback from the balanced cross-correlator to account for the measured timing drift. The temporal drift of the pump pulses with respect to the seed pulses could be fully removed. This is shown in figure 5.36.

The remaining timing jitter for this measurement is 46 fs rms. The peak-to-peak fluctuations are in contrast still very high with a value of 350 fs. This is mainly due to the fact that the stage used for the stabilization is too slow for very fast feedbacks. This problem can be solved by using an only-electronic feedback system with a PID feedback system with a combination of the coarse delay stage and a piezo actuator which has a faster response time. Finally, the resolution of the balanced cross-correlator can be increased by implementing thinner BBO crystals for the signal generation and a thicker glass plate for a bigger temporal shift between the pump and signal pulses. The stability of the OPCPA output during the measurement is 1.2 % rms.

Figure 5.37 shows the measured spectra for the stabilized system. It can be observed that both the spectral stability and the position of the spectral COG have a much higher stability for the measurement period. The stabilization of the timing also results in a stable OPCPA output spectrum which is beneficial for the compressed

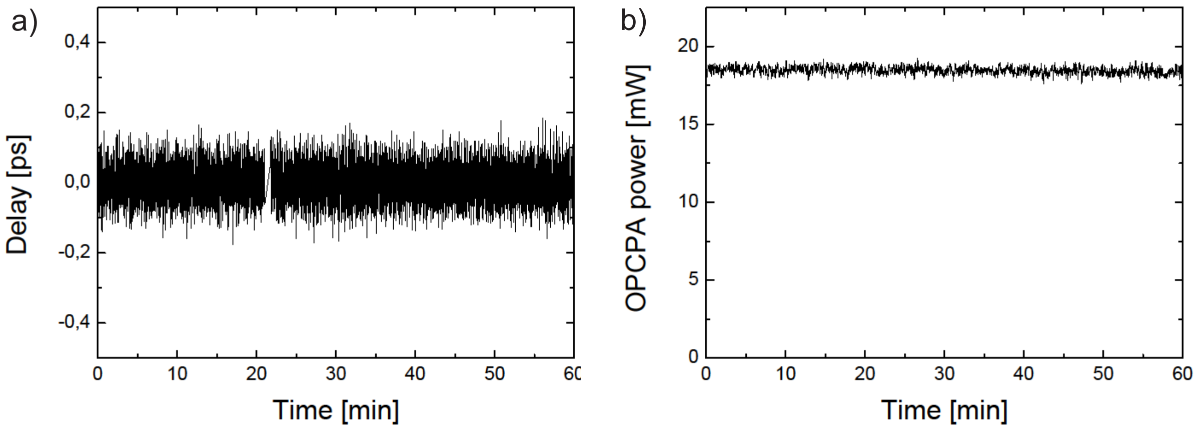

Figure 5.36: Stabilized OPCPA system: a) Delay between pump and seed measured with the balanced cross-correlator, b) OPCPA output power.

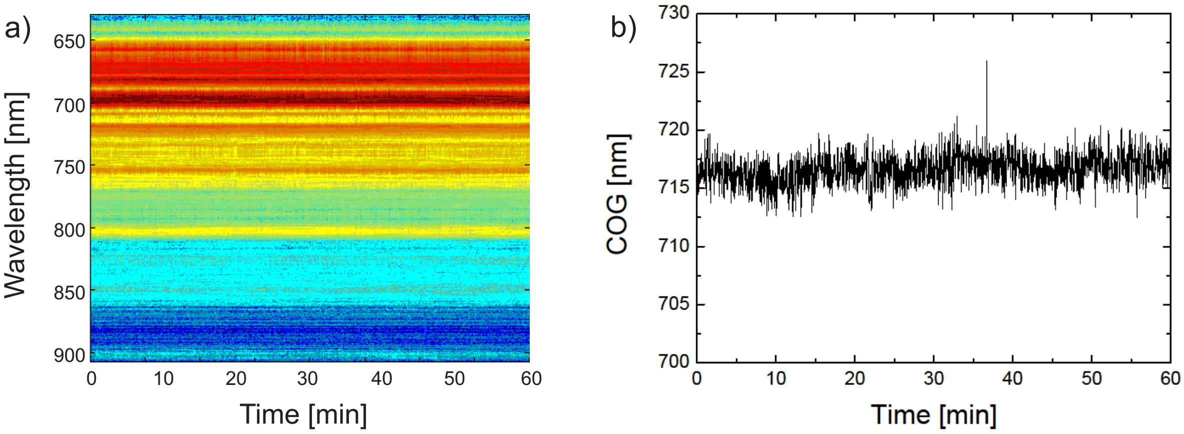

Figure 5.37: Spectral measurements of the stabilized system: a) Output spectra of the OPCPA stage, b) center of gravity of the corresponding spectra.

pulse duration of the entire amplification system.

5.6.4 Impact on the OPCPA system

To estimate the impact of the temporal fluctuations on the OPCPA output, additional simulations have been performed for a one-stage OPCPA setup[1]. The code consists of a 2D-model with the z-axis along the the signal propagation axis and a transverse axis (x-axis). The nonlinear coupled equations for signal, pump and idler are solved within the slowly varying envelope approximation using a fourth order Runge-Kutta split-step Fourier-algorithm. With this code, the influence of the timing on the amplification of ultra-broadband pulses was simulated. The spectrum used for the simulation code is the measured output spectrum of the Venteon oscillator (section 4.1). The time delay between pump and seed was changed in a range of -0.4 to 0.4 ps. The resulting dynamics of the OPCPA are displayed in figure 5.38.

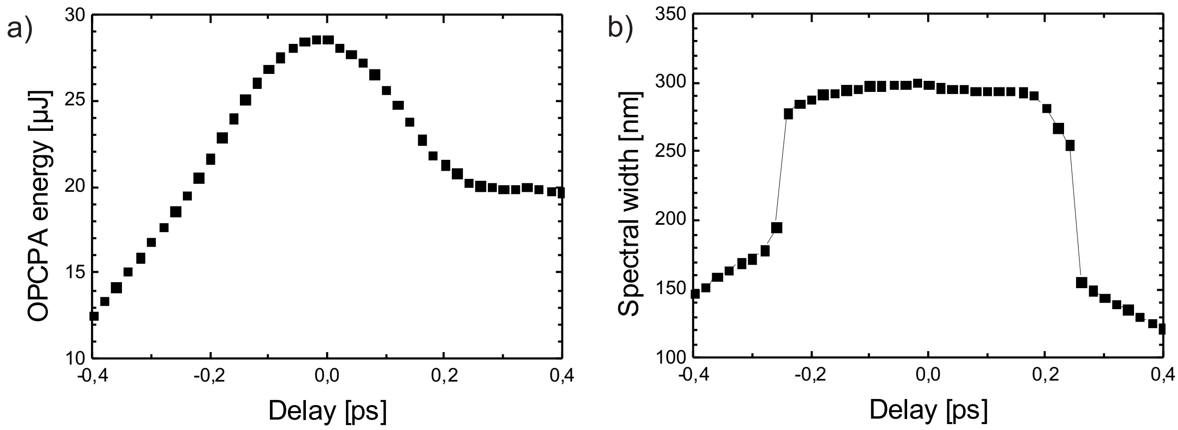

Figure 5.38: Simulation results for the broadband pulses (bandwidth of 650-1000 nm) with 5.76 fs Fourier-limited pulse duration. Influence of the timing delay on a) the output pulse energy and b) the spectral width of the amplified pulses.

As can be seen from figure 5.38a, the influence on the output energy is very sensitive around the delay where the maximum amplification is achieved. In contrast to this behavior, the influence of the timing on the spectral width is smaller (see figure 5.38b). A plateau with a width of about 0.4 ps is observable. The Fourier-transform-limited pulse duration achieved from the amplified spectrum is 5.76 fs.

In a second simulation run, an output spectrum supporting a Fourier-transform-limited pulse duration of 15 fs was used. The timing was changed again to investigate

---

[1] Simulation code kindly provided by Mark Prandolini.

the influence of temporal drift and jitter on the stability of the OPCPA output characteristics. The results of this simulation run are shown in figure 5.39.

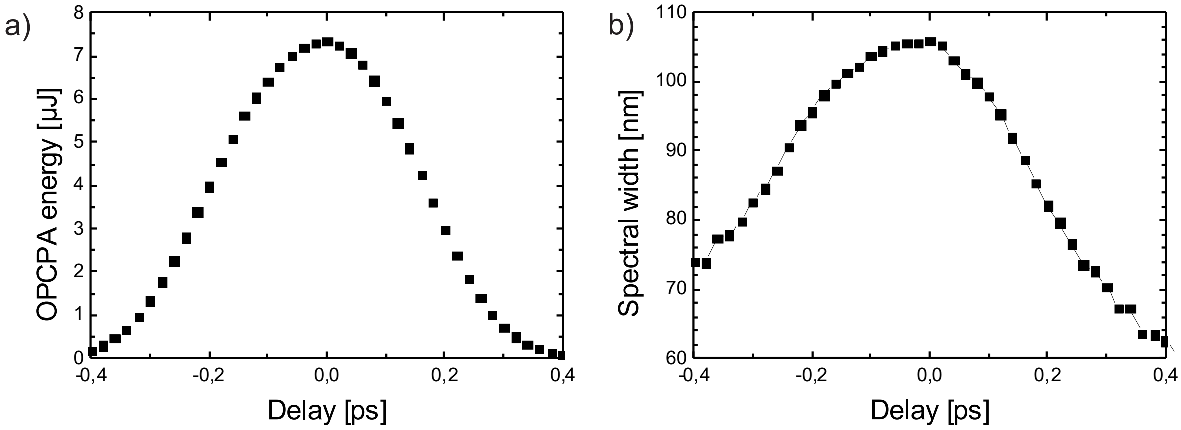

Figure 5.39: Simulation results for the narrowband pulses with 15 fs pulse duration. Influence of the timing delay on a) the output pulse energy and b) the spectral width of the amplified pulses.

It can be seen that the influence of the timing variations on the output pulse energy is similar to the case where the full spectrum was amplified (figure 5.39a). In contrast to the short pulse simulation stated above, the influence of timing variations on the spectral width has increased.

Chapter 6

Conclusion and outlook

In this work, the development and characterization of an Yb:YAG thin-disk multipass amplifier with outstanding output characteristics regarding the pulse energy and pulse duration at very high repetition rates has been presented. The fact that this amplifier is operated in a burst operation mode has made it difficult to find optimal operation parameters due to the non-equilibrium operating conditions of the amplifier. The challenge there was mainly to find a working condition where the output burst has a flat shape and therefore can be used for second-harmonic generation and in the end for pumping an OPCPA system.

Beneath the thin-disk amplifier, one topic of this work was to test amplifiers based on the Innoslab technology. This has been performed with three different types of Innoslab amplifier. First tests showed that the technology is capable of generating pulses with 20 mJ pulse energy at lower repetition rates. For the higher power Innoslab amplifiers, problems arose with the output beam profiles. In addition to that, the output power is restricted in this type of amplifier due to the mode area which is given by the dimensions of the slab gain medium. This problem can easily be overcome in the thin-disk laser technology by increasing the spot size on the gain medium.

First of all, an analytical model has been developed to understand the dynamics of such an amplifier operated in the burst mode. A two-step model has been developed including the dynamics of amplified spontaneous emission, which have to be considered for the development of a laser amplifier with these high average output powers. In addition to that, the operation of the laser in a burst-mode had to be taken into account.

A first experimental setup of the thin-disk laser has been developed with a fiber seeding source for the amplifier. There, 30 passes on the thin-disk gain module have been used to achieve a high amplification factor. Different methods to reduce the influence of ASE in the amplifier were explored. The first one was to reduce the pump spot size for a reduction of ring-type ASE modes and the second one was to bevel the disk boundaries. With these two methods, an amplification to the kilowatt output power range could be attained. The only limiting factor of the amplifier was then the single pass gain. The results of this setup were compared with the predictions made with the simulation code such that the dynamics of the ASE could be determined. The output characteristics of this amplifier setup were very promising concerning the output energy stability and the output beam profile. Due to the very high number of passes and the resulting length of the multipass of 120 m, the pointing of the amplifier output was still subject to strong fluctuations.

To circumvent the problem of the long multipass and to exploit a third measure to reduce the influence of ASE, a higher seed power was applied using an Innoslab amplifier with an output power of 500 W or 5 mJ pulse energy. This lead to the possibility of shortening the multipass of the thin-disk amplifier to 10 passes, which resulted in a total multipass length of about 20 m. The output characteristics of the thin-disk amplifier showed that again a single pass gain of 1.17 could be achieved, which was in well accordance to the results achieved with the fiber laser seeder. This showed that with the methods employed for the thin-disk amplifier, the ASE influence could be sufficiently reduced.

With a cascaded setup of two thin-disk amplifiers seeded by an Innoslab amplifier, output intra-burst powers exceeding the 10 kW level have been achieved. Therefore, only 7 passes per thin-disk module were needed to boost the power to the demanded values. The number of 14 kW of intra-burst output power is promising for the use of the amplifier system as OPCPA pump amplifier at high repetition rates reaching the 1 MHz frontier. This is of special interest for the application at the free-electron laser FLASH2, which runs with a maximum repetition rate of 1 MHz. Also for materials processing applications, this high intra-burst output power is very interesting in terms of an increased processing speed. During the experiments with the two stage thin-disk amplifier system, no problems arising from the ASE could be observed in the amplifiers. The simulation code was able to predict the characteristics of both amplifiers with a small deviation for the second stage. This deviation can not be modeled in the one dimensional simulation code due to the lack of a spatial dimension in the disk gain medium. Therefore, a more sensitive numerical model needs to be developed which also includes the spatial properties of the amplified pulses in the thin-disk gain medium.

For improving the output characteristics of the amplifier in terms of pointing and temporal stability, a new setup has been engineered and needs to be implemented in the future. This contains frames for the mirror holders of the multipass which are made of granite to reduce the influence of vibrations on the mirror holders. This reduces the pointing fluctuations which are caused by the environment of the setup. A schematic of the setup can be found in figure 6.1. Further improvements of the pointing stability can be achieved by reducing the influence of the air flow introduced by the flowboxes above the optical table. This is achieved by a housing around the thin-disk amplifiers.

To stabilize the temporal properties of the amplifier, Zerodur bars are implemented in the setup. These have a negligible thermal expansion coefficient such that an elongation of the setup and thus a timing drift of the amplifier output can be avoided. The mirror holder frames are coupled to the disk by these Zerodur bars. With these measures performed in the setup, the entire amplifier system should deliver a spatially and temporally stable output which can then be used for the OPCPA pumping.

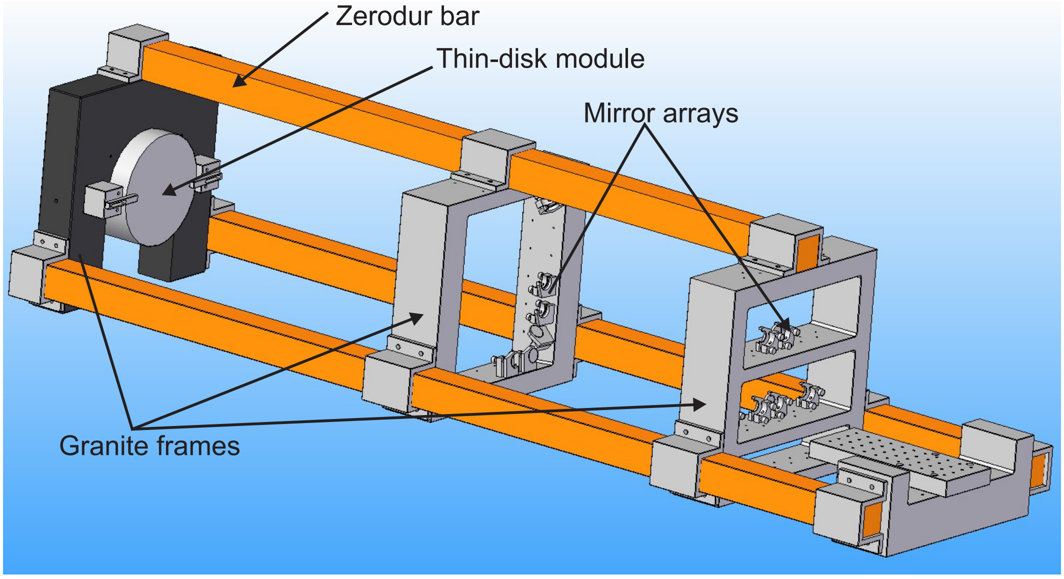

Figure 6.1: Planned setup of the stabilized thin-disk amplifier. The mirror arrays are mounted on granite frames for a better stability against vibrations of the experimental environment. Additionally, these frames are mounted to a fixed distance with respect to the disk module by Zerodur bars which have a negligible thermal expansion coefficient. This eliminates the sensitivity of the multipass length to changes in the environmental temperature.

In addition to the experiments with the thin-disk laser, a method of compensating for the temporal drift introduced by the pump amplifier was developed and tested. This includes a two-crystal optical balanced cross-correlator which is able to measure temporal drifts of the pump-to-seed synchronization in a direction sensitive way. The output signal of this cross-correlator can be used as a feedback signal for an optical delay line in the pump beam path. Thus, a long term stability of the OPCPA output can be achieved with an rms jitter below 50 fs. This device still needs to be tested for its capabilities as feedback system in the burst-mode operation of the entire laser system. Since this device is conceived only for long time drift compensation, there should be no problems by implementing it in the burst-mode laser.

Bibliography

[1] T.H. Maiman. *Stimulated optical radiation in ruby.* Nature 187, 493, (1960).

[2] P.A. Franken, A.E. Hill, C.W. Peters, and G. Weinreich. *Generation of Optical Harmonics.* Phys. Rev. Lett. 7, 118, (1961).

[3] G.H.C. New and J.F. Ward. *Optical third-harmonic generation in gases.* Phys. Rev. Lett. 19, 556, (1967).

[4] J. Reintjes and R.C. Eckardt. *Efficient harmonic generation from 532 to 266 nm in ADP and KD*P.* Appl. Phys. Lett. 30, 91, (1977).

[5] L.E. Hargrove, R.L. Fork, and M.A. Pollack. *Locking of He-Ne laser modes induced by synchronous intracavity modulation.* Appl. Phys. Lett. 5, 4, (1964).

[6] E.P. Ippen, C.V. Shank, and A. Dienes. *Passive mode locking of the cw dye laser.* Appl. Phys. Lett. 21, 348, (1972).

[7] H.A. Haus. *Mode locking of lasers.* IEEE J. Sel. Top. Quantum Electron. 6, 1173, (2000).

[8] P.B. Corkum. *Plasma perspective on strong-field multiphoton ionization.* Phys. Rev. Lett. 71, 1994, (1993).

[9] C. Spielmann, N.H. Burnett, S. Sartania, R. Koppitsch, M. Schnürer, C. Kan, M. Lenzner, P. Wobrauschek, and F. Krausz. *Generation of coherent X-rays in the water window using 5-femtosecond laser pulses.* Science 278, 661, (1997).

[10] P. Salieres. *Generation of ultrashort coherent XUV pulses by harmonic conversion of intense laser pulses in gases: towards attosecond pulses.* Meas. Sci. Technol. 12, 1818, (2001).

[11] M. Drescher, M. Hentschel, R. Kienberger, G. Tempea, C. Spielmann, G.A. Reider, P.B. Corkum, and F. Krausz. *X-ray pulses approaching the attosecond frontier.* Science 291, 1923, (2001).

[12] P.M. Paul, E.S. Toma, P. Breger, G. Mullot, F. Augé, P. Balcou, H.G. Muller, and P. Agostini. *Observation of a train of attosecond pulses from high harmonic generation.* Science 292, 1689, (2001).

[13] J. Chanteloup, D. Albach, A. Lucianetti, T. Novo, and B. Vincent. *6.6 J / 2 Hz Yb:YAG Diode-Pumped Laser Chain Activation.* Advanced Solid-State Photonics (ASSP), ATuE4, (2011).

[14] D.J. Richardson, J. Nilsson, and W.A. Clarkson. *High power fiber lasers: current status and future perspectives [Invited].* J. Opt. Soc. Am. B 27, B63, (2010).

[15] G. Mourou, B. Brocklesby, T. Tajima, and J. Limpert. *The future is fibre accelerators.* Nature Photonics 7, 258, (2013).

[16] P. Russbüldt, T. Mans, G. Rotarius, J. Weitenberg, H.D. Hoffmann, and R. Poprawe. *400W Yb:YAG Innoslab fs-amplifier.* Opt. Express 17, 12230, (2009).

[17] A. Giesen, H. Hügel, A. Voss, K. Wittig, U. Brauch, and H. Opower. *Scalable concept for diode-pumped high-power solid-state lasers.* Appl. Phys. B 58, 365, (1994).

[18] P. Emma, R. Akre, J. Arthur, R. Bionta, C. Bostedt, J. Bozek, A. Brachmann, P. Bucksbaum, R. Coffee, F.-J. Decker, Y. Ding, D. Dowell, S. Edstrom, A. Fisher, J. Frisch, S. Gilevich, J. Hastings, G. Hays, P. Hering, Z. Huang, R. Iverson, H. Loos, M. Messerschmidt, A. Miahnahri, S. Moeller, H.-D. Nuhn, G. Pile, D. Ratner, J. Rzepiela, D. Schultz, T. Smith, P. Stefan, H. Tompkins, J. Turner, J. Welch, W. White, J. Wu, G. Yocky, and J. Galayda. *First lasing and operation of an ångstrom-wavelength free-electron laser.* Nat. Photonics 4, 641, (2010).

[19] J.N. Galayda, J. Arthur, D.F. Ratner, and W.E. White. *X-ray free-electron lasers - present and future capabilities.* J. Opt. Soc. Am. B 27 (11), B106, (2010).

[20] G. Lambert, T. Hara, D. Garzella, T. Tanikawa, M. Labat, B. Carre, H. Kitamura, T. Shintake, M. Bougeard, S. Inoue, Y. Tanaka, P. Salieres, H. Merdji, O. Chubar, O. Gobert, K. Tahara, and M.-E. Couprie. *Injection of harmonics generated in gas in a free-electron laser providing intense and coherent extreme-ultraviolet light.* Nature Physics 4, 296, (2008).

[21] E. Allaria, C. Callegari, D. Cocco, W.M. Fawley, M. Kiskinova, C. Masciovecchio, and F. Parmigiani. *The FERMI@Elettra free-electron-laser source for coherent x-ray physics: photon properties, beam transport system and applications.* New Journal of Physics 12, 075002, (2010).

[22] D. Shu, Y. Shvydko, J. Amann, P. Emma, S. Stoupin, and J. Quintana. *Design of a diamond-crystal monochromator for the LCLS hard x-ray self-seeding project.* J. Phys.: Conf. Ser. 425 052004, (2013).

[23] J. Feldhaus. *FLASH - the first soft x-ray free electron laser (FEL) user facility.* J. Phys. B: At. Mol. Opt. Phys. 43 194002, (2010).

[24] B. Faatz, N. Baboi, V. Ayvazyan, V. Balandin, W. Decking, S. Duesterer, H.-J. Eckoldt, J. Feldhaus, N. Golubeva, K. Honkavaara, M. Koerfer, T. Laarmann, A. Leuschner, L. Lilje, T. Limberg, D. Noelle, F. Obier, A. Petrov, E. Ploenjes, K. Rehlich, H. Schlarb, B. Schmidt, M. Schmitz, S. Schreiber, H. Schulte-Schrepping, J. Spengler, M. Staack, F. Tavella, K. Tiedtke, M. Tischer, R. Treusch, M. Vogt, A. Willner, J. Bahrdt, R. Follath, M. Gensch, K. Holldack, A. Meseck, R. Mitzner, M. Drescher, V. Miltchev, J. Rönsch-Schulenburg, and J. Rossbach. *Flash II: Perspectives and challenges.* Nucl. Instrum. Meth. A 635, S2, (2011).

[25] I. Will, H.I. Templin, S. Schreiber, and W. Sandner. *Photoinjector drive laser of the FLASH FEL.* Opt. Express 19, 23770, (2011).

[26] H. Redlin, A. Al-Shemmary, A. Azima, N. Stojanovic, F. Tavella, I. Will, and S. Düsterer. *The FLASH pump-probe laser system: Setup, characterization and optical beamlines.* Nucl. Instrum. Meth. A 635, S88, (2011).

[27] C. Emmelmann and J.P. Calderón Urbina. *Analysis of the Influence of Burst-Mode Laser Ablation by Modern Quality Tools.* Science Direct, Physics Procedia 12, 172, (2011).

[28] F. Tavella, A. Willner, J. Rothhardt, S. Hädrich, E. Seise, S. Düsterer andT. Tschentscher, H. Schlarb, J. Feldhaus, J. Limpert, A. Tünnermann, and J. Rossbach. *Fiber-amplifier pumped high average power few-cycle pulse non-collinear OPCPA.* Opt. Express 18, 4689, (2010).

[29] J. Rothhardt, S. Hädrich, E. Seise, M. Krebs, F. Tavella, A. Willner, S. Düsterer, H. Schlarb, J. Feldhaus, J. Limpert, J. Rossbach, and A. Tünnermann. *High average and peak power few-cycle laser pulses delivered by fiber pumped OPCPA system.* Opt. Express 18, 12719, (2010).

[30] R. Paschotta. *Encyclopedia of Laser Physics and Technology.* Wiley-VCH Verlag, (2008).

[31] R. Menzel. *Photonics.* Second Edition, Springer Verlag, (2007).

[32] P.A. Bélanger. *Beam propagation and the ABCD ray matrices.* Opt. Lett. 16, 196, (1991).

[33] C. Rullière. *Femtosecond Laser Pulses.* Second Edition, Springer Verlag, (2005).

[34] Z.Y. Ou, S.F. Pereira, E.S. Polzik, and H.J. Kimble. *85 percent efficiency for cw frequency doubling from 1.08 to 0.54 μm.* Opt. Lett. 17, 640, (1992).

[35] R. Paschotta, P. Kürz, R. Henking, S. Schiller, and J. Mlynek. *82 percent efficient continuous-wave frequency doubling of 1.06 μm with a monolithic MgO:LiNbO3 resonator.* Opt. Lett. 19, 1325, (1994).

[36] F. Shimizu. *Frequency broadening in liquids by a short light pulse.* Phys. Rev. Lett. 19, 1097, (1976).

[37] D.S. Steingrube, M. Kretschmar, D. Hoff, E. Schulz, T. Binhammer, P. Hansinger, G.G. Paulus, U. Morgner, and M. Kovacev. *Sub-1.5-cycle pulses from a single filament.* Opt. Express 20, 24049, (2012).

[38] M.D. Perry, T. Ditmire, and B.C. Stuart. *Self-phase modulation in chirped-pulse amplification.* Opt. Lett. 19, 2149, (1994).

[39] D. Strickland and G. Mourou. *Compression of Amplified Chirped Optical Pulses.* Opt. Commun. 56, 219, (1985).

[40] M.D. Perry, D. Pennington, B. C. Stuart, G. Tietbohl, J.A. Britten, C. Brown, S. Herman, B. Golick, M. Kartz, J. Miller, H.T. Powell, M. Vergino, and V. Yanovsky. *Petawatt laser pulses.* Opt. Lett. 24, 160, (1999).

[41] R.A. Baumgartner and R.L. Byer. *Optical Parametric Amplification.* IEEE J. Quantum Electron. QE 15, 432, (1979).

[42] G. Cerullo and S. De Silvestri. *Ultrafast optical parametric amplifiers.* Rev. Sci. Instrum. 74, 1, (2003).

[43] A. Galvanauskas, A. Hariharan, D. Harter, M.A. Arbore, and M.M. Fejer. *High-energy femtosecond pulse amlification in a quasi-phase-matched parametric amplifier.* Opt. Lett. 23, 210, (1998).

[44] D.N. Schimpf, J. Rothhardt, J. Limpert, A. Tünnermann, and D.C. Hanna. *Theoretical analysis of the gain bandwidth for noncollinear parametric amplification of ultrafast pulses.* J. Opt. Soc. Am. B 24 (11), 2837, (2007).

[45] F. Tavella. *Multiterawatt few-cycle pulse OPCPA for applications in high-field physics.* Dissertation an der Fakultät für Physik der Ludwig Maximilians Universität München, (2007).

[46] G. Cerullo, M. Nisoli, S. Stagira, and S. De Silvestri. *Sub-8-fs pulses from an ultrabroadband optical parametric amplifier in the visible.* Opt. Lett. 23, 1283, (1998).

[47] A. Shirakawa, I. Sakane, M. Takasaka, and T. Kobayashi. *Sub-5-fs visible pulse generation by pulse-front-matched noncollinear optical parametric amplification.* Appl. Phys. Lett. 74 (16), 2268, (1999).

[48] R. Butkus, R. Danielius, A. Dubietis, A. Piskarskas, and A. Stabinis. *Progress in chirped pulse optical parametric amplifiers.* Appl. Phys. B 79, 693, (2004).

[49] I.N. Ross, P. Matousek, M. Towrie, A.J. Langley, and J.L. Collier. *The prospects for ultrashort pulse duration and ultrahigh intensity using optical parametric chirped pulse amplifiers.* Opt. Commun. 144, 125, (1997).

[50] F. Tavella, Y. Nomura, L. Veisz, V. Pervak, A. Marcinkevicius, and F. Krausz. *Dispersion management for a sub-10-fs, 10 TW optical parametric chirped-pulse amplifier.* Opt. Lett. 32, 2227, (2007).

[51] F. Tavella, A. Marcinkevicius, and F. Krausz. *90 mJ parametric chirped pulse amplification of 10 fs pulses.* Opt. Express 14, 12822, (2006).

[52] S. Adachi, N. Ishii, T. Kanai, A. Kosuge, J. Itatani, Y. Kobayashi, D. Yoshitomi, K. Torizuka, and S. Watanabe. *5-fs, multi-mJ, CEP-locked parametric chirped-pulse amplifier pumped by a 450-nm source at 1 kHz.* Opt. Express 16, 14341, (2008).

[53] D. Herrmann, L. Veisz, R. Tautz, F. Tavella, K. Schmid, V. Pervak, and F. Krausz. *Generation of sub-three-cycle, 16 TW light pulses by using noncollinear optical parametric chirped-pulse amplification.* Opt. Lett. 34, 2459, (2009).

[54] I.N. Ross, J.L. Collier, P. Matousek, C.N. Danson, D. Neely, R.M. Allott, D.A. Pepler, C. Hernandez-Gomez, and K. Osvay. *Generation of terawatt pulses by use of optical parametric chirped pulse amplification.* Appl. Opt. 39 (15), 2422, (2000).

[55] X. Yang, Z. Xu, Y. Leng, H. Lu, L. Lin, Z. Zhang, R. Li, W. Zhang, D. Yin, and Bing Tang. *Multiterawatt laser system based on optical parametric chirped pulse amplification.* Opt. Lett. 27, 1135, (2002).

[56] Y. Kitagawa, H. Fujita, R. Kodama, H. Yoshida, S. Matsuo, T. Jitsuno, T. Kawasaki, H. Kitamura, T. Kanabe, S. Sakabe, K. Shigemori, N. Miyanaga, and Y. Izawa. *Prepulse-free petawatt laser for a fast ignitor.* IEEE J. Quantum Electron. 40 (3), 281, (2004).

[57] L.J. Waxer, D.N. Maywar, J.H. Kelly, T.J. Kessler, B.E. Kruschwitz, S.J. Loucks, R.L. McCrory, D.D. Meyerhofer, S.F.B. Morse, C. Stoeckl, and J.D. Zuegel. *High-energy petawatt capability for the Omega laser.* Opt. Photon. News 16 (7), 30, (2005).

[58] V.V. Lozhkarev, G.I. Freidman, V.N. Ginzburg, E.V. Katin, E.A. Khazanov, A.V. Kirsanov, G.A. Luchinin, A.N. Mal'shakov, M.A. Martyanov, O.V. Palashov, A.K. Poteomkin, A.M. Sergeev, A.A. Shaykin, I.V. Yakovlev, S.G. Garanin, S.A. Sukharev, N.N. Rukavishnikov, A.V. Charukhchev, R.R. Gerke, and V.E. Yashin. *200 TW 45 fs laser based on optical parametric chirped pulse amplification.* Opt. Express 14, 446, (2006).

[59] C.J. Koester and E. Snitzer. *Amplification in a Fiber Laser.* Appl. Opt. 3, 1182, (1964).

[60] E. Snitzer, H. Po, F. Hakami, R. Tumminelli, and B.C. McCollum. *Double-clad, offset core Nd fiber laser.* Opt. Fiber Sens., Opt. Soc. Amer. Tech. Dig. Ser., vol. 2, Postdeadline Paper PD5, (1988).

[61] H. Zellmer, A. Tünnermann, H. Welling, and V. Reichel. *Double-clad fiber with 30 W output power.* OSA TOPS: Proc. OAA 16, FAW18, (1997).

[62] V. Dominic, S. MacCormack, R. Waarts, S. Sanders, S. Bicknese, R. Dohle, E. Wolak, P.S. Yeh, and E. Zucker. *110 W fibre laser.* Electron. Lett. 35, CPD11/1, (1999).

[63] J. Limpert, A. Liem, H. Zellmer, and A. Tünnermann. *500 W continuous-wave fiber laser with excellent beam quality.* Electron. Lett. 39, 645, (2003).

[64] Y. Jeong, J.K. Sahu, D.N. Payne, and J. Nilsson. *Ytterbium-doped large-core fiber laser with 1.36 kW continuous-wave output power.* Opt. Express 12, 6088, (2004).

[65] A. Tünnermann, T. Schreiber, F. Röser, A. Liem, S. Höfer, H. Zellmer, S. Nolte, and J. Limpert. *The renaissance and bright future of fibre lasers.* J. Phys. B, At. Mol. Opt. Phys, vol. 38, S681, (2005).

[66] J. Limpert, F. Röser, T. Schreiber, and A. Tünnermann. *High-Power Ultrafast Fiber Laser Systems.* IEEE J. Quantum Electron. 12, 233, (2006).

[67] D. Gloge. *Weakly guiding fibers.* Appl. Opt. 10, 2252, (1971).

[68] M. Fermann. *Single-mode excitation of multimode fibers with ultrashort pulses.* Opt. Lett. 23, 52, (1998).

[69] J.M. Sousa and O.G. Okhotnikov. *Multimode Er-doped fiber for singletransverse-mode amplification.* Appl. Phys. Lett. 74, 1528, (1999).

[70] J.A. Alvarez-Chavez, H.L. Offerhaus, J. Nilsson, P.W. Turner, W.A. Clarkson, and D.J. Richardson. *High-energy, high-power ytterbium-doped Q-switched fiber laser.* Opt. Lett. 25, 37, (2000).

[71] J.A. Alvarez-Chavez, A.B. Grudinin, J. Nilsson, P.W. Turner, and W.A. Clarkson. *Mode selection in high power cladding pumped fibre lasers with tapered section.* CLEO Conference, OSA Techn. Dig., 247, (1999).

[72] A. Galvanauskas. *Mode-scalable fiber-based chirped pulse amplification systems.* IEEE J. Quantum Electron. 7, 504, (2001).

[73] J.I. Sakai and T. Kimura. *Bending loss of propagationmodes in arbitrary-index profile optical fibers.* Appl. Opt. 17, 1499, (1978).

[74] P. Koplow, D. Kliner, and L. Goldberg. *Single-mode operation of a coiled multimode fiber amplifier.* Opt. Lett. 25, 442, (2000).

[75] J.P. Russell. *Photonic crystral fibers.* Science 299, 358, (2003).

[76] J. Knight, T. Birks, P. Russell, and D. Atkin. *All-silica single-mode optical fiber with photonic crystal cladding.* Opt. Lett. 21, 1547, (1996).

[77] T. Birks, J. Knight, and P. Russell. *Endlessly single-mode photonic crystal fiber.* Opt. Lett. 22, 961, (1997).

[78] N.A. Mortensen, M.D. Nielsen, J.R. Folkenberg, A. Petersson, and H.R. Simonsen. *Improved large-mode-area endlessly singlemode photonic crystal fibers.* Opt. Lett. 28, 393, (2003).

[79] J. Limpert, A. Liem, T. Schreiber, S. Nolte, H. Zellmer, A. Tünnermann, J. Broeng, A. Petersson, C. Jacobsen, H. Simonsen, and N.A. Mortensen. *Extended large-mode-area single mode microstructured fiber laser.* CLEO Conference, Paper CMS6, (2004).

[80] W.J. Wadsworth, R.M. Percival, G. Bouwmans, J.C. Knight, and P.S.J. Russell. *High power air-clad photonic crystal fibre laser.* Opt. Express 11, 48, (2003).

[81] J. Limpert, T. Schreiber, S. Nolte, H. Zellmer, T. Tünnermann, R. Iliew, F. Lederer, J. Broeng, G. Vienne, A. Petersson, and C. Jakobsen. *High-power air-clad large-mode-area photonic crystal fiber laser.* Opt. Express 11, 818, (2003).

[82] J. Limpert, A. Liem, M. Reich, T. Schreiber, S. Nolte, H. Zellmer, A. Tünnermann, J. Broeng, A. Petersson, and C. Jakobsen. *Low-nonlinearity single-transverse-mode ytterbium-doped photonic crystal fiber amplifier.* Opt. Express 12, 1313, (2004).

[83] T. Eidam, S. Hanf, E. Seise, T.V. Andersen, T. Gabler, C. Wirth, T. Schreiber, J. Limpert, and A. Tünnermann. *Femtosecond fiber CPA system emitting 830 W average output power.* Opt. Lett. 35, 94, (2010).

[84] F. Stutzki, F. Jansen, T. Eidam, A. Steinmetz, C. Jauregui, J. Limpert, and A. Tünnermann. *High average power large-pitch fiber amplifier with robust single-mode operation.* Opt. Lett. 36, 689, (2011).

[85] F. Stutzki, F. Jansen, A. Liem, C. Jauregui, J. Limpert, and A. Tünnermann. *26 mJ, 130 W Q-switched fiber-laser system with near-diffraction-limited beam quality.* Opt. Lett. 37, 1073, (2012).

[86] J. Limpert, N. Deguil-Robin, I. Manek-Hönninger, F. Salin, F. Röser, A. Liem, T. Schreiber, S. Nolte, H. Zellmer, A. Tünnermann, J. Broeng, A. Petersson, and C. Jakobsen. *High-power rod-type photonic crystal fiber laser.* Opt. Express 13, 1055, (2005).

[87] J. Limpert, T. Schreiber, A. Liem, S. Nolte, H. Zellmer, T. Peschel, V. Guyenot, and A. Tünnermann. *Thermo-optical properties of air-clad photonic crystal fiber lasers in high power operation.* Opt. Express 11, 2982, (2003).

[88] L. Daniault, M. Hanna, L. Lombard, Y. Zaouter, E. Mottay, D. Goular, P. Bourdon, F. Druon, and P. Georges. *Coherent beam combining of two femtosecond fiber chirped-pulse amplifiers.* Opt. Lett. 36, 621, (2011).

[89] Y. Zaouter, L. Daniault, M. Hanna, D.N. Papadopoulos, F. Morin, C. Hönninger, F. Druon, E. Mottay, and P. Georges. *Passive coherent combination of two ultrafast rod type fiber chirped pulse amplifiers.* Opt. Lett. 37, 1460, (2012).

[90] C.X. Yu, S.J. Augst, S.M. Redmond, K.C. Goldizen, D.V. Murphy, A. Sanchez, and T.Y. Fan. *Coherent combining of a 4 kW, eight-element fiber amplifier array.* Opt. Lett. 36, 2686, (2011).

[91] R. Su, P. Zhou, X. Wang, H. Zhang, and X. Xu. *Active coherent beam combining of a five-element, 800 W nanosecond fiber amplifier array.* Opt. Lett. 37, 3978, (2012).

[92] S.M. Redmond, D.J. Ripin, C.X. Yu, S.J. Augst, T. Yee Fan, P.A. Thielen, J.E. Rothenberg, and G.D. Goodno. *Diffractive coherent combining of a 2.5 kW fiber laser array into a 1.9 kW Gaussian beam.* Opt. Lett. 37, 2832, (2012).

[93] R.J. Shine, A.J. Alfrey, and R.L. Byer. *40-W cw, TEM*$_{00}$*-mode, diode-laser-pumped, Nd:YAG mimiature-slab laser.* Opt. Lett. 20, 459, (1995).

[94] T.S. Rutherford, W.M. Tulloch, S. Sinha, and R.L. Byer. *Yb:YAG and Nd:YAG edge-pumped slab lasers.* Opt. Lett. 26, 986, (2001).

[95] B.J. Comaskey, G.F. Albrecht, R.J. Beach, S.P. Velsko, S.B. Sutton, S.C. Mitchell, C.S. Petty, K.S. Jancaitis, W.J. Benett, B.L. Freitas, and R.W. Solarz. *One-kilowatt average-power diode-pumped Nd:YAG folded zigzag slab laser.* Proc. SPIE 1865, 9, (1993).

[96] P. Russbüldt, T. Mans, G. Rotarius, D. Hoffmann, R. Poprawe, T. Eidam, J. Limpert, and A. Tünnermann. *Hybrid 400W Fiber-Innoslab fs-Amplifier.* Advanced Solid-State Photonics (ASSP), MF4, (2009).

[97] P. Russbüldt, T. Mans, J. Weitenberg, H.D. Hoffmann, and R. Poprawe. *Compact diode-pumped 1.1 kW Yb:YAG Innoslab femtosecond amplifier.* Opt. Lett. 35, 4169, (2010).

[98] K. Contag, M. Karszewski, C. Stewen, A. Giesen, and H. Hügel. *Theoretical modelling and experimental investigations of the diode-pumped thin disk Yb:YAG laser.* IEEE J. Quantum Electron. 29 (8), 697, (1999).

[99] C. Stewen, K. Contag, M. Larionov, A. Giesen, and H. Hügel. *A 1-kW cw thin disc laser.* IEEE J. Sel. Top. Quantum Electron. 6 (4), 650, (2000).

[100] J. Mende, E. Schmid, J. Speiser, G. Spindler, and A. Giesen. *Thin-disk laser - Power scaling to the kW regime in fundamental mode operation.* Proc. of SPIE 7193, 71931V-1, (2009).

[101] C.R.E. Baer, C. Kränkel, C.J. Saraceno, O.H. Heckl, M. Golling, R. Peters, K. Petermann, T. Südmeyer, G. Huber, and U. Keller. *Femtosecond thin-disk laser with 141 W of average power.* Opt. Lett. 35, 2302, (2010).

[102] D. Bauer, I. Zawischa, D.H. Sutter, A. Killi, and T. Dekorsy. *Mode-locked Yb:YAG thin-disk oscillator with 41* μ*J pulse energy at 145 W average infrared power and high power frequency conversion.* Opt. Express 20, 9698, (2012).

[103] C.J. Saraceno, F. Emaury, O.H. Heckl, C.R.E. Baer, M. Hoffmann, C. Schriber, M. Golling, T. Südmeyer, and U. Keller. *275 W average output power from a femtosecond thin disk oscillator operated in a vacuum environment.* Opt. Express 20, 23535, (2012).

[104] S.V. Marchese, C.R. Baer, A.G. Engqvist, S. Hashimoto, D.J. Maas, M. Golling, T. Südmeyer, and U. Keller. *Femtosecond thin disk laser oscillator with pulse energy beyond the 10-microjoule level.* Opt. Express 16, 6397, (2008).

[105] J. Neuhaus, J. Kleinbauer, A. Killi, S. Weiler, D. Sutter, and T. Dekorsy. *Passively mode-locked Yb:YAG thin-disk laser with pulse energies exceeding 13 μJ by use of an active multipass geometry.* Opt. Lett. 33, 726, (2008).

[106] J. Neuhaus, D. Bauer, J. Zhang, A. Killi, J. Kleinbauer, M. Kumkar, S. Weiler, M. Guina, D.H. Sutter, and T. Dekorsy. *Subpicosecond thin-disk laser oscillator with pulse energies of up to 25.9 microjoules by use of an active multipass geometry.* Opt. Express 16, 20530, (2008).

[107] O. Pronin, J. Brons, C. Grasse, V. Pervak, G. Boehm, M.-C. Amann, V.L. Kalashnikov, A. Apolonski, and F. Krausz. *High-power 200 fs Kerr-lens mode-locked Yb:YAG thin-disk oscillator.* Opt. Lett. 36, 4746, (2011).

[108] O. Pronin, J. Brons, C. Grasse, V. Pervak, G. Boehm, M.-C. Amann, A. Apolonski, V. L. Kalashnikov, and F. Krausz. *High-power Kerr-lens mode-locked Yb:YAG thin-disk oscillator in the positive dispersion regime.* Opt. Lett. 37, 3543, (2012).

[109] C. Hönninger, I. Johannsen, M. Moser, G. Zhang, A. Giesen, and U. Keller. *Diode-pumped thin-disk Yb:YAG regenerative amplifier.* Appl. Phys. B 65, 423, (1997).

[110] A. Beyertt, D. Nickel, and A. Giesen. *Femtosecond thin-disk Yb:KYW regenerative amplifier.* Appl. Phys. B 80, 655, (2005).

[111] M. Larionov, F. Butze, D. Nickel, and A. Giesen. *High-repetition-rate regenerative thin-disk amplifier with 116 μJ pulse energy and 250 fs pulse duration.* Opt. Lett. 32, 494, (2007).

[112] U. Buenting, H. Sayinc, D. Wandt, U. Morgner, and D. Kracht. *Regenerative thin disk amplifier with combined gain spectra producing 500 μJ sub 200 fs pulses.* Opt. Express 17, 8046, (2009).

[113] T. Metzger, A. Schwarz, C.Y. Teisset, D. Sutter, A. Killi, R. Kienberger, and F. Krausz. *High-repetition-rate picosecond pump laser based on a Yb:YAG disk amplifier for optical parametric amplification.* Opt. Lett. 34, 2123, (2009).

[114] J. Tümmler, R. Jung, H. Stiel, P.V. Nickles, and W. Sandner. *High-repetition-rate chirped-pulse-amplification thin-disk laser system with joule-level pulse energy.* Opt. Lett. 34, 1378, (2009).

[115] M. Suzuki, H. Kiriyama, I. Daito, Y. Ochi, H. Okada, M. Sato, Y. Tamaoki, T. Yoshii, J. Maeda, S. Matsuoka, H. Kan, P.R. Bolton, A. Sugiyama, K. Kondo, and S. Kawanishi. *Hundred mJ, sub-picoseconds, high temporal contrast OPCPA/Yb:YAG ceramic thin disk hybrid laser system.* Appl. Phys. B 105, 181, (2012).

[116] M. Siebold, M. Loeser, F. Roeser, M. Seltmann, G. Harzendorf, I. Tsybin, S. Linke, S. Banerjee, P.D. Mason, P.J. Phillips, K. Ertel, J.C. Collier, and U. Schramm. *High-energy, ceramic-disk Yb:LuAG laser amplifier.* Opt. Express 20, 21992, (2012).

[117] J.A. Glaze, S. Guch, and J.B. Trenholme. *Parasitic Suppression in Large Aperture Nd:Glass Disk Laser Amplifiers.* Appl. Opt. 13, 2808, (1974).

[118] D.C. Brown, S.D. Jacobs, and N. Nee. *Parasitic oscillations, absorption, stored energy density and heat density in active-mirror and disk amplifiers.* Appl. Opt. 17, 211, (1978).

[119] D. Albach, J.-C. Chanteloup, and G. le Touzé. *Influence of ASE on the gain distribution in large size, high gain Yb:YAG slabs.* Opt. Express 17, 3792, (2009).

[120] D. Kouznetsov, J. Bisson, and K. Ueda. *Scaling laws of disk lasers.* Opt. Materials 31, 754, (2009).

[121] J. Speiser. *Scaling of thin-disk lasers - influence of amplified spontaneous emission.* J. Opt. Soc. Am. B 26, 26, (2009).

[122] J. Speiser and A. Giesen. *Scaling of Thin Disk Pulse Amplifiers.* Proc. of SPIE 6871, (2011).

[123] A. Antognini, K. Schuhmann, F.D. Amaro, F. Biraben, A. Dax, A. Giesen, T. Graf, T.W. Hänsch, P. Indelicato, L. Julien, C. Kao, P.E. Knowles, F. Kottmann, E. Le Bigot, Y. Liu, L. Ludhova, N. Moschüring, F. Mulhauser, T. Nebel, F. Nez, P. Rabinowitz, C. Schwob, D. Taqqu, and R. Pohl. *Thin-Disk Yb:YAG Oscillator-Amplifier Laser, ASE, and Effective Yb:YAG Lifetime.* IEEE J. Quantum Electron. 45, 993, (2009).

[124] K. Contag. *Modellierung und numerische Auslegung des Yb:YAG-Scheibenlasers.* Dissertation an der Universität Stuttgart, (2002).

[125] D. Kouznetsov and J. Bisson. *Role of undoped cap in the scaling of thin-disk lasers.* J. Opt. Soc. Am. B 25, 338, (2008).

[126] J.C. Diels and W. Rudolph. *Ultrashort Laser Pulse Phenomena.* Second Edition, Academic Press, (2006).

[127] S. Reuter. *Numerische Modellierung und experimentelle Charakterisierung der physikalischen Eigenschaften von modengekoppelten Femtosekunden-Yb:YAG und Yb:KGW Lasern.* Dissertation, Technische Universität Kaiserslautern, (2004).

[128] W.F. Krupke. *Ytterbium Solid-State Lasers - The First Decade.* IEEE J. Quantum Electron. 6, 1287, (2000).

[129] M.P. Hehlen. *Reabsorption artifacts in measured excited-state lifetimes of solids.* J. Opt. Soc. Am. B 14, 1312, (1997).

[130] D.S. Sumida and T.Y. Fan. *Effect of radiation trapping on fluorescence lifetime and emission cross section measurements in solid-state laser media.* Opt. Lett. 19, 1343, (1994).

[131] F.D. Patel, E.C. Honea, J. Speth, S.A. Payne, R. Hutcheson, and R. Equall. *Laser demonstration of Yb3Al5O12 (YbAG) and materials properties of highly doped Yb:YAG.* IEEE J. Quantum Electron. 37, 135, (2001).

[132] D.S. Sumida and T.Y. Fan. *Emission Spectra and Fluorescence Lifetime Measurements of Yb:YAG as a Function of Temperature.* OSA Proc. in Advanced Solid State Lasers, vol. 20, YL4, (1994).

[133] T.R. Schible, J. Kim, O. Kuzucu, J.T. Gopinath, S.N. Tandon, G.S. Petrich, L.A. Kolodziejski, J.G. Fujimoto, E.P. Ippen, and F.X. Kärtner. *Attosecond active synchronization of passively mode-locked lasers by balanced cross correlation.* Opt. Lett. 28, 947, (2003).

[134] J. Kim, J. Chen, Z. Zhang, F.N.C. Wong, and F.X. Kärtner. *Long-term femtosecond timing link stabilization using a single-crystal balanced cross correlator.* Opt. Lett. 32, 1044, (2007).

Acknowledgements

At first I want to thank Prof. Dr. Markus Drescher and Dr. Franz Tavella for giving me the opportunity to work on this outstandingly interesting topic during my time as PhD student.

Very special thanks goes to my mentor Dr. Franz Tavella. His experience with the work in the lab was tremendous and I could learn a lot from him. He was always a motivating help in conceiving the results and pushing the laser system further and further beyond the limits. His thinking outside of standard paths lead to the realization of the high power amplifiers presented in this thesis. His dedicated help in finding myself in the infrastructure and also for the preparation of publications and conference proceedings was invaluable.

I also want to thank the working group of Dr. Franz Tavella, where always a very good working atmosphere was present. Specially, I want to thank Robert Riedel and Dr. Mark Prandolini who helped a lot in the setup and operation of the different stages of the thin-disk amplifier.

I am grateful to the engineers at DESY who made a lot of experimental setups possible. The workshops always helped with small construction works on a short timescale. A special thanks to Marc Temme who was very interested in the proceedings of the project at all times. His dedicated help for the stabilized thin-disk setup was invaluable.

Zu guter letzt möchte ich mich bei meiner Familie bedanken, die mich auf dem langen Weg meiner Ausbildung immer unterstützt und begleitet hat. Auch an meine Freundin geht ein besonderer Dank.